

American University in Cairo

## AUC Knowledge Fountain

---

Theses and Dissertations

---

2-1-2013

### High performance 3-folded symmetric decoupled MEMS gyroscopes

Hani Hisham Tawfik

Follow this and additional works at: <https://fount.aucegypt.edu/etds>

---

#### Recommended Citation

##### APA Citation

Tawfik, H. (2013). *High performance 3-folded symmetric decoupled MEMS gyroscopes* [Master's thesis, the American University in Cairo]. AUC Knowledge Fountain.

<https://fount.aucegypt.edu/etds/1281>

##### MLA Citation

Tawfik, Hani Hisham. *High performance 3-folded symmetric decoupled MEMS gyroscopes*. 2013. American University in Cairo, Master's thesis. *AUC Knowledge Fountain*.

<https://fount.aucegypt.edu/etds/1281>

This Thesis is brought to you for free and open access by AUC Knowledge Fountain. It has been accepted for inclusion in Theses and Dissertations by an authorized administrator of AUC Knowledge Fountain. For more information, please contact [mark.muehlhaeusler@aucegypt.edu](mailto:mark.muehlhaeusler@aucegypt.edu).



**The American University in Cairo**  
**School of Sciences and Engineering**

# **High Performance 3-Folded Symmetric Decoupled MEMS Gyroscopes**

By

**Hani Hisham Tawfik**

A thesis submitted in partial fulfillment of the requirements for the degree of  
**Master of Science in Nanotechnology**

under the supervision of:

**Dr. Sherif Sedky**

**Professor of Physics, American University in Cairo**  
**Founding Provost, Zewail University**

**Summer 2012**

**To my parents,  
brothers and sister.**

## **Acknowledgements**

There are number of people I would like to acknowledge their support, on professional and social aspects, that without it this work would never be achieved. I would like first to thank my supervisor Prof. Sherif Sedky for the endless knowledge and research skills that he taught me. In addition, I want to state my utmost appreciation for the unmatched support and advisement that he shown during the entire 3-years of the project. Not to mention his tireless efforts to sustain the project funds. This provided state of art facilities in microfarbication which gave the chance for me, and my colleagues, to obtain high tech hands-on experience. Also, I would like to thank Dr. Amro El Shurafa for his precious advises regarding all the aspect related to research from suggesting a research point to writing a technical paper, in addition, to his supervision on modeling the gyroscopes performance. I can't forget Dr. Ahmed Emira's role for supporting me with several ideas that improved the quality of the latter work. I would like to thank my classmate and my friend, Karim Khairallah for helping me verifying the numerical model.

I want to send my special thanks and appreciation to Dr. Mohamed Serry for his guidance during the fabrication phase. His patience and understanding made me master the usage of various microfabrication facilities at the American University in Cairo (AUC) clean room. I learned a lot from him as a researcher and as a person. I am very grateful to my best friend Ahmed Kamal, for his during my beginning months at Yousef Jameel Science and Technology Research Center (YJ-STRC). His illustrations regarding the novel gyroscope design was extremely fruitful. Moreover, I would like to thank Dr. Abdelhameed Sharaf for his help in building the characterization setup for the fabricated devices. I want to send my warm regards to my friend Joseph Ernest for his help in setting up the electroplating facility. Special thanks to Mohamed Ibrahim for his endless efforts to sustain the fabrication quality and facilities at the AUC clean room up to the world standards. I want to send my sincerest thanks to King Abdallah Univeristy for Science and Technology for funding the research project and my masters' studies.

At last, but not least, I want to send my warm appreciation to my family (parents, brothers, sister, and fiancée) for their endless efforts to provide stable environment at home and for keeping pushing me forward. Everything I am, and will be, is because of them.



## Abstract

This thesis reports, for the first time, on a novel design and architecture for realizing inertial grade gyroscope based on Micro-Electro-Mechanical Systems (MEMS) technology. The proposed device is suitable for high-precision Inertial Navigation Systems (INS). The new design has been investigated analytically and numerically by means of Finite Element Modeling (FEM) of the shapes, resonance frequencies and decoupling of the natural drive and sense modes of the various implementations. Also, famous phenomena known as spring softening and spring hardening are studied. Their effect on the gyroscope operation is modeled numerically in Matlab/Simulink platform. This latter model is used to predict the drive/sense mode matching capability of the proposed designs.

Based on the comparison with the best recently reported performance towards inertial grade operation, it is expected that the novel architecture further lowers the dominant Brownian (thermo-mechanical) noise level by more than an order of magnitude (down to  $0.08^{\circ}/\text{hr}$ ). Moreover, the gyroscope's figure of merit, such as output sensitivity ( $150 \text{ mV}/^{\circ}/\text{s}$ ), is expected to be improved by more than two orders of magnitude. This necessarily results in a signal to noise ratio (SNR) which is up to three orders of magnitude higher (up to  $1,900 \text{ mV}/^{\circ}/\text{hr}$ ). Furthermore, the novel concept introduced in this work for building MEMS gyroscopes allows reducing the sense parasitic capacitance by up to an order of magnitude. This in turn reduces the drive mode coupling or quadrature errors in the sensor's output signal. The new approach employs Silicon-on-Insulator (SOI) substrates that allows the realization of large mass ( $>1.6 \text{ mg}$ ), large sense capacitance ( $>2.2 \text{ pF}$ ), high quality factors ( $>21,000$ ), large drive amplitude ( $\sim 2\text{-}4 \text{ }\mu\text{m}$ ) and low resonance frequency ( $\sim 3\text{-}4 \text{ KHz}$ ) as well as the consequently suppressed noise floor and reduced support losses for high-performance vacuum operation.

Several challenges were encountered during fabrication that required developing high aspect ratio (up to 1:20) etching process for deep trenches (up to  $500 \text{ }\mu\text{m}$ ). Frequency Response measurement platform was built for devices characterization. The measurements were performed at atmospheric pressures causing huge drop of the devices performance. Therefore, various MEMS gyroscope packaging technologies are studied. Wafer Level Packaging (WLP) is selected to encapsulate the fabricated devices under vacuum by utilizing wafer bonding. Through Silicon Via (TSV) technology was developed (as connections) to transfer the electrical signals (of the fabricated devices) outside the cap wafers.

## Table of Contents

|  |      |
|--|------|
| Acknowledgements .....   | iii  |
| Abstract.....  | iv   |
| List of Figures .....  | viii |
| List of Tables .....   | xv   |
| List of Abbreviations.....   | xvi  |
| 1. Chapter I: Introduction .....   | 18   |
| 1.1. Mechanical Gyroscopes and Coriolis' Effect.....                       | 19   |
| 1.1.1. Performance Measures .....  | 22   |
| 1.1.2. Applications.....   | 23   |
| 1.1.3. Literature Survey .....   | 23   |
| 1.2. The Need for Novel Architecture .....                                 | 34   |
| 2. Chapter II: Novel MEMS Gyroscope Architectures .....                    | 36   |
| 2.1. Devices Operations.....   | 37   |
| 2.1.1. Vertical Suspension Gyroscope Architecture.....                     | 37   |
| 2.1.2. Hybrid Suspension Gyroscope Architecture .....                      | 39   |
| 2.2. Decoupling Analysis.....  | 41   |
| 2.2.1. Electrical Domain .....   | 41   |
| 2.2.2. Mechanical Domain .....   | 43   |
| 2.3. Mode Matching .....   | 49   |
| 2.3.1. Problem Setup for Electrostatic Domain.....                         | 50   |
| 2.3.2. Numerical Analysis.....   | 54   |
| 2.3.3. Model Verification (Case Study).....                                | 57   |
| 2.3.4. Results .....   | 60   |
| 2.4. Gyroscope Performance Measures .....                                  | 65   |
| 2.5. Performance Comparison with the State of The Art and Discussion ..... | 66   |
| 3. Chapter III: Devices Fabrication & Characterization.....                | 70   |

|  |     |
|--|-----|
| 3.1. Vertical Suspension Device Fabrication .....                  | 70  |
| 3.1.1. Fabrication Process Flow .....                              | 72  |
| 3.1.2. Layout.....   | 74  |
| 3.2. Hybrid Suspension Device Fabrication .....                    | 76  |
| 3.2.1. Fabrication Process Flow .....                              | 78  |
| 3.2.2. Layout.....   | 80  |
| 3.3. Developing the Etching Process .....                          | 81  |
| 3.3.1. Cryogenic DRIE Process.....                                 | 81  |
| 3.3.2. Profile Optimization.....                                   | 82  |
| 3.3.3. Surface Finish .....  | 82  |
| 3.3.4. Undercutting .....  | 83  |
| 3.3.5. Masking Material.....                                       | 83  |
| 3.3.6. Depth Dependent Profile .....                               | 84  |
| 3.3.7. Profile Optimization Results .....                          | 85  |
| 3.3.8. Notching effects at the Si-SiO <sub>2</sub> interface ..... | 87  |
| 3.3.9. Switching to Bosch process.....                             | 88  |
| 3.4. Micromachining Facilities .....                               | 88  |
| 3.4.1. Deep Reactive Ion Etching (DRIE) .....                      | 89  |
| 3.4.2. Photolithography.....                                       | 91  |
| 3.4.3. Chemical Vapor Deposition (CVD).....                        | 93  |
| 3.5. Characterization.....   | 94  |
| 3.5.1. Fabricated Devices.....                                     | 95  |
| 3.5.2. Measurement Setup.....                                      | 98  |
| 3.5.3. Frequency Sweep Results.....                                | 99  |
| 4. Chapter IV: Devices Packaging .....                             | 101 |
| 4.1. Package Design .....  | 101 |
| 4.2. Through Silicon Via (TSV).....                                | 105 |

|  |     |
|--|-----|
| 4.2.1. Deep Reactive Ion Etching (DRIE) .....        | 106 |
| 4.2.2. Physical Vapor Deposition (PVD).....          | 106 |
| 4.2.3. Electroplating.....                           | 108 |
| 4.3. Wafer Bonding .....                             | 113 |
| 4.3.1. Direct (Fusion Bonding).....                  | 114 |
| 4.3.2. Anodic Bonding.....                           | 115 |
| 4.3.3. Glass Frit Bonding.....                       | 116 |
| 4.3.4. Eutectic Bonding.....                         | 117 |
| 4.4. Process Flow.....                               | 119 |
| 4.5. Layout .....                                    | 123 |
| 5. Chapter V: Summary, Conclusion & Future Work..... | 125 |
| 5.1. Conclusion.....                                 | 130 |
| 5.3. Future Work .....                               | 132 |
| References.....                                      | 133 |

## List of Figures

|   |    |
|---|----|
| Figure 1-1: The Foucault pendulum, invented by Jean Bernard L'eon Foucault in 1851 as an experiment to demonstrate the rotation of the earth. The swinging direction of the pendulum rotates with time at a rate proportional to the sine of the latitude due to earth's rotation [1] . | 18 |
| Figure 1-2: Illustration of a conventional mechanical gyroscope and the three rotational degrees of freedom it can measure [2] .....  | 19 |
| Figure 1-3: A ball rolling from the center of a spinning disk is subjected to Coriolis acceleration and hence shows a curved trajectory [4] .....   | 20 |
| Figure 1-4: (a) The Coriolis effect. (b) Tuning-fork vibratory gyroscope. The tines are differentially driven to a fixed amplitude. Coriolis force is detected either as differential bending of the tuning-fork tines or as a torsional vibration of the tuning-fork stem [6].....     | 21 |
| Figure 1-5: Lumped model of MEMS gyroscope [4].....   | 21 |
| Figure 1-6: First MEMS gyroscope reported in the literature developed by Draper Labs [9]  | 24 |
| Figure 1-7: 2 <sup>nd</sup> generation of micromachined gyroscopes developed by Draper Labs in 1993 [10] .....  | 24 |
| Figure 1-8: Micromachined gyroscope developed by Murata Manufacturing in 1995 [11] ...  | 25 |
| Figure 1-9: First z-axis surface micromachined gyroscope developed at BSAC [12].....  | 25 |
| Figure 1-10: Micromachined gyroscope developed by Daimler Benz in 1997 [13].....  | 26 |
| Figure 1-11: Ring vibratory gyroscope [16] .....  | 27 |
| Figure 1-12: Dual axis surface micromachined gyroscope [19].....  | 27 |
| Figure 1-13: Gyroscope utilizing fish hook shape springs [20].....  | 28 |
| Figure 1-14: a) Drive mode. b) Sense mode [21].....   | 28 |
| Figure 1-15: MEMS gyroscope fabricated using a mix of surface and bulk micromachining [22]. .....   | 29 |
| Figure 1-16: a) lateral-axis CMOS MEMS gyroscope [23]. b) z-axis CMOS-MEMS gyroscope [24].....  | 29 |
| Figure 1-17: Double rotary lateral-axis rotation sensitive gyroscope [25].....  | 30 |
| Figure 1-18: 3 folded symmetric decoupled gyroscope [28].....   | 30 |
| Figure 1-19: a) Drive mode. b) Sense mode [28].....   | 31 |
| Figure 1-20: a) Micromachined gyroscope. b) 2 degree of freedom sense-mode oscillator [29] .....  | 31 |
| Figure 1-21: Lumped mass-spring-damper model and the frequency response of the overall 3-DOF gyroscope with 2-DOF sense-mode [29] .....   | 32 |

|  |    |
|--|----|
| Figure 1-22: Schematic of fully decoupled MEMS gyroscope [30] .....  | 32 |
| Figure 1-23: a) SEM of the double proof mass tuning fork gyroscope [32]. b) Sense Mode [31]. .....   | 33 |
| Figure 1-24: Schematic diagram of the capacitive silicon spoke gyroscope [35] .....  | 33 |
| Figure 1-25: Schematic of the quasi-digital gyroscope based on mechanical Frequency Modulation of the input rate [36] .....  | 34 |
| Figure 2-1: 3 folded symmetric decoupled gyroscope [28].....   | 36 |
| Figure 2-2: 3D structure of the vertical suspension system gyroscope.....  | 38 |
| Figure 2-3: 3D structure of the hybrid suspension system gyroscope. ....   | 39 |
| Figure 2-4: Top view of the hybrid suspension system gyroscope.....  | 40 |
| Figure 2-5: Origin of the parasitic capacitance between the drive/sense comb-drive and proof mass in vertical suspension version.....  | 40 |
| Figure 2-6: A model of the gyroscope showing set of springs with a constant $k$ , a voltage source, and initial distances; the dark green area is fixed and the light green shaded area is moving; $C^+$ and $C^-$ are the sense capacitances generated between the fixed and moving structures of the comb-drive pair. The combs are all $h$ thick (see text for details).....  | 41 |
| Figure 2-7: Voltage divider. Most famous scheme for getting rid of the electrical coupling .   | 42 |
| Figure 2-8: Various decoupling mechanisms to achieve mechanical decoupling. (a) In the “no decoupling” case there is a continuous bias coupled to the sense mode and the drive-mode linearity is disturbed. (b) Decoupled-drive-mode removes the non-linearity but not the sense mode bias. The configuration in (c) completely solves both non-linearity and unwanted sense-mode bias. [28] .....   | 43 |
| Figure 2-9: Beam cross-section.....  | 44 |
| Figure 2-10: a) Drive mode resonance frequency 3117 Hz. b) sense mode resonance frequency 3119 Hz .....  | 45 |
| Figure 2-11: a) Drive mode resonance frequency 4964 Hz. b) sense mode resonance frequency 4953 Hz .....  | 47 |
| Figure 2-12: Effect of drive and sense modes mismatch on the output signal [1].....  | 49 |
| Figure 2-13: A conceptual model of a comb drive actuator showing a damper with damping coefficient $D$ , a spring with a constant $k$ , a voltage source (DC and AC), and pertinent distances; the black shaded area is fixed and the gray shaded area is moving; $C_t$ is the transverse capacitance generated between the fixed and moving structures, while $C_l$ is the longitudinal capacitance generated the combs. The combs are all $h$ thick (see text for details) ..... | 50 |

|  |    |
|--|----|
| Figure 2-14: Solution methodology (dark gray blocks represent the Simulink Domain; white and light gray blocks represent Matlab Domain). The first lines written in light gray boxes are responsible for the sweep up, while the second lines written are responsible for the sweep down. .... | 55 |
| Figure 2-15: The spring-damper equation, (b) the electrostatic force, and (c) the electrostatic force.....   | 56 |
| Figure 2-16: Comparing the proposed solution with the measured results from Nguyen and Howe in [44]. Graph taken from [52]......   | 59 |
| Figure 2-17: The hardening response of the resonator in [44] obtained by using the proposed analysis. Graph taken from [51]......  | 59 |
| Figure 2-18: The measurement results of the output current of the resonator as presented in [44]. Note the similarities between that the measurements in this figure and the theoretical results shown in Fig. 2-17 above.....   | 60 |
| Figure 2-19: The double-sided response for various DC excitation voltages applied to the vertical suspension gyroscope.....  | 61 |
| Figure 2-20: The double-sided response for various AC excitation voltages applied to the vertical suspension gyroscope.....  | 62 |
| Figure 2-21: The double-sided response for various $X_0$ values for the vertical suspension gyroscope.....   | 62 |
| Figure 2-22: The double-sided response for various DC excitation voltages applied to the hybrid suspension gyroscope.....  | 63 |
| Figure 2-23: The double-sided response for various AC excitation voltages applied to the hybrid suspension gyroscope.....  | 63 |
| Figure 2-24: The double-sided response for various $X_0$ values for the hybrid suspension gyroscope.....   | 64 |
| Figure 2-25: The double-sided response for various DC excitation voltages applied to the hybrid suspension gyroscope. However, $x_0 = 7\mu\text{m}$ instead of $10\mu\text{m}$ . ....  | 65 |
| Figure 3-1: Vertical suspension system 3D model. a) Front-side snapshot. b) Back-side snapshot. c) Back-side snapshot for vertical beams defined from three sides only (no Contacts etching). ....   | 71 |
| Figure 3-2: Electrical connection to the proof-mass in the vertical suspension design. ....  | 72 |
| Figure 3-3: a) SOI wafer ( $100\mu\text{m}$ device wafer, $1\mu\text{m}$ $\text{SiO}_2$ , and $500\mu\text{m}$ handle layer). b) Coating wafer with positive photoresist (PR) on spinner.....  | 72 |
| Figure 3-4: a) print Contacts mask. b) Etch $100\mu\text{m}$ Si in DRIE.....   | 73 |

|   |    |
|---|----|
| Figure 3-5: a) Etch intermediate SiO <sub>2</sub> in DRIE. b) Etch 400 $\mu$ m Si in DRIE. ....   | 73 |
| Figure 3-6: a) Strip photoresist using Acetone. b) Deposit poly SiGe in LPCVD. ....   | 73 |
| Figure 3-7: a) Spray coat photoresist (PR). b) Print Fingers mask. ....   | 73 |
| Figure 3-8: a) Etch SiGe film in DRIE. b) Etch 100 $\mu$ m Si in DRIE.....  | 73 |
| Figure 3-9: a) Spin photoresist on the wafer backside. b) Print Isolation mask. ....  | 74 |
| Figure 3-10: a) Etch 30 $\mu$ m Si in DRIE. b) Strip photoresist using Acetone. ....  | 74 |
| Figure 3-11: a) Spray coat photoresist. b) Print Suspension mask. ....  | 74 |
| Figure 3-12: a) Etch 470 $\mu$ m Si in DRIE (Cross-section of the completed device). b)<br>Frontside SEM photo of the fabricated device.....  | 74 |
| Figure 3-13: Fingers mask (light blue; light field) and Contacts (green; dark field).....   | 75 |
| Figure 3-14: Contacts mask (green; dark field), Fingers (light blue; light field), Isolation<br>(stripes; dark field), and Suspension (dark green; dark field).....                 | 75 |
| Figure 3-15: Fingers mask (light blue; light field) and Metallization (dark blue; light field). 76  |    |
| Figure 3-16: Layout of vertical suspension system based gyroscope. ....   | 76 |
| Figure 3-17: Electrical signal connection using through handle wafer in vertical suspension<br>version. ....  | 77 |
| Figure 3-18: Electrical connection to the proof-mass in the hybrid suspension design.....   | 77 |
| Figure 3-19: Origin of the parasitic capacitance between the drive/sense comb-drive and<br>proof mass in vertical suspension version. ....  | 78 |
| Figure 3-20: a) SOI wafer (100 $\mu$ m device wafer, 1 $\mu$ m SiO <sub>2</sub> , and 500 $\mu$ m handle layer). b)<br>Coating wafer with positive photoresist (PR) on spinner..... | 78 |
| Figure 3-21: a) Print Fingers mask. b) Etch 100 $\mu$ m Si. ....  | 78 |
| Figure 3-22: a) Etch 1 $\mu$ m SiO <sub>2</sub> . b) Etch 400 $\mu$ m Si. ....  | 79 |
| Figure 3-23: a) Strip photoresist. b) Spin photoresist on substrate backside.....   | 79 |
| Figure 3-24: a) Print Suspension mask. b) Etch 500 $\mu$ m Si. ....   | 79 |
| Figure 3-25: Strip photoresist (Cross-section of the completed device). ....  | 79 |
| Figure 3-26: a) Fingers mask (light field). b) Contacts mask (dark field).....  | 80 |
| Figure 3-27: Layout of hybrid suspension system based gyroscope.....  | 80 |
| Figure 3-28: Hybrid (vertical and horizontal) suspension system. ....   | 81 |
| Figure 3-29: Black Silicon formed at 13 sccm O <sub>2</sub> , 100 sccm SF <sub>6</sub> at 120°C .....   | 82 |
| Figure 3-30: Undercut formed after 64 minute etching at 120°C and variable O <sub>2</sub> to SF <sub>6</sub><br>concentrations .....  | 83 |
| Figure 3-31: Wet isotropic etching on reduces the resolution .....  | 84 |



|   |    |
|---|----|
| Figure 3-32: SEM of cantilevers showing the high intrinsic stresses associated with Cu film .....   | 84 |
| <b>Figure 3-33: Undercut which destroyed critical features of the structures</b> .....  | 84 |
| Figure 3-34: a) Negative profile generated after 60' etching at 9 sccm O <sub>2</sub> , 100 sccm SF <sub>6</sub> and -120°C. b) Positive profile generated by decreasing SF <sub>6</sub> , content to 90 sccm.....  | 85 |
| Figure 3-35: a) Positive profile generated at 11 sccm O <sub>2</sub> content and 100 sccm SF <sub>6</sub> at -100°C. b) Profile became less positive by reducing O <sub>2</sub> content to 10 sccm.....   | 85 |
| Figure 3-36: a) Further reduction of O <sub>2</sub> to 9 sccm while adjusting SF <sub>6</sub> to 90 sccm at -120°C results in more straight profile. b) Increasing O <sub>2</sub> content beyond 13% at -120°C results in black silicon formation .....   | 86 |
| Figure 3-37: a) A slightly positive profile at -120°C and 9 sccm O <sub>2</sub> , 90 sccm SF <sub>6</sub> . b) Profile became less positive by increasing the temperature -115°C .....  | 86 |
| Figure 3-38: a) Loss of mask after 60 minute etching at 5 W RF power, 6 sccm O <sub>2</sub> , 90 sccm SF <sub>6</sub> , and -140°C. b) Also negative profile is observed at same conditions in Fig. 3-36-a.....   | 87 |
| Figure 3-39: a) Undercutting and damage of mask after 30' minute etching, at 10 W RF power and 6 sccm O <sub>2</sub> , 90 sccm SF <sub>6</sub> , -140°C. b) Complete sidewall damage when RF power was increased to 15 W and 6 sccm O <sub>2</sub> , 90 sccm SF <sub>6</sub> , -140°C .....     | 87 |
| Figure 3-40: a) at 1000 W ICP power, a negative profile started to form (9 sccm O <sub>2</sub> , 90 sccm SF <sub>6</sub> , 60" 4 W, -120°C). b) at 900 W ICP power, profile is more straight (6 sccm O <sub>2</sub> , 90 sccm SF <sub>6</sub> , 60" 5 W, -140°C).....                           | 87 |
| Figure 3-41: Profile of a DRIE trench using the Bosch process. The process cycles between an etch step using SF <sub>6</sub> gas and a polymer deposition step using C <sub>4</sub> F <sub>8</sub> . The polymer protects the sidewalls from etching by the reactive fluorine radicals [2]..... | 90 |
| Figure 3-42: Schematic drawing of the spray coating [58] .....  | 92 |
| Figure 3-43: Chemical Vapor Deposition working principle diagram [59] .....   | 93 |
| Figure 3-44: SEM of the front-side vertical suspension gyroscope after etching Contacts and Fingers mask .....  | 95 |
| Figure 3-45: SEM of back-side of vertical suspension gyroscope after Suspension etching. Without etching front-side .....   | 96 |
| Figure 3-46: SEM of back-side of vertical beam that's fully defined by etching both Contacts and Suspension masks .....   | 96 |
| Figure 3-47: SEM of front-side of the hybrid suspension gyroscope .....   | 97 |
| Figure 3-48: SEM of back-side of hybrid suspension gyroscope .....  | 97 |
| Figure 3-49: Resonance frequency measurement setup .....  | 98 |

|  |     |
|--|-----|
| Figure 3-50: Sense mode frequency response .....   | 99  |
| Figure 3-51: Drive mode frequency response.....  | 100 |
| Figure 4-1: a) Fabricated MEMS device on Si wafer. b) Deposition and patterning of sacrificial layer. c) Deposition of sealing layer. d) Patterning sealing layer to define the release holes. e) Etching the sacrificial layer. f) Sealing the release holes under vacuum conditions. g) SEM taken at step number (e) for a microencapsulated MEMS device [60]. | 102 |
| Figure 4-2: Device wafer with two cap wafers (lower and upper). Green is the adhesive layer, blue is copper pads .....   | 104 |
| Figure 4-3: Schematic for metal line route on gyroscope. ....  | 104 |
| Figure 4-4: a) Conventional packaging using wire bonding [60]. b) Wafer level packaging using TSV [60].....  | 105 |
| Figure 4-5: Cu film sputtered on Si substrate directly without any adhesive layers peeled off during rinsing in deionized water.....   | 107 |
| Figure 4-6: Electroplating setup for Cu deposition [60]. ....  | 109 |
| Figure 4-7: a) TSV formed in the cap wafer then wafer bonded to the device wafer. b) Seed layer deposited using PVD then the stack was connected as the cathode in the electroplating setup.....   | 110 |
| Figure 4-8: a) Cu electroplating. b) Metal pads patterining through wet etching.....   | 110 |
| Figure 4-9: SEM photo showing sputtered Ti film only covering wafer surface. ....  | 111 |
| Figure 4-10: EDX scans showing no sign of Ti on the trench sidewalls (a) and trench bottom (b). ....   | 111 |
| Figure 4-11: a) Printing areas of TSV on high resistivity Si wafer. b) After etching Si wafer, seed layer grown on the backside of the wafer and served as the cathode in the electroplating process .....   | 112 |
| Figure 4-12: a) Electroplating Cu. b) Patterning backside Cu seed layer using wet etching and bond cap and device wafers together.....   | 112 |
| Figure 4-13: TSV filled with Cu after electroplating. It's notable that the electroplating process is selective to TSV other than Si surface. ....   | 113 |
| Figure 4-14: Anodic bonding diagram [74].....  | 115 |
| Figure 4-15: Phase diagram for the gold-silicon system [88].....   | 118 |
| Figure 4-16: a) High resistivity double side polished Si wafer with Au evaporated on the backside. b) Spin Photoresist (PR) on the front-side.....   | 120 |
| Figure 4-17: a) Print TSV mask. b) Si etching through wafer till gold film is reached. ....  | 120 |
| Figure 4-18: a) Cu electroplating. b) Strip positive photoresist in Acetone. ....  | 120 |

|  |     |
|--|-----|
| Figure 4-19: a) Deposit Cu film using RF Magnetron Sputtering. b) Spin positive photoresist AZ 9260. ....  | 120 |
| Figure 4-20: a) Print Metallization mask. b) Cu wet etching in 5% ammonium persulfate..                    | 120 |
| Figure 4-21: a) Strip photoresist in Acetone. b) Spin Spin positive photoresist AZ 9260....                | 121 |
| Figure 4-22: a) Print Frontside Paste mask. b) Wet etch Au. ....   | 121 |
| Figure 4-23: a) Strip photoresist in Acetone. b) Spin positive photoresist AZ 9260 on the backside. ....   | 121 |
| Figure 4-24: a) Print Frontside Cavity mask. b) Etch Si in DRIE for 50 $\mu\text{m}$ . ....                | 122 |
| Figure 4-25: a) Strip photoresist in Acetone. b) Align Upper Cap wafer with Device wafer. ....             | 122 |
| Figure 4-26: a) Bond two wafers under vacuum conditions. b) Align Lower Cap wafer with Device Wafer. ....  | 122 |
| Figure 4-27: Bond stack wafers with Lower Cap wafer under vacuum conditions. ....                          | 123 |
| Figure 4-28: Fingers Mask (Blue); Frontside Paste (Grey); Frontside Cavity (Stripes); and TSV (Blue). .... | 123 |
| Figure 4-29: Fingers Mask (Blue); Backside Paste (Green). ....   | 124 |
| Figure 5-1: SEM of back-side of hybrid suspension gyroscope .....  | 128 |
| Figure 5-2: Measured frequency response: a) Sense mode. b) Drive mode .....                                | 128 |
| Figure 5-3: TSV after Cu filling by electroplating process .....   | 129 |

## List of Tables

|  |     |
|--|-----|
| Table 1-1: Performance requirements for different classes of gyroscopes [6] .....                  | 22  |
| Table 2-1: Summary of vertical suspension gyroscope dimensions and properties .....                | 46  |
| Table 2-2: Summary of hybrid suspension gyroscope dimensions and properties .....                  | 48  |
| Table 2-3: Parameters used to obtain the plots in Figs. 2-16 and 2-17. ....                        | 58  |
| Table 2-4: Parameters values used for simulating both architectures. ....                          | 61  |
| Table 2-5: Comparison between the vertical gyroscope, hybrid gyroscope, and state of the art ..... | 68  |
| Table 3-1: Buried Oxide Etching Recipe .....   | 91  |
| Table 3-2: Bosch Process Used for Etching Si .....   | 91  |
| Table 3-3: Optimized photoresist spinning parameters .....   | 92  |
| Table 3-4: Optimized spray coating parameters .....  | 92  |
| Table 3-5: Optimized LPCVD SiGe deposition parameters .....  | 94  |
| Table 3-6: Measured gyroscope dimensions in micro-meters .....                                     | 99  |
| Table 3-7: Frequency response results .....  | 100 |
| Table 4-1: Optimized Cu sputtering parameters .....  | 108 |
| Table 4-2: Optimized process for Cu electroplating temperature .....                               | 109 |
| Table 5-1: Comparison between the vertical gyroscope, hybrid gyroscope, and state of the art ..... | 126 |

## List of Abbreviations

|         |   |
|---------|---|
| 3D      | Three Dimensions                          |
| 3-FSG   | Three Folded Symmetric Gyroscope          |
| AC      | Alternating Voltage                       |
| ARW     | Angle Random Walk                         |
| AUC     | American University in Cairo              |
| BSAC    | Berkley Sensors and Actuators             |
| BW      | Bandwidth                                 |
| CalTech | California Institute of Technology        |
| CD      | Comb-Drive                                |
| CMOS    | Commentary Metal-Oxide-Semiconductor      |
| DC      | Direct Voltage                            |
| DFT     | Discrete Fourier Transform                |
| DOF     | Degree of Freedom                         |
| DRIE    | Deep Reactive Ion Etching                 |
| EDX     | Energy Dispersive X-Ray                   |
| FEA     | Finite Element Analysis                   |
| IC      | Integrated Circuits                       |
| ICP     | Inductively Coupled Plasma                |
| MEMS    | Micro-Electro-Mechanical Systems          |
| MNEΩ    | Mechanical Noise Equivalent Angular Rate  |
| PECVD   | Plasma Enhanced Chemical Vapor Deposition |
| PMAFF   | Proof Mass Area Fill Factor               |
| PR      | Photoresist                               |
| PVD     | Physical Vapor Deposition                 |
| RF      | Radio Frequency                           |
| SEM     | Scanning Electron Microscope              |
| SNR     | Signal to Noise Ratio                     |
| SOI     | Silicon-On-Insulator                      |
| TSV     | Through Silicon Via                       |
| UCI     | University of California Irvine           |
| UCLA    | University of California Berkley          |

|         |  |
|---------|--|
| UV      | Ultraviolet  |
| VMG     | Vibratory MEMS Gyroscope                             |
| WLP     | Wafer Level Packaging                                |
| YJ-STRC | Yousef Jameel Science and Technology Research Center |
| ZRO     | Zero-Rate Output                                     |

## 1. Chapter I: Introduction

Gyroscopes are mechanical devices used to sense rotation around any of the 3 principal-axis (x, y, and z). The word gyroscope came from two Greek words: Skopeein (to see) and Gyros (circle or rotation) [1]. The first gyroscope was a pendulum (see Fig. 1-1) built by Foucault in 1851 to demonstrate the rotation of the earth [1]. Foucault experiment was based on swinging a hanged mass (from the top of a building) causing harmonic motion. As the object mass was supposed to be affected by the forces of gravity and inertia, its harmonic motion should have been fixed to a certain direction. However, they found that the mass motion has a component in the perpendicular direction. This proved that the frame, the pendulum is suspended to, is under angular motion. Hence, the earth, the building is built on, is rotating.



**Figure 1-1: The Foucault pendulum, invented by Jean Bernard L'eon Foucault in 1851 as an experiment to demonstrate the rotation of the earth. The swinging direction of the pendulum rotates with time at a rate proportional to the sine of the latitude due to earth's rotation [1]**

Earliest mechanical, rotating wheel shown in Fig. 1-2, gyroscopes were developed based on the Coriolis' Effect. These types of gyroscopes were used in airplanes for maintaining their orientation during the flight. The device is based on a rotating wheel around an inner gimbal axis. This inner gimbal has only one degree of freedom. The latter gimble is connected to an outer gimbal that also has one degree of freedom (yet perpendicular to the inner gimbal) through a pivot. If the outer gimbal was applied to an input rotation, a rotation would observe in the inner gimbal ring due to the Coriolis' Force.

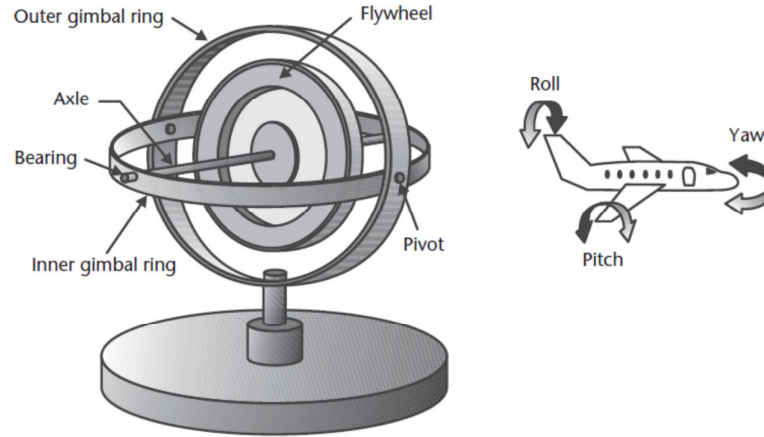


**Figure 1-2: Illustration of a conventional mechanical gyroscope and the three rotational degrees of freedom it can measure [2]**

This chapter first introduces gyroscopes and the physical theory behind it, which is the Coriolis' Effect. Then, the utilization of Micro-Electro-Mechanical Systems and micromachining technology to miniaturization of mechanical gyroscopes is introduced. This introduction is accompanied with the applications of MEMS gyroscopes and the figures of merits used to measure its performance. After that, a concise survey of the previously reported gyroscopes in literature and considered as milestones in the industry is given. Finally, the last section highlights the major limitations for the existing micromachined gyroscopes and demonstrates the need for a novel architecture that alleviates the short falls of current architecture. Developing such architecture is the main motivation behind the work presented in this study, and explores the thesis roadmap.

### **1.1. Mechanical Gyroscopes and Coriolis' Effect**

A French physicist called Gaspard Gustave Coriolis in 1835 derived, mathematically, the fictitious force (named after him as Coriolis' Force) which is applied to moving objects in a rotating frame [3]. This phenomenon can be demonstrated by passing a ball between two fixed points on a rotating wheel as shown in Fig. 1-3.



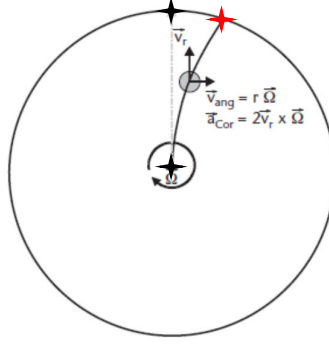


**Figure 1-3: A ball rolling from the center of a spinning disk is subjected to Coriolis acceleration and hence shows a curved trajectory [4]**

The mathematical expression for the Coriolis' Force,  $F_c$ , is:

$$F_C = -2m\Omega \times v \quad (1-1)$$

Where  $m$  is the mass of the moving object,  $v$  its velocity, and  $\Omega$  is the angular rotation of the frame.

Non-mechanical high performance gyroscopes such as Fiber-Optic Gyroscope (FOG) [5] and Ring Laser Gyroscope (RLG) [5] were developed based on a physical phenomenon named Sagnac Effect [5]. However, these types of gyroscopes are out of this thesis focus. The next section introduces Micro-Electro-Mechanical Systems and explores the miniaturization of mechanical gyroscopes by utilizing the micromachining technology.

#### MEMS Vibratory Gyroscopes

MEMS stands for Micro-Electro-Mechanical Systems. It's a technology that realizes mechanical structures, with features in the micron scale, and integrates them with standard integrated electronic circuits (IC's) to make a full system. Over the last two decades, MEMS technology delivered several devices to the world of sensors and actuators that were integrated in numerous applications such as military, aerospace, automotive, optics, biomedical, energy harvesting, etc. [2].

Using MEMS technology to realize a mechanical gyroscope results in reducing the foot-print of the rotation sensor to a limit that allows their integration inside portable devices. The basic operation principle of mechanical gyroscope is based on the tuning fork concept [6]. The vibrating element of the fork suspended to a rotating frame would lead to the generation of the Coriolis' force acting on the element and cause a displacement in the perpendicular direction (see Fig. 1-4). This displacement can be sensed by means of capacitors, piezoelectric, or piezoresistive elements.

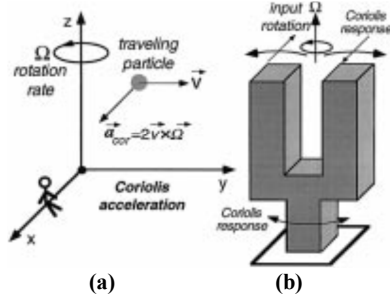


**Figure 1-4: (a) The Coriolis effect. (b) Tuning-fork vibratory gyroscope. The tines are differentially driven to a fixed amplitude. Coriolis force is detected either as differential bending of the tuning-fork tines or as a torsional vibration of the tuning-fork stem [6]**

An example of a general MEMS gyroscope principle operation is illustrated in Fig. 1-5. A proof mass, free to move, is suspended to a fixed frame with four springs where the drive mode is in the x-axis, sense mode in the y-axis and the input rotation is around z-axis.

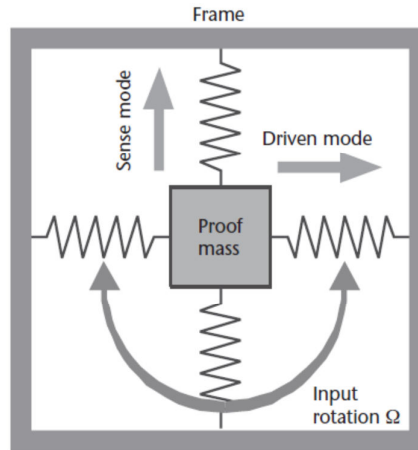


**Figure 1-5: Lumped model of MEMS gyroscope [4]**

The behavior of the mass-spring-damping system for drive and sense modes are described by the famous equations of motion shown in Eqs. (1-2) and (1-3) respectively [1]:

$$m\ddot{x} + D\dot{x} + kx = F \quad (1-2)$$

$$m\ddot{y} + D\dot{y} + ky + 2m\Omega\dot{x} = 0 \quad (1-3)$$

Where  $m$  is the weight of the proof mass,  $x$  is the displacement in the drive mode,  $y$  is the displacement in the sense mode,  $D$  is the damping factor,  $k$  is the spring constant,  $\Omega$  is input angular rotation, and  $F$  is the driving force.

### 1.1.1. Performance Measures

The figures of merit that define the performance of vibratory gyroscopes are stated in the IEEE Standard Specification Format Guide and Test Procedure for Coriolis Vibratory Gyros [7] while important specifications and definitions are available at IEEE Standard for Inertial Sensor Terminology [8].

The most important factors in measuring the performance of MEMS gyroscope are Resolution, drift, zero-rate output (ZRO), and scale factor. In the absence of input rotation, the output signal of a gyroscope is a random function that is the sum of white noise and a slowly varying function [6]. The white noise defines the resolution of the sensor and is expressed in terms of the standard deviation of equivalent rotation rate per square root of bandwidth of detection [ $(^\circ/\text{s})/\text{Hz}$  or  $(^\circ/\text{h})/\text{Hz}$ ]. Some angular rate sensors are used to track the change in angles not angular rate, therefore, the angular rate signal is integrated to calculate angle changes. In latter case, the “angle random walk” (ARW) in  $^\circ/\sqrt{\text{h}}$  may be used instead. The ARW is defined to calculate the output noise resulted in the integrated signal. The term random walk is defined in statistics when the output of the system is driven by random, uncorrelated steps (in the case of rotating gyroscope these steps are angles). The peak-to-peak value of the slowly varying function defines the short- or long-term drift of the gyroscope and is usually expressed in  $^\circ/\text{s}$  or  $^\circ/\text{h}$  [6]. Scale factor is defined as the amount of change in the output signal per unit change of rotation rate and is expressed in  $\text{V}/(^\circ/\text{s})$ . Last, an important factor for any gyroscope that is primarily defined by device imbalances is the ZRO, which represents the output of the device in the absence of a rotation rate [6].

Gyroscopes are categorized into three classes based on their performance [6]. These classes are Rate Grade, Tactical Grade, and Inertial Grade. Table 1-1 shows the different parameters requirements for each class.

**Table 1-1: Performance requirements for different classes of gyroscopes [6]**

| <b>Parameter</b>                           | <b>Rate Grade</b> | <b>Tactical Grade</b> | <b>Inertial Grade</b> |
|--|-------------------|-----------------------|-----------------------|
| Angle Radom Walk, $^\circ/\sqrt{\text{h}}$ | $>0.5$            | $0.5-0.05$            | $<0.001$              |
| Bias Drift, $^\circ/\text{h}$              | $10-1000$         | $0.1-10$              | $<0.01$               |
| Scale Factor Accuracy, %                   | $0.1-1$           | $0.01-0.1$            | $<0.001$              |
| Full Scale Range ( $^\circ/\text{sec}$ )   | $50-1000$         | $>500$                | $>400$                |
| Max. Shock in 1msec, g's                   | $10^3$            | $10^3-10^4$           | $10^3$                |
| Bandwidth, Hz                              | $>70$             | $\sim 100$            | $\sim 100$            |

Also, Bandwidth ( $BW$ ) is an important factor, which is the range of frequency of the angular rate input that the gyroscope can detect. Typically specified as the cutoff frequency coinciding to the -3dB point. Equations (1-4) - (1-6) shows the way of calculating the  $BW$ .

$$\omega_0 = \sqrt{k/m} \quad (1-4)$$

$$Q = \sqrt{km}/D \quad (1-5)$$

$$BW = \frac{\omega_0}{Q} \quad (1-6)$$

Where the  $\omega_0$  is the resonance frequency of the harmonic oscillation and  $Q$  is the quality factor.

Reliability requirements such as turn on time, shock resistance, operating life, operating temperature range, thermal shock, thermal cycling, humidity, electrostatic discharge immunity, and electromagnetic emissions and susceptibilities are also required to be measured for many applications.

### 1.1.2. Applications

The conventional rotating wheel gyroscope is too big and RLG and FOG is too expensive while MEMS gyroscopes are small, precise, high sensitivity, and low power consumption. Moreover, the batch-fabrication of the micromachining technology makes the MEMS gyroscopes extremely cheap. This low cost due to the fabrication of hundreds (even thousands) of devices on a single wafer with the same running cost. Hence, MEMS gyroscopes are becoming more and more attractive to be integrated in many applications [1].

MEMS gyroscopes are currently integrated in the controllers of game consoles to add a realistic sense to the player. Also, they are integrated in smart phones and tablets. Moreover, MEMS gyroscopes are used in automotive industry for electronic stability control and navigation. Image stabilizations in digital cameras is done with the aid integrated MEMS gyroscopes. In addition, high performance gyroscopes are used in aerospace and military applications.

### 1.1.3. Literature Survey

The first micromachined vibratory gyroscope was developed by Draper lab in 1991 [9]. This gyroscope had a noise limited rate detection capability of 4 deg/sec at 1 Hz bandwidth. The device consists of two gimbals of single crystal silicon suspended by torsional flexures and

the inertial mass is made of gold as seen in Fig. 1-6. The device operation was limited due to the small proof-mass and small driving deflections.

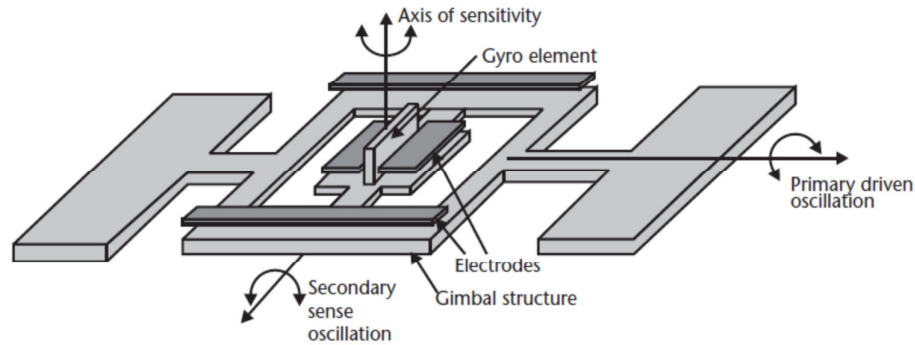


Figure 1-6: First MEMS gyroscope reported in the literature developed by Draper Labs [9]

After two years, Draper labs introduced the second generation of gyroscopes built using poly silicon material which is more readily interfaced with low cost electronics [10]. The device utilized comb-drive structure for realizing linear capacitance for electrostatic force generation as shown in Fig. 1-7. Resolution of  $1 \text{ deg/sec}/\sqrt{\text{Hz}}$  was achieved. This device was fabricated using another two different technologies rather than the polysilicon surface micromachining. The first, is the silicon on glass substrates which realizes low stray capacitance, however, it's not compatible with CMOS electronics ICs. The second is Ni electroforming on Si substrates. However, this technology was rejected by the authors due to the huge support losses made of electroformed Ni, which limits the mechanical quality factor to 1000.

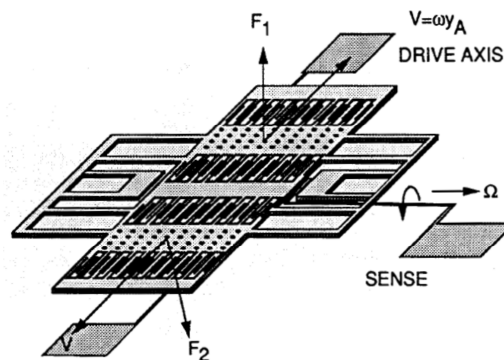


Figure 1-7: 2<sup>nd</sup> generation of micromachined gyroscopes developed by Draper Labs in 1993 [10]

Murata manufacturing reported polysilicon surface micromachined gyroscope (shown in Fig. 1-8) in 1995 [11]. This gyroscope was operated under vacuum of pressures of 0.1 Pa achieving mechanical quality factors of 2,800 and 16,000 for drive and sense modes

respectively with resonance frequencies of 13 KHz. The gyroscope had a noise equivalent rate of 7deg/sec. This device uses surface micromachining technology which allows small sense capacitance that reduces the device sensitivity.

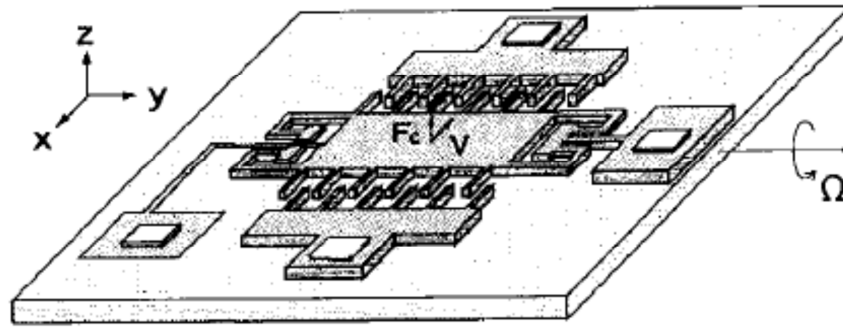


Figure 1-8: Micromachined gyroscope developed by Murata Manufacturing in 1995 [11]

R. T. Howe et al at Berkley Sensors and Actuators Center (BSAC) reported in [12] the first surface micromachined polysilicon gyroscope that sense the rotation around the z-axis as illustrated in Fig. 1-9. As the previous designs were sensing rotation of in-plane axes (x and y), the integration of this gyroscope with lateral axis gyroscopes allows fabrication of an axis gyroscope on a single chip. However, it can be seen from Fig. 1-9, the architecture had small proof-mass which would reduce the device operation. This forced the authors used long lateral suspension beams to resolve the issue. However, these lateral beams occupy large area of the device.

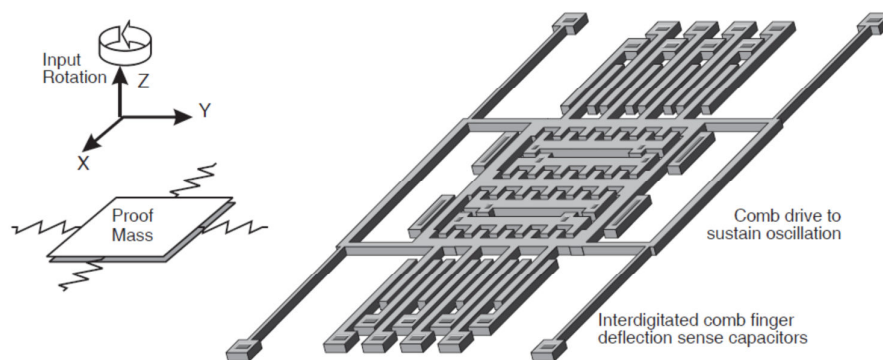


Figure 1-9: First z-axis surface micromachined gyroscope developed at BSAC [12]

Daimler Benz introduced in 1997 a novel design of tuning fork based MEMS vibratory gyroscope [13]. In this design, the tines of the fork are perpendicular to the wafer surface as shown in Fig. 1-10. Also, in contrast to the previous designs, the driving mode was excited

using a piezoelectric material and the output signal is sensed by piezoresistive material instead of parallel plate, or comb-drive capacitors. Although Benz gyroscope proved high performance, it required utilization of sophisticated and expensive processes for its fabrication such as Silicon direct bonding. Also, it worth mentioning that this process is performed at elevated temperatures of  $\sim 1000^{\circ}\text{C}$ .

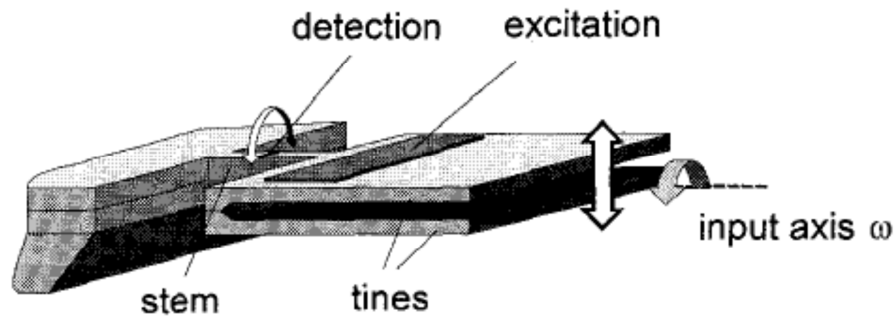


Figure 1-10: Micromachined gyroscope developed by Daimler Benz in 1997 [13]

In 1997, Robert Bosch GmbH reported a z-axis gyroscope that was driven using a magnet mounted below which allows driving displacement up to  $50\text{ }\mu\text{m}$  [14]. Moreover, the latter design attempted to decouple the sense and drive mode from each other through a differential reading of the outputs of the two sensing elements.

The idea of ring vibratory gyroscope shown in Fig. 1-11 was introduced in the literature [15, 16, 17]. The principle operation relies on the presence of two identical elliptical shaped resonance modes of the same resonance frequencies and separated with  $45^{\circ}$ . These two modes are the sense and the drive mode. The Coriolis' force is sensed capacitively through the sense electrodes shown in Fig. 1-11. A resolution of  $0.01\text{ deg/sec}/\sqrt{\text{Hz}}$  achieved in [16]. This architecture allows small drive amplitude which limits its sensitivity.

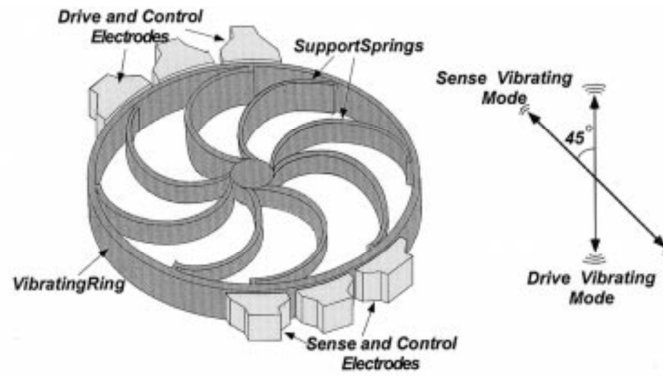


Figure 1-11: Ring vibratory gyroscope [16]

In 1997 California Institute of Technology (CalTech) and University of California Los Angeles (UCLA) developed together high performance MEMS gyroscope for space applications with bias resolution of  $70 \text{ deg/hr}/\sqrt{\text{Hz}}$  and scale factor of  $24 \text{ mV/deg/sec}$  [18]. The symmetrical design provided a mismatch between the drive and sense mode resonance frequencies of 7 Hz. However, the realization of this device required assembling a metal post inside a hole in the device and wafer bonding.

Pisano et al developed at BSAC and with the cooperation with Sandia labs in 1997 the first dual axis surface micromachined gyroscope (see Fig. 1-12-a) [19]. The operating principle is based on the angular oscillation of a circle inertial rotor (see Fig. 1-12-b) while any input rotation around the y-axis would induce a shift of the rotor in the x-direction and vice versa. Cross axis sensitivity ranged from 3-16%.

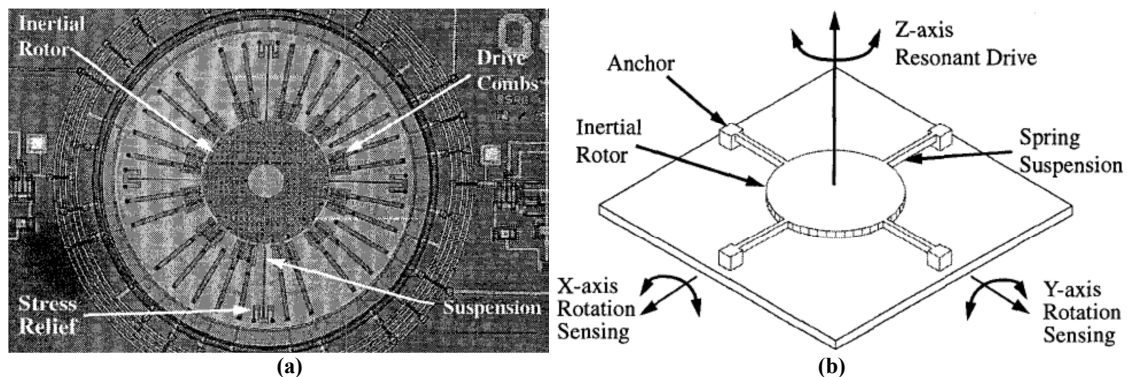


Figure 1-12: Dual axis surface micromachined gyroscope [19]

Samsung introduced to the industry in [20] the use of fish hook shape springs. These springs (see Fig. 1-13) provides high stiffness, in directions other than the desired one, which enhances the mechanical robustness against shock. Also, it can be seen from the architectures



that it suffers from small proof mass area fill factor due to the long in-plane lateral suspension system.

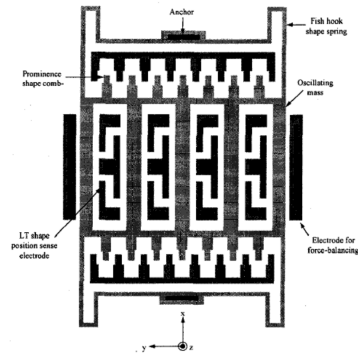


Figure 1-13: Gyroscope utilizing fish hook shape springs [20]

The micromachined gyroscope based on gimbal configuration, as shown in Fig. 1-14, inherently decouple mechanically the sense and the drive mode completely [21]. However, matching the resonance frequencies of the drive and sense modes stand as an issue due to the mismatch between the drive and sense proof masses.

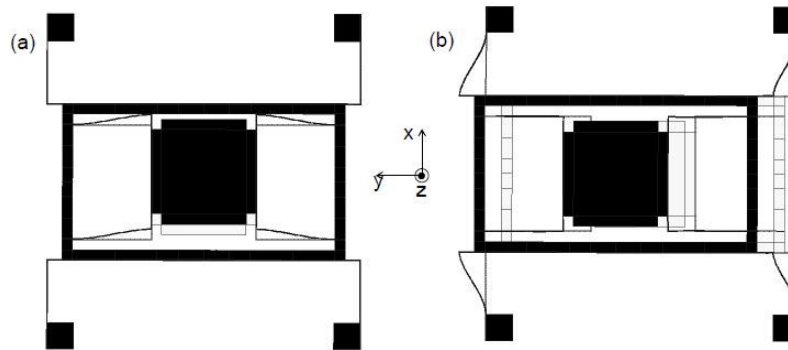


Figure 1-14: a) Drive mode. b) Sense mode [21]

Seoul National University developed in 2000 MEMS gyroscope (cf. Fig. 1-15) that's fabricated using a mix surface and bulk micromachining technology [22]. This design achieved a resolution of 9 deg/sec/ $\sqrt{\text{Hz}}$ .

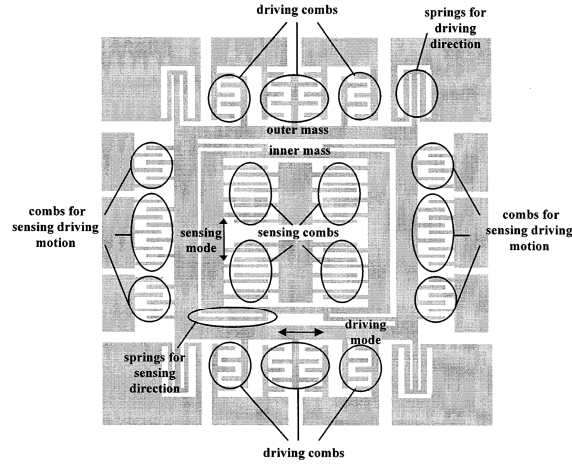


Figure 1-15: MEMS gyroscope fabricated using a mix of surface and bulk micromachining [22].

Fedder *et al.* at the Carnegie Mellon University demonstrated for the first time the realization of a lateral [23] and z-axis [24] CMOS gyroscopes. The devices (shown in Fig. 1-16) were fabricated using post-CMOS micromachining in 2001. However, the structures of the gyroscopes suffered from, observable, residual stress which limited the sizes of the features.

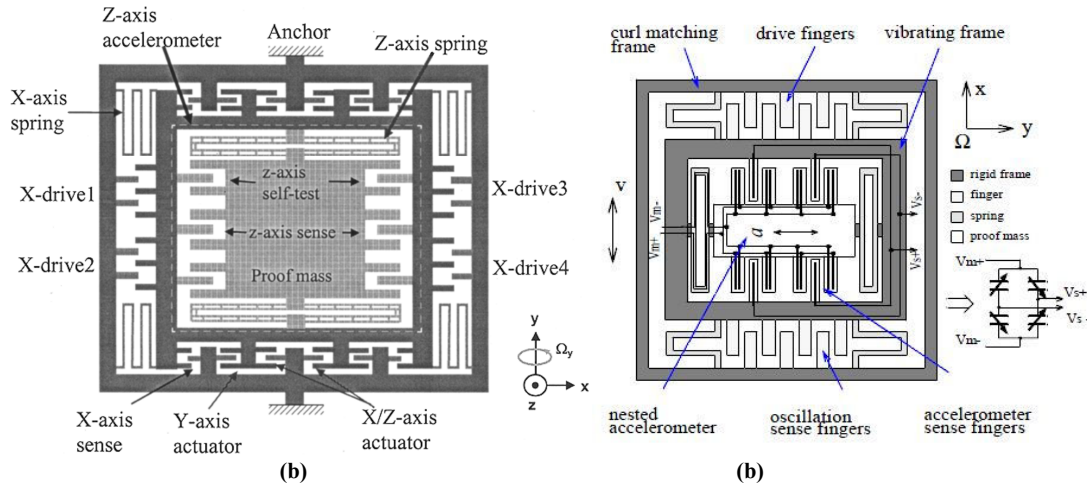


Figure 1-16: a) lateral-axis CMOS MEMS gyroscope [23]. b) z-axis CMOS-MEMS gyroscope [24].

Double rotary lateral-axis rotation sensitive gyroscope proved to have robust decoupling capability [25]. This design was developed as is shown in Fig. 1-17.

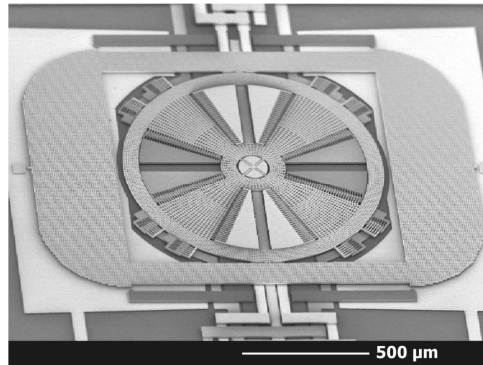


Figure 1-17: Double rotary lateral-axis rotation sensitive gyroscope [25].

The three-folded symmetric gyroscope (3FSG) was reported in literature by [26, 27, 28]. The symmetric design (shown in Fig. 1-18) provides the 3FSG configuration the advantage of perfectly sense and drive mode matching. The latter property enhances the gyroscope sensitivity, especially with the presence of high quality factors.

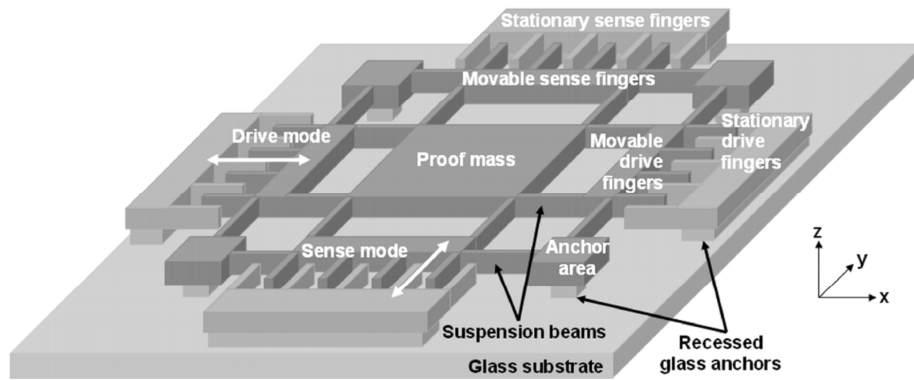


Figure 1-18: 3 folded symmetric decoupled gyroscope [28]

Also, it's worth noting that in the design reported by Akin [28], the drive and sense modes are decoupled by a set of in-plane suspensions that limits both drive and sense modes to have only 1 degree of freedom (1DOF) while keeping the inertial mass with 2DOF as shown in Fig. 1-19. However, the fabrication of architecture required use of Ni electroplating that was molded on glass substrate which is not a standard process. Moreover, he achieved large resonance frequency even with the use of long in-plane suspension beams.

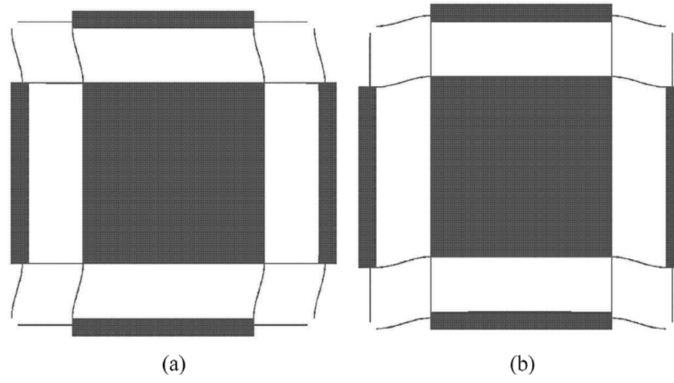


Figure 1-19: a) Drive mode. b) Sense mode [28]

University of California Irvine (UCI) developed in 2005 a gyroscope with a sense mode of multi degree of freedom [29]. The gyroscope sense mode shown in Fig. 1-20-b has two masses and two sets of folded springs.

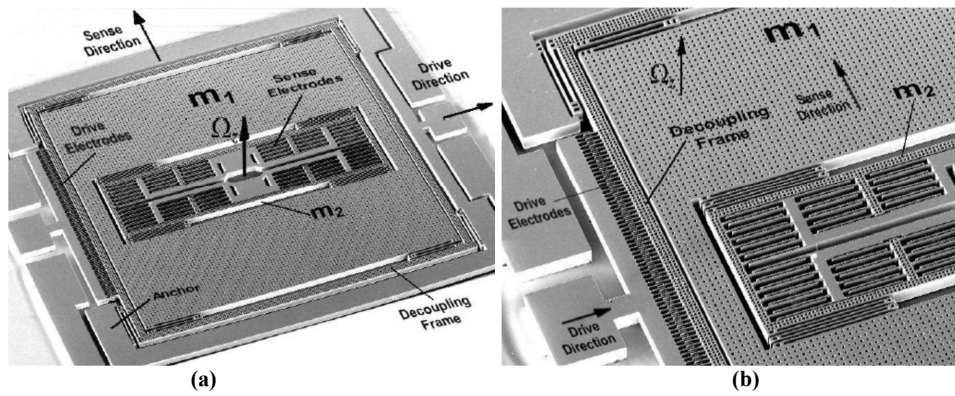
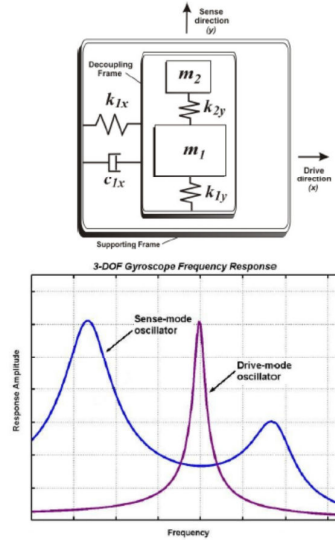


Figure 1-20: a) Micromachined gyroscope. b) 2 degree of freedom sense-mode oscillator [29]

This leads to the presence of two resonance modes as shown in Fig. 1-21. Such effect would lead to increase in the bandwidth of the device, consequently, enhances robustness against environment variations and fabrication imperfections and allows large driving amplitudes. However, this would be on the expense of a relatively small loss in sensitivity.



**Figure 1-21: Lumped mass-spring-damper model and the frequency response of the overall 3-DOF gyroscope with 2-DOF sense-mode [29]**

Fully decoupled MEMS gyroscope was developed by Middle East Technical University, Turkey in 2008 [30]. Although gimbal gyroscopes provide such full decoupling, the architecture shown in Fig. 1-22 is not using the gimbal configuration shown in Fig. 1-14. This configuration has connected both sense electrodes together by rigid trusses and ensures full decoupling. However, this connection, doubles the sense mass and therefore, reduces the Coriolis' response by two.

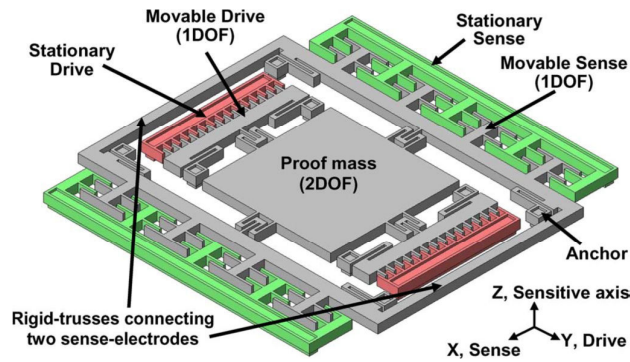


**Figure 1-22: Schematic of fully decoupled MEMS gyroscope [30]**

Symmetric tuning fork architecture with two proof masses was developed by Ayazi et al in Georgia Institute of Technology as shown in Fig. 1-23-a [31-34]. The sense mode of this configuration is taking advantage of the two proof masses so that they actuate in different directions and the output signal is sensed differentially. Therefore, this architecture has the advantage over gimbaled and single proof mass as it's more robust against shock signals.

Because both masses would displace in the same direction, hence, the signal would be rejected in the differential reading. However, he had small sense area and consequently capacitance. Also, the proof-mass area fill factor of his design is less than 17% which reduces the Coriolis' Force and device sensitivity.

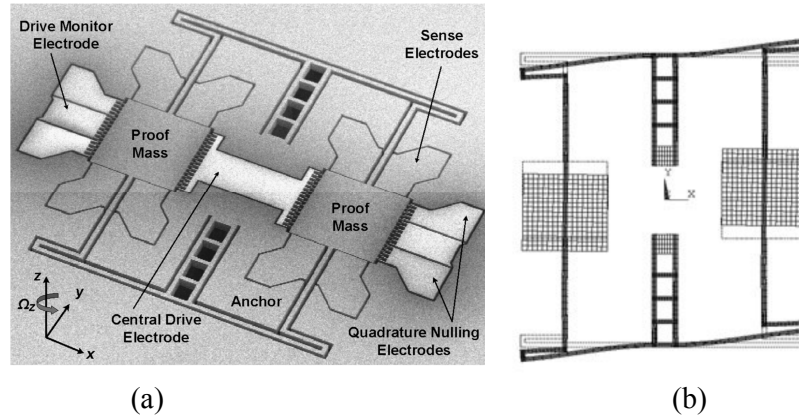


Figure 1-23: a) SEM of the double proof mass tuning fork gyroscope [32]. b) Sense Mode [31].

Ayazi et al introduced in 2010 a novel architecture for a gyroscope that operates at atmospheric pressure with a relatively high quality factor 1000-2000 [35]. The architecture of spoke shape shown in Fig. 1-24 has a resonance frequency of 3 MHz and large dynamic range due to the large  $BW$  with a dynamic range of 30,000°/sec. However, it has low sensitivity of 15.0 $\mu$ V/°/sec.

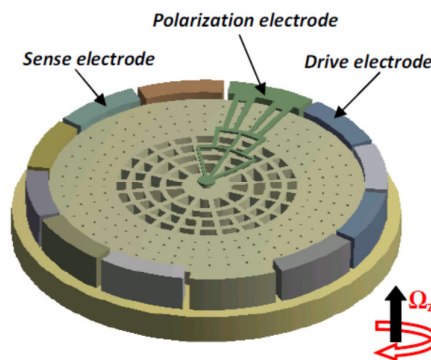


Figure 1-24: Schematic diagram of the capacitive silicon spoke gyroscope [35]

So far, reported micromachined gyroscopes in the literature based on amplitude modulated output signal. In 2012, Shkel et al at UCI reported for the first time a frequency modulation based angular gyroscope [36]. The lumped model shown in the Fig. 1-25, illustrates the working principle of the quasi-digital sensor. The FM based rate sensor eliminated the trade-

off between the quality factor and dynamic range. The authors in [36] reported a quality factor of one million with dynamic range of 2000 deg/sec (limited by the setup) and it's fundamentally limited to 72,000 deg/sec.

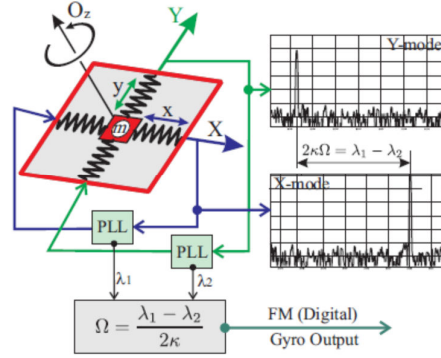


Figure 1-25: Schematic of the quasi-digital gyroscope based on mechanical Frequency Modulation of the input rate [36]

## 1.2. The Need for Novel Architecture

After the thorough inspection of the various designs in literature, it has been found that performance is limited due to the small deflection in case of depending on bending torsional hinges [9-11, 15-17, 19]. Also the designs reported in [15, 37-42] are primarily based on having in-plane suspension or springs which limit the area fill factor of the proof mass. This in turn reduces the proof mass and results in degraded noise floor or minimum detectable angular rate, output signal sensitivity to input angular rate and, accordingly, scale factor. It is worth noting that the various designs that achieve highly-decoupled structures are either 3FSG or gimbale structures.

This evidently means that there is a dire need for entirely novel implementations and fabrication architectures, rather than the common methodologies, which are fairly well-investigated in literature. After the inspection of the basic design equations of gyroscopes equations (1-1) to (1-6), the novel architecture must provide large proof mass and low stiffness, leading to a high quality factor, low support and thermo-elastic losses and reduced resonance frequency. As a result, this allows for relatively high signal sensitivity and suppressed Brownian or thermo-mechanical noise floor. There is another factor that has not been considered in literature, which is the area fill factor of the proof mass or the whole sensor. The inspection of various designs reported in literature reveals that the proof mass area fill factor is no more than 50%, i.e. the use of the overall area needs to be more efficient.

In this thesis, two novel architectures are proposed for the realization of MEMS gyroscope. In these two designs, out-of-plane beams are used instead of in-plane beams for realization of the suspension system. This allows presence of large proof-mass (1.6 mg) with long beams (400-500  $\mu\text{m}$ ) in small area. In chapter two, the architecture of the design is discussed and its performance is modeled and simulated, then compared to literature. Chapter three discusses the fabrication process and micromachining technology used for building the device. It is worth mentioning that the fabrication of both architectures can be performed on a single standard low resistivity Double Side Polished Si wafer without the need for any non-standard and expensive fabrication processes such as wafer bonding or metal assembling as in [13, 18, 25-28]. Then, the characterization setup used for frequency sweep measurement for the fabricated devices is presented. Chapter four studies the different packaging technologies reported in literature and specify the optimum technique for packaging the proposed MEMS gyroscope in this thesis. Finally, chapter five conclude the presented work contribution to the literature, in addition, to standing issues for the future research.



## 2. Chapter II: Novel MEMS Gyroscope Architectures

This thesis studies two different novel architectures for realizing bulk micromachined MEMS gyroscopes. The two architectures are semi-clones of decoupled high performance gyroscope shown in Fig. 2-1 which is considered as one of the best gyroscopes reported in literature [28]. The novelty of both architectures, proposed in this thesis, relies on replacing the in-plane beams used for realizing the suspension system with vertical ones. The realization of out-of-plane beams using standard Microfabrication technologies is patented in [43].

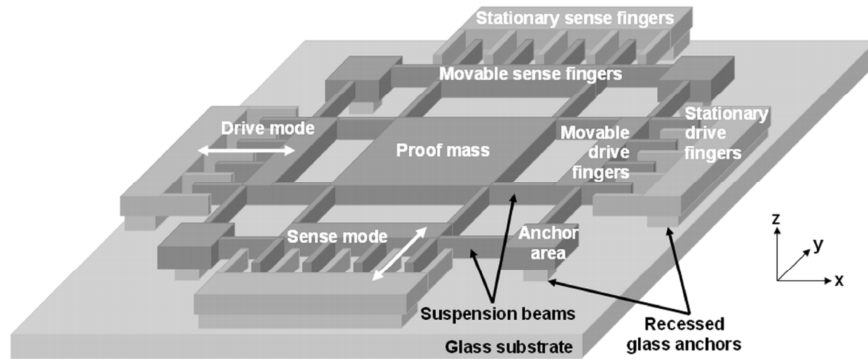


Figure 2-1: 3 folded symmetric decoupled gyroscope [28]

This chapter first presents the architectures. The first one, which has suspension system using, only, vertical beams, hereby and forth called in this thesis vertical suspension gyroscope. As it's shown later, this design has great potential in achieving high performance gyroscope: high quality factor, high drive/sense capacitance, high signal to noise ratio, low resonance frequency, and low noise. However, this architecture has drawbacks, mainly related to the complexity of its fabrication. Consequently, a modification made to the design to ease the fabrication process. This led to the second architecture, hereby and forth called hybrid suspension gyroscope. The hybrid suspension gyroscope, as deduced from its name, is using mix of in-plane and out-of-plane set of beams. Both designs are studied and their performances are compared to each other while their fabrication and packaging processes are presented in later chapters.

Then the electrical and mechanical techniques implemented to decouple the drive/sense mode are introduced. Electrical analysis of the voltage divider scheme used to sense the output signal is provided. After that, it's explained how the proposed architectures ensure mechanical decoupling. This decoupling is simulated using Finite Element Analysis (FEA) software tool (COMSOL Multiphysics).

After that, the spring softening phenomenon is studied, and numerically simulated using Matlab/Simulink platform. This model is used to study the tuning capability of the gyroscopes to match the sense and drive modes resonance frequencies during measurement. The numerical model is first verified by comparing its output results with published comb-drive based MEMS resonator [44]. Then, several results are presented to illustrate the effect of different parameters resonance frequency tuning. Finally, the performance measures of the proposed gyroscopes designs are calculated followed by comparing the performance of both architectures to the state of the art.

## **2.1. Devices Operations**

### **2.1.1. Vertical Suspension Gyroscope Architecture**

The new architecture proposed in this work employs vertical rather than the common in-plane springs or suspensions. This inherently means that the area fill factor of the proof mass should be significantly improved ( $\sim 80\%$ ) which enlarges the proof mass, and consequently reduces the resonance frequency and Brownian noise floor and improves the mechanical quality factor as well as the signal sensitivity and Signal to Noise Ratio (SNR) of the sensor. Moreover, if the fabrication employs bulk micromachining technology, a suspension length up to  $400\text{-}500\mu\text{m}$  is achievable for more than  $700\mu\text{m}$  thick proof masses. This suppresses greatly the thermo-elastic and support losses, which are the dominant sources of losses in high-quality vacuum operated inertial sensors [31].

The new architecture is intended to open the floor for bulk micromachined vibratory MEMS gyroscope (VMG) possessing relatively large sense capacitance ( $>5.5\text{pF}$ ) and proof mass ( $>1.6\text{mg}$ ) which in turn results in relatively large quality factor ( $>100,000$ ) and sensitivity and higher angular rate resolution. As discussed above, in the vertical suspension scheme, the springs can be very long up to  $400\mu\text{m}$  or even longer (certainly without any area loss) depending mainly on the limitation imposed by the maximum standard aspect ratio of Deep Reactive Ion etching (DRIE) processes, which is typically up to 1:50 [45]. Furthermore, there is another inherent advantage in this approach which lies in the fact that the spring length, and accordingly the resonance frequency, is determined by the DRIE time rather than the mask features. This necessarily means that with the same patterning mask, infinite number of resonance frequencies over a wide range can be designed. However, it should be noted that this affects the mode matching and decoupling, so the desired range of dimensions must be

confirmed by simulation prior to etching. Fig. 2-2 demonstrates a 3Folded Symmetric Gyroscope (FSG) employing the proposed vertical suspensions architecture.

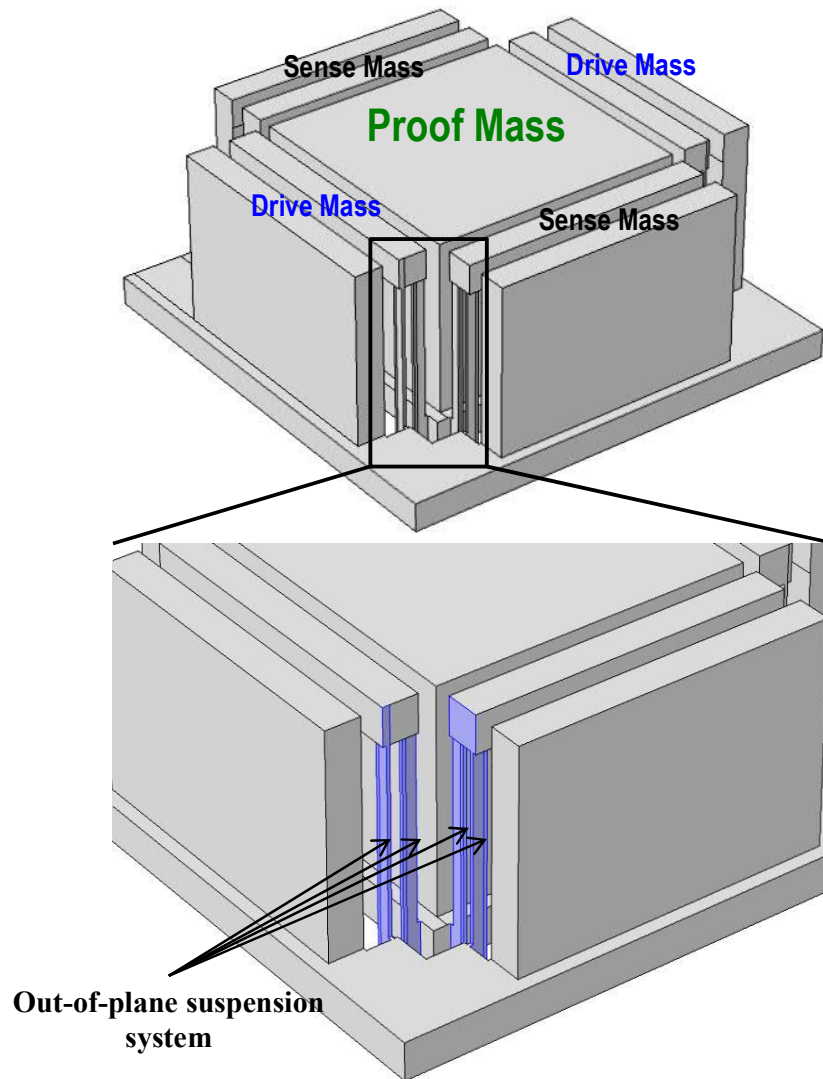


Figure 2-2: 3D structure of the vertical suspension system gyroscope.

Although the fabrication of this design can be done in commercial fabs, using standard processes, it's relatively complex to be made as explained in detail in Chapter 4. Therefore, a simpler version is introduced in the next section.

### 2.1.2. Hybrid Suspension Gyroscope Architecture

In this architecture the outer set of vertical beams are replaced with horizontal ones as shown in Fig 2-3, 2-4). These in-plane beams ensure direct connections between the movable part of the comb-drive and the anchors. Such scheme simplifies the fabrication process flow as illustrated in detail in chapter 4. As shown in Fig. 2-2-b, the movable part of the comb-drive design was modified to accommodate the horizontal beam inside it. This modification create more space that allows the presence of a longer beam, hence, smaller spring constant without reducing the area fill factor of the proof mass or reducing number of fingers (i.e capacitances).

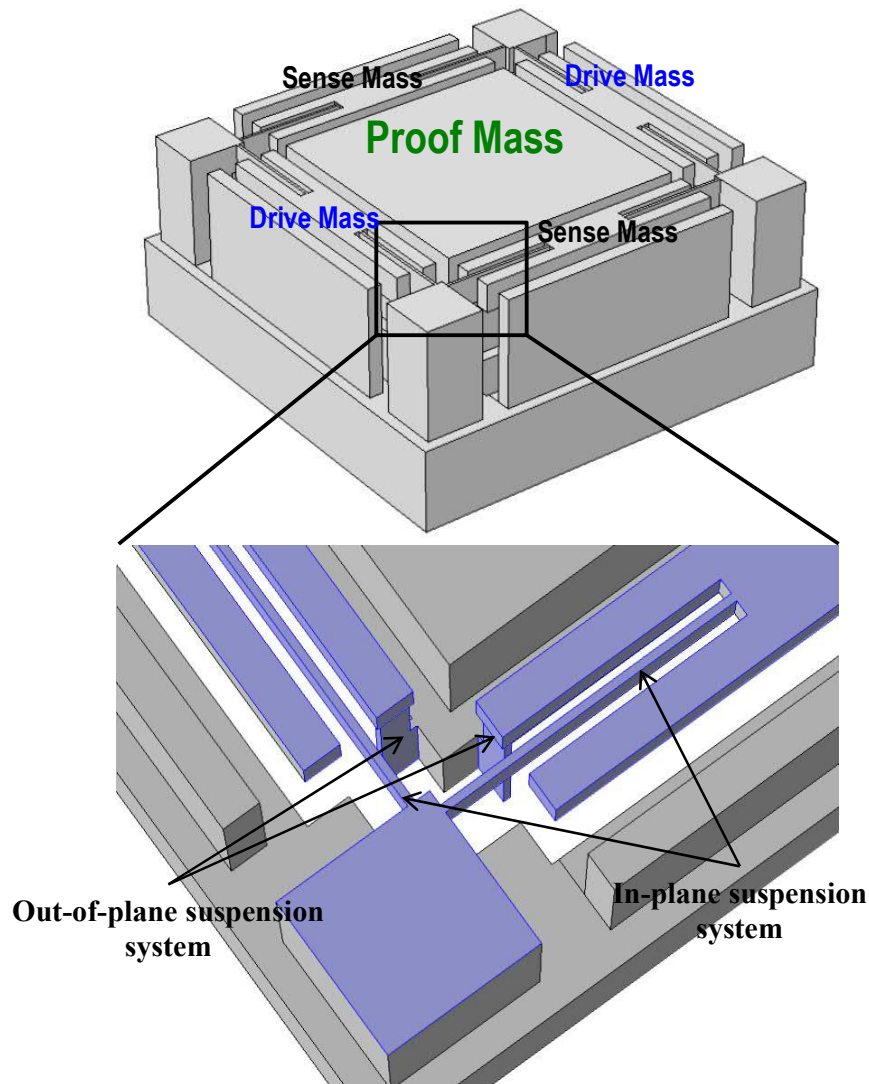
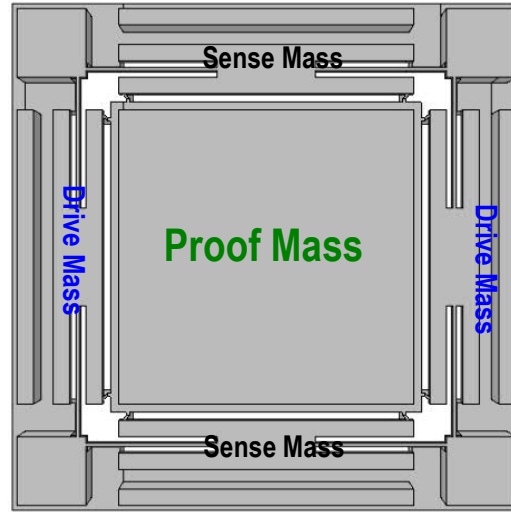
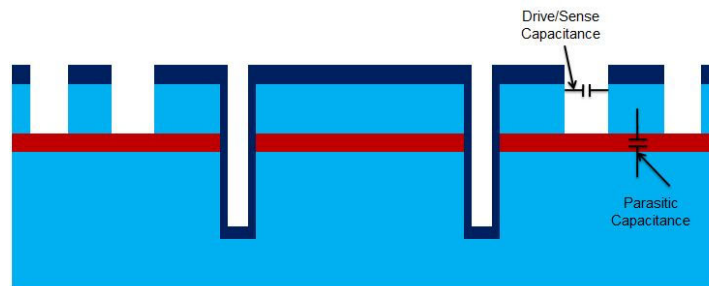


Figure 2-3: 3D structure of the hybrid suspension system gyroscope.



**Figure 2-4: Top view of the hybrid suspension system gyroscope.**

Another great advantage of this architecture over the vertical suspension gyroscope, beside the simplified fabrication process, is the cancellation of the parasitic capacitance. As discussed in detail in Chapter 4, the electrical connections between the anchors and the proof mass is done through the Si bulk below the intermediate  $\text{SiO}_2$  film of the SOI wafer. Therefore, a parasitic capacitance between the comb-drives and the proof mass is generated as shown in Fig 2-5.



**Figure 2-5: Origin of the parasitic capacitance between the drive/sense comb-drive and proof mass in vertical suspension version.**

As shown in the analysis provided in the next section, achieving complete electrical decoupling between the sense and drive modes signals is not possible in the presence of these parasitic capacitances. Due to the use of direct connections (between the proof mass and the anchors) the parasitic capacitances is drastically reduced with the hybrid suspension gyroscope design.

## 2.2. Decoupling Analysis

The coupling problem between the drive and sense mode is one of the biggest issues that must be tackled during designing MEMS gyroscope. The coupling occurs when the movement /displacement in the drive mode cause a displacement in the sense. The drive/sense modes in both designs proposed in this thesis are decoupled by electrical and mechanical means as discussed in the next sections.

### 2.2.1. Electrical Domain

We start the analysis by explaining in detail, with the aid of Fig. 2-6, a conceptual model for gyroscopes (both designs) presented in this thesis. The light green area is the vibrating proof mass, which contains the moving fingers, and the outer dark green area is fixed and holds the fixed combs. The middle moving mass is suspended with a suspension configuration possessing a spring constant  $k$ , and is affected with a damper possessing a damping coefficient  $D$  when actuated electrostatically with a voltage  $V$ . The distances  $x_0$ ,  $l$ ,  $d$ ,  $h$ , and  $w$  represent the initial separating distance between the fixed combs and the proof mass, the static overlap, the distance separating two adjacent fingers, the thickness of the fingers, and the width of the fingers respectively. The capacitances  $C^+$  and  $C^-$  are the varying sense capacitances generated between the fixed and moving parts of the structure due to the input rotation (Coriolis' Force).

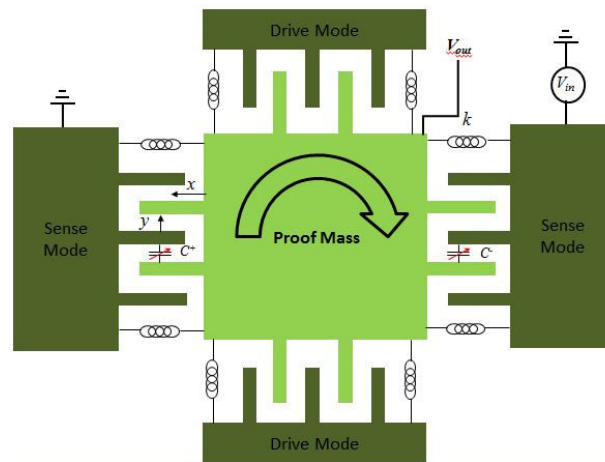
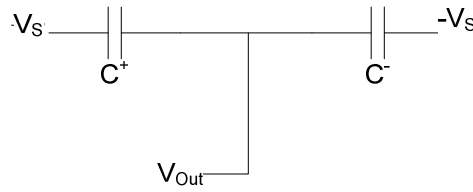


Figure 2-6: A model of the gyroscope showing set of springs with a constant  $k$ , a voltage source, and initial distances; the dark green area is fixed and the light green shaded area is moving;  $C^+$  and  $C^-$  are the sense capacitances generated between the fixed and moving structures of the comb-drive pair. The combs are all  $h$  thick (see text for details).

Assuming complete mechanical coupling, the sense capacitances are affected by the movement  $x$  due to the Coriolis' Force as a result of the input rotation (the displacement desired to be measured). Also, the displacement  $y$  in the perpendicular direction (due to the drive mode oscillation) would affect the value of the capacitance. The latter value is not desired to be measured as it would give a reading on the output signal (change in capacitance value) without input rotation. The dependence of the change of the sense capacitance of the  $y$ -displacement resembles the electrical coupling that is required to be eliminated.

The most famous electrical scheme that achieves electrical decoupling between the drive and sense modes is the voltage divider as shown in Fig. 2-7.



**Figure 2-7: Voltage divider. Most famous scheme for getting rid of the electrical coupling**

The change of the sense capacitances is calculated according to equations (2-1) - (2-4) :

$$C^+ = \frac{\varepsilon_o h(l+x)}{d-y} + \frac{\varepsilon_o h(l+x)}{d+y} = \frac{2\varepsilon_o h(l+x)d}{(d-y)^2} \quad (2-1)$$

While  $\varepsilon_o$  is the permittivity in free space.

$$C^- = \frac{\varepsilon_o h(l-x)}{d-y} + \frac{\varepsilon_o h(l-x)}{d+y} = \frac{2\varepsilon_o h(l-x)d}{(d-y)^2} \quad (2-2)$$

$$V_{Out} = 2V_s \frac{Z_{C^+}}{Z_{C^-} + Z_{C^+}} = 2V_s \frac{\frac{1}{j\omega C^+}}{\frac{1}{j\omega C^+} + \frac{1}{j\omega C^-}} = 2V_s \frac{C^-}{C^- + C^+} = 2V_s \frac{2\varepsilon_o h(l-x)d}{2\varepsilon_o h(l-x)d + 2\varepsilon_o h(l+x)d} \quad (2-3)$$

$$V_{Out} = V_s \frac{l-x}{l} \quad (2-4)$$

It must be noted that in the voltage divider scheme, shown in Fig. 2-7, the output voltage depends only on the displacement  $x$  and is not affected by the displacement  $y$  which comes from the coupling of the other mode. Thus, the voltage divider scheme is providing the

perfect electrical decoupling between the driving and sensing modes. However, this decoupling is limited to the absence of parasitic capacitances between different sense electrode and the proof mass. These parasitic capacitances would be added in parallel with the capacitances of the comb-drive pairs and would not allow the cancellation between the numerator and denominator made in the previous analysis and lead finally to an output voltage depending on the displacement  $y$ .

Also, due to fabrication imperfections such as fingers dimensions might not match for different comb-drives or occurrence of slight misalignment might invalidate the last analysis. This would lead to electrical coupling between the sense and the drive modes. Therefore, it's preferred that the gyroscope design allows full mechanical decoupling as discussed in the next section.

### 2.2.2. Mechanical Domain

As shown in Fig. 2-8-a, the proof mass, drive, and sense modes are sharing the same mass. Hence, complete mechanical coupling is present as all of them have two degree of freedom for movement. Therefore, any displacement in the drive mode (even in the absence of the input rotation and consequently the Coriolis's Force) the sense mode would be affected by the same displacement. Consequently, the gyroscope would have high zero-input bias which means existence of output signal in the absence of input rotation. Fig. 2-8-b is a step on separating the drive mode from the proof mass; however, the sense mode is still coupled to proof mass [28].

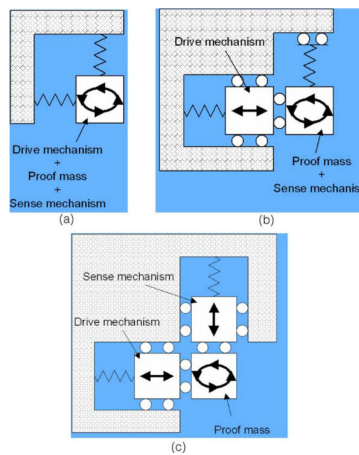


**Figure 2-8: Various decoupling mechanisms to achieve mechanical decoupling. (a) In the “no decoupling” case there is a continuous bias coupled to the sense mode and the drive-mode linearity is disturbed. (b) Decoupled-drive-mode removes the non-linearity but not the sense mode bias. The configuration in (c) completely solves both non-linearity and unwanted sense-mode bias. [28]**



The configuration shown in Fig. 2-8-c achieves complete mechanical decoupling. Where each of the drive and sense modes have its separate mass with one degree of freedom (1 DOF) while the proof mass only has 2DOF. The 2DOF proof mass allows the Coriolis' Force to affect the sense mode while 1 DOF of both the sense and drive modes ensures the decoupling.

Limiting the DOF of the drive/sense mode is done in both architectures by having set of beams that have very high stiffness in y-direction (for drive mode) and low stiffness in x-direction and vice versa for the sense mode.

The mechanical stiffness of the rectangular beam is calculated using equation (2-5) [46]

$$K_{s-linear} = \frac{12EI}{L^3} \quad (2-5)$$

Where  $K_{s-linear}$  is the mechanical spring constant,  $E$  is young's modulus of the material,  $L$  is the suspension length, and  $I$  is the second moment of inertial which is measured according to the following equation with the aid of Fig. 2-9 [46]:

$$I_{xx} = \frac{wt^3}{12}$$

$$I_{yy} = \frac{tw^3}{12}$$

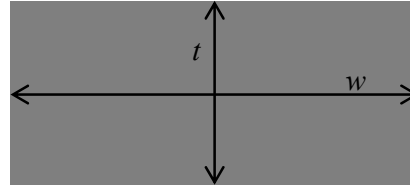
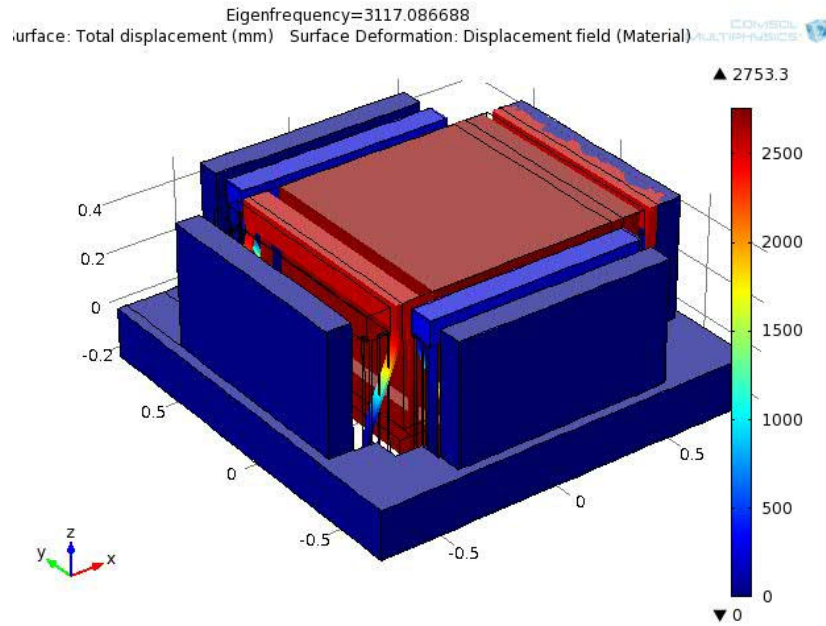


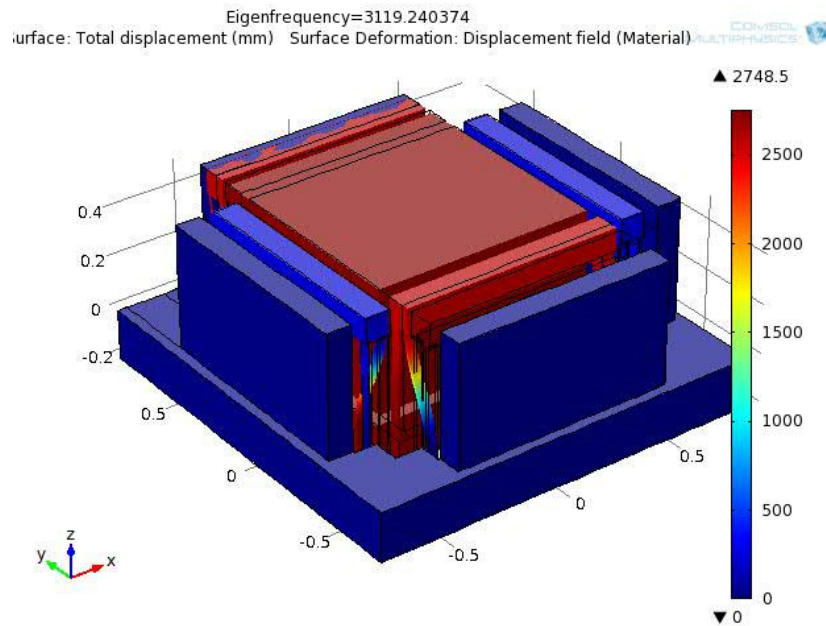
**Figure 2-9: Beam cross-section**

It is clear from the above formula that the aspect ratio of the beam cross-section affects dramatically the ratio between the beam stiffness when it's bent in the x-direction relative to the y-direction. The vertical beams have a cross-section similar to the one shown in Fig. 2-9.

As the aspect ratio of the beams, used in these designs, is set to  $w:t=4:1$ , the ratio between the stiffness in the x-direction to y-direction for the drive mode would be 16:1. Such ratio reduces the mechanical coupling drastically which is confirmed by the Finite Element Analysis (FEA) conducted by COMSOL Multiphysics.



(a)



(b)

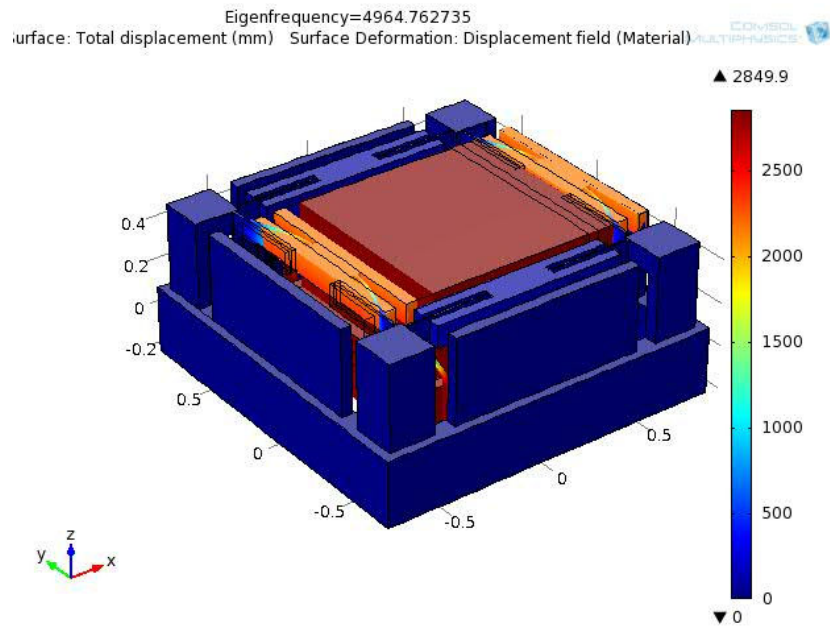
Figure 2-10: a) Drive mode resonance frequency 3117 Hz. b) sense mode resonance frequency 3119 Hz

FEA has been used to analyze the mode shape and verify the decoupling of both gyroscope designs as shown in Fig 2-10. The mechanical coupling is calculated as the percentage of the displacement of the sense comb-drive (in x-direction) relative to the drive displacement (in the x-direction) given that device was excited in the drive mode. Mechanical coupling was calculated to be 6.5%. Table 2-1 gives an overview of the dimensions and properties for the vertical suspension gyroscope.

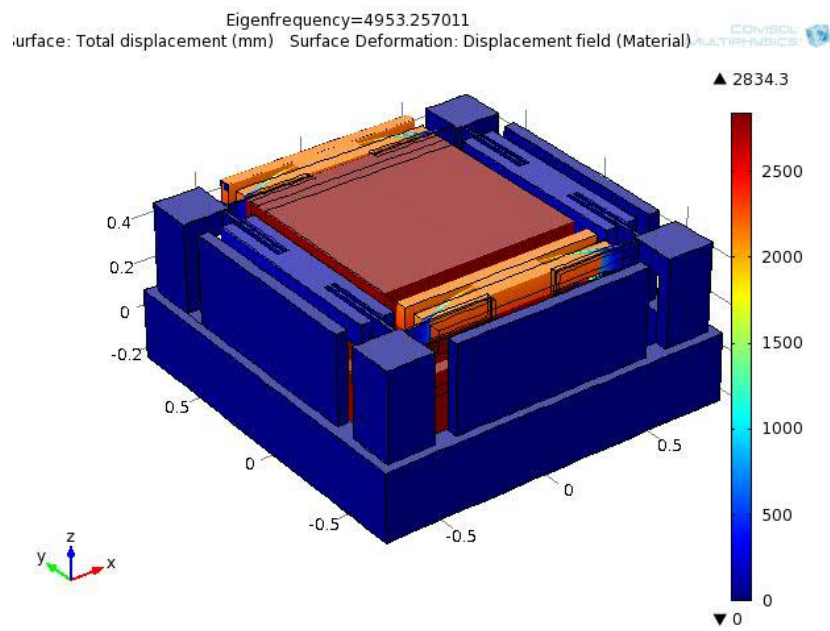
**Table 2-1: Summary of vertical suspension gyroscope dimensions and properties**

| <b>Parameter</b>                         | <b>Value</b>                  |
|--|-------------------------------|
| <i>Proof mass size</i>                   | 1000x1000x700 $\mu\text{m}^3$ |
| <i>Proof mass weight</i>                 | 1.6 mg                        |
| <i>Suspension width/thickness/length</i> | 40x10x400 $\mu\text{m}$       |
| <i>Total device area</i>                 | 2 $\text{mm}^2$               |
| <i>Finger width/thickness</i>            | 2x100 $\mu\text{m}$           |
| <i>Gap between fingers</i>               | 2 $\mu\text{m}$               |
| <i>Fingers overlap</i>                   | 50 $\mu\text{m}$              |
| <i>Number of fingers</i>                 | 250                           |
| <i>Drive/sense electrode capacitance</i> | 5.5 pF                        |
| <i>Parasitic Capacitance</i>             | 0.35 pF                       |
| <i>Proof mass area fill factor</i>       | 80%                           |
| <i>Drive mode frequency</i>              | 3117 Hz                       |
| <i>Sense mode frequency</i>              | 3119 Hz                       |
| <i>Quality Factor</i>                    | 21,000                        |
| <i>Mechanical coupling</i>               | 6.5 %                         |

Fig. 2- 11 shows FEA simulations of the drive and sense modes of the hybrid suspension gyroscope. Mechanical coupling was calculated to be 2.8%. Mechanical coupling for both architectures was calculated when the gyroscope is derived differentially at resonance frequency. Table 2-2 summarizes the dimensions, mechanical and electrical properties of the hybrid suspension gyroscope.



(a)



(b)

Figure 2-11: a) Drive mode resonance frequency 4964 Hz. b) sense mode resonance frequency 4953 Hz

**Table 2-2: Summary of hybrid suspension gyroscope dimensions and properties**

| <b>Parameter</b>                                    | <b>Value</b>                  |
|---|-------------------------------|
| <i>Proof mass dimensions (LxWxh)</i>                | 1000x1000x700 $\mu\text{m}^3$ |
| <i>Proof mass weight</i>                            | 1.6 mg                        |
| <i>Vertical suspension width/thickness/length</i>   | 40x10x300 $\mu\text{m}$       |
| <i>Horizontal suspension width/thickness/length</i> | 100x10x400 $\mu\text{m}$      |
| <i>Total device area</i>                            | 2 $\text{mm}^2$               |
| <i>Finger width/thickness</i>                       | 2x100 $\mu\text{m}$           |
| <i>Gap between fingers</i>                          | 2 $\mu\text{m}$               |
| <i>Fingers overlap</i>                              | 50 $\mu\text{m}$              |
| <i>Number of fingers</i>                            | 250                           |
| <i>Drive/sense electrode capacitance</i>            | 5.5 pF                        |
| <i>Parasitic Capacitance</i>                        | 0.35 fF                       |
| <i>Proof mass area fill factor</i>                  | 80%                           |
| <i>Drive mode frequency</i>                         | 4964 Hz                       |
| <i>Sense mode frequency</i>                         | 4953 Hz                       |
| <i>Quality Factor</i>                               | 21,000                        |
| <i>Mechanical coupling</i>                          | 2.8%                          |

The dimensions used in simulations, listed to in Table 2-1 and Table 2-2, are used selected based on the typical (and standard) photolithography and etching capabilities reported in the literature. This action was taken for the sake of a fair comparison in the performance between the proposed devices in this study with those reported in the literature. However, the fabricated devices had different dimensions which were limited to the capabilities of the microfabrication facilities at AUC.

Also it is worth noting that quality factors calculated assuming vacuum conditions. Therefore, the quality factors value are limited to the support losses. These losses can be reduce b increasing the length of the suspension beams.

### 2.3. Mode Matching

One of the crucial issues in designing gyroscopes is ensuring that both modes have the same resonance frequency. This is essential especially in high quality factor gyroscopes, and small bandwidth. The resonance frequency of the drive mode, in the presence of input rotation, results in oscillating the sense comb-drive with the same frequency (due to the Coriolis' Force). In the case of the drive/sense mode mismatch as seen in Fig. 2-12, a significant reduction to the output the sense signal occurs, hence, worse performance.

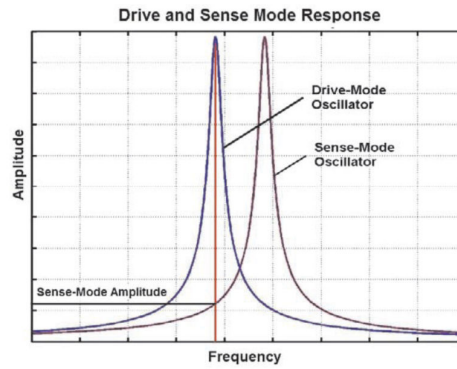


Figure 2-12: Effect of drive and sense modes mismatch on the output signal [1]

Both designs proposed in this thesis are 3FSG which ensures that resonance frequency of the drive and sense modes are the same. The symmetry of the device ensures same geometry for the drive/sense proof mass and suspension. Hence, the resonance frequencies of both modes are matched. However, due to fabrication imperfections, resonance frequency mismatch is inevitable.

A recognized nonlinear phenomenon existing in electrostatically actuated MEMS comb-drives (as those used to drive and sense the proposed designs) is spring softening. In spring softening, the resonance frequency decreases as the amplitude of oscillation increases [46]. This phenomenon is considered advantageous because it can tune the sense frequency to match the drive frequency and results in higher sensitivity [47, 34].

This section presents a comprehensive numerical analysis for the spring softening behavior in MEMS comb-drives that are actuated electrostatically. After deriving an expression for the electrostatic force that takes into account the sliding (longitudinal) and transverse capacitances in the comb-drive (CD). The resulting stiff differential equation is solved numerically using the Runge-Kutta method in Matlab/Simulink environment. After discussing the model it's verified by comparing the results to previously published

experimental data. The solution presented offers an extremely important advantage because it enables the designer to analyze the softening and consequently predicts the required bias DC bias voltage to tune the sense mode resonance frequency for mode matching.

### 2.3.1. Problem Setup for Electrostatic Domain

Before starting the analysis, we provide a conceptual model of an electrostatic CD actuator that can be used for the proposed MEMS gyroscope designs in Fig. 2-13. The gray shaded areas are vibrating and are comprised of the moving fingers and the suspension, while the black shaded areas are fixed and anchored to the supporting substrate. The middle moving mass is suspended with a folded suspension configuration and is actuated with voltages  $V_L$  and  $V_R$  (i.e. left and right). Further, the mass is damped with a damping coefficient  $D$ . In Fig. 2-13,  $x_0$  is the initial spacing between the fixed combs and the proof mass,  $l$  is the rest overlap distance between the fingers,  $d$  is the gap between two adjacent fingers,  $h$  is the thickness of the structure,  $w$  is the width of the fingers,  $W$  is the width of the beam, and  $L$  is the length of the beam. The capacitances  $C_t$  and  $C_l$  are the varying transverse and longitudinal capacitances generated between the fixed and moving parts of the structure, respectively.

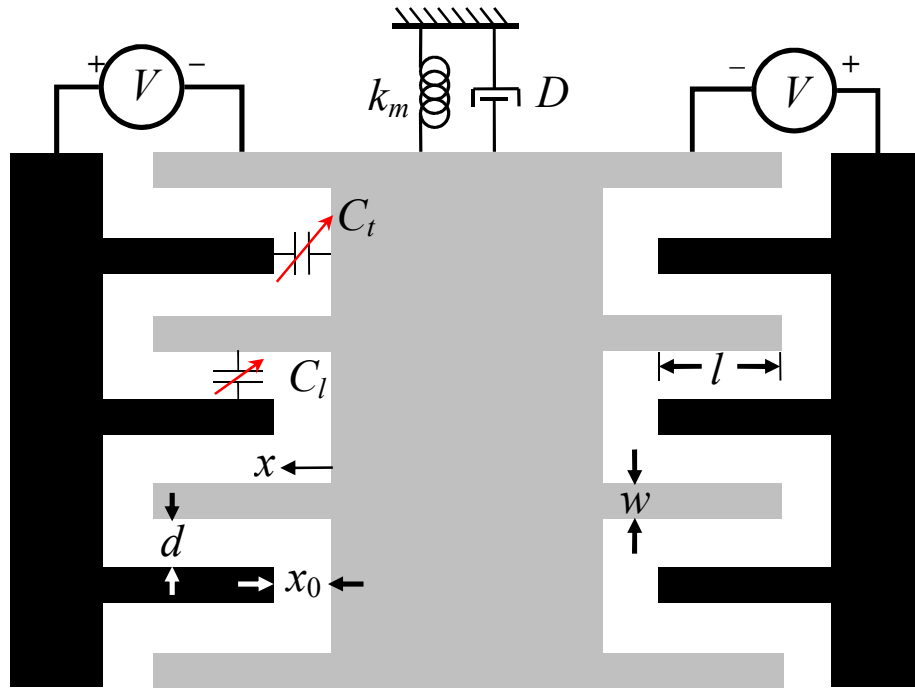


Figure 2-13: A conceptual model of a comb drive actuator showing a damper with damping coefficient  $D$ , a spring with a constant  $k$ , a voltage source (DC and AC), and pertinent distances; the black shaded area is fixed and the gray

shaded area is moving;  $C_t$  is the transverse capacitance generated between the fixed and moving structures, while  $C_l$  is the longitudinal capacitance generated the combs. The combs are all  $h$  thick (see text for details)

### 2.3.1.1. Single Sided Excitation

#### 1) Forces resulting from transverse capacitances

Without loss of generality, we assume that the excitation voltage is applied to the left side of the resonator in Fig. 2-13, i.e.  $V_R = 0$ . The single ended, or single sided, electrostatic force ( $F_{SS}$ ) that will be generated will be the vector sum of the electrostatic forces generated due to the transverse ( $F_t$ ) and longitudinal ( $F_l$ ) capacitances, or  $F_{SS} = |F_t| + |F_l|$ . Because of the symmetrical shape of the structure, the movement is confined theoretically in the  $x$ - direction only. We also use the absolute values because we are interested here in magnitude only.

The electrostatic attractive force is derived from the very well known equation:

$$F_{SS} = -\frac{\partial E_{SS}}{\partial x} \quad (2-6)$$

where  $E_{SS}$  is the electric energy stored in the capacitor, i.e.  $E_{SS} = CV^2/2$ .  $F_t$  is derived ignoring fringing using (2-7) as:

$$F_t = -\frac{N}{2} \frac{\partial}{\partial x} \left( \frac{\epsilon_0 A_t}{x_0 - x} \right) (V_{DC} + V_{AC})^2 = \frac{-\alpha_1}{(x_0 - x)^2} (V_{DC} + V_{AC})^2 \quad (2-7)$$

where

$$\alpha_1 = \frac{N \epsilon_0 A_t}{2} \quad (2-8)$$

Note that  $A_t = h.w$ ,  $N$ , and  $\epsilon_0$  are the transverse area per finger, total number of fingers, and permittivity of free space respectively.

#### 2) Forces resulting from longitudinal capacitances

The expression for  $C_l$  is somewhat more complicated. However, an approximate expression, that incorporates the fringing capacitance, could be used [48].

$$C_l = \epsilon_0 l (N-1) \left\{ \frac{h}{d} + \frac{1}{\pi} \ln \left[ \left( \frac{w}{d} + 1 \right)^2 - 1 \right] \frac{2d}{w} + 1 \right\}^{\left( 1 + \frac{w}{d} \right)} \quad (2-9)$$

Note that in the case of the comb drive,  $h$ ,  $d$ , and  $w$  are constant, and the variation in the capacitance takes place due to the change in  $l$  only. As such,  $F_l$  becomes:



$$F_l = \frac{1}{2} \frac{\partial C_l}{\partial l} (V_{AC} + V_{DC})^2 = \underbrace{-\frac{\epsilon_0(N-1)}{2} \left\{ \frac{h}{d} + \frac{1}{\pi} \ln \left[ \left( \frac{w}{d} + 1 \right)^2 - 1 \right] \left[ \frac{2d}{w} + 1 \right]^{\left( 1 + \frac{w}{d} \right)} \right\}}_{\alpha_2} (V_{DC} + V_{AC})^2 = \alpha_2 (V_{DC} + V_{AC})^2 \quad (2-10)$$

Note that the term  $\alpha_2$  in equation (2-10) is a constant. Using the famous spring-mass oscillation equation of motion with damping, we write:

$$m\ddot{x} + D\dot{x} + k_m x = |F_t| + |F_l| \quad (2-11)$$

where  $m$  denotes mass.

### 2.3.1.2. Double Sided Excitation

The double sided excitation case is more involved, and requires careful setup of the equations because there are attractive forces present at both sides of the structure, working in opposite directions. At first glance, one would be tempted to say that the vibrating mass will not move because both forces are equal in magnitude and opposite in direction. This is true when the voltages applied are DC only. However, when DC and AC voltages are imposed and the AC signal at one side is  $180^\circ$  out of phase with the signal at the other side, one of the attractive forces starts to increase while the other starts to decrease as time progresses. Hence, the mass will vibrate.

To formulate the problem, we assume that the mass will move initially to the left, i.e. the force on the left is larger than that of the right during the first half of the frequency period. The double-sided electrostatic force,  $F_{DS}$ , will once again depend on the forces that result from the transverse and longitudinal capacitances. However, this time we need to account for the left and right combs. In other words,

$$F_{DS} = F_t^T + F_l^T \quad (2-12)$$

In which,

$$F_t^T = |F_t^L - F_t^R| \quad (2-13)$$

$$F_l^T = |F_l^L - F_l^R| \quad (2-14)$$

In equations (2-12) to (2-14),  $F_t^T$  is the total resultant transverse electrostatic force generated at both sides (left:  $F_t^L$  and right:  $F_t^R$ ) due to the transverse capacitances, and  $F_l^T$  is the total resultant longitudinal electrostatic force generated at both sides (left:  $F_l^L$ , and right:

$F_l^R$ ) due to the longitudinal capacitances. Note that we need to subtract the forces in equations (2-13) and (2-14) because both forces on the left and right hand side are attractive, and hence they are acting in opposite directions.

1) *Forces resulting from transverse capacitances*

As mentioned earlier, the electrostatic forces generated at both ends of the structure are attractive forces. However, the magnitude at one end will be larger than the other end and thus the structure will move. Assuming that the structure starts moving to the left hand side, then:

$$F_l^L = \frac{-\alpha_1}{(x_0 - x)^2} (V_{DC} + V_{AC})^2 \quad (2-15)$$

$$F_l^R = \frac{-\alpha_1}{(x_0 + x)^2} (V_{DC} - V_{AC})^2 \quad (2-16)$$

Substituting (2-15) and (2-16) into (2-13), and after some manipulation, yields

$$F_l^T = 2N\epsilon A_l \left( \frac{V_{DC}^2 x_0 x + V_{AC}^2 x_0 x + V_{DC} V_{AC} x^2 + V_{DC} V_{AC} x_0^2}{(x_0^2 - x^2)^2} \right) \quad (2-17)$$

2) *Forces resulting from longitudinal capacitances*

Using the same methodology used in the previous subsection,  $F_l^T$  can be calculated using (2-10) as

$$F_l^L = \alpha_2 (V_{DC} + V_{AC})^2 \quad (2-18)$$

$$F_l^R = \alpha_2 (V_{DC} - V_{AC})^2 \quad (2-19)$$

Note the difference in signs at  $V_{AC}$ , which represents that they are 180 degrees out of phase. Once again, substituting equations (2-18) and (2-19) into equation (2-14), yields

$$F_l^T = 4\alpha_2 V_{DC} V_{AC} \quad (2-20)$$

Finally, the damped harmonic equation for this case can be written as

$$m\ddot{x} + D\dot{x} + k_m x = F_{DS} \quad (2-21)$$

## 2.3.2. Numerical Analysis

### 2.3.2.1. Matlab and Simulink Usage and Solution Methodology

In order to solve the equations derived above, Matlab and Simulink were both utilized to determine the oscillation behavior numerically.

The inputs to Matlab, i.e. the dimensions and parameters of the comb-drive, are coupled to the Simulink model, which solves the equation of motion after modeling the electrostatic forces. Multiple calculations are performed in the Matlab code to deduce the Simulink parameters, and finally the solution from Simulink is carried to the code.

Tracking the resonance frequency of the given resonator at different cases (different input voltages, or CD dimensions) was performed using a loop in the Matlab code, which interacts with Simulink. After a reasonable time of simulation has elapsed or, in other words, when the system reaches steady state (by inspection), we extract the maximum displacement from the Simulink model at each step, feed it back to Matlab, and graph frequency versus displacement. By repeating this solution, several frequency responses are obtained and drawn on the same plot to obtain the *new*, effective, resonance frequency of the resonator at the conditions dictated. Fig. 2-14 summarizes this methodology.

As will be shown, the direction of the frequency sweep, whether sweep up or sweep down, affects the response significantly. In order to account for this phenomenon, the input voltage phase of each run must be transferred while sweeping (whether up or down) the frequencies.

A behavioral model for the famous mass-spring-damper system was built previously in [28] using Simulink in an effort to model the performance of a MEMS gyroscope. However, this model did not take into consideration the softening due to the electrostatic actuation. To the best of our knowledge, this is the first demonstration of analyzing the sweep up and sweep down numerically.

With this methodology in mind, the Simulink model, as shown in Fig. 2-15, was created. Fig. 2-15a models the spring-damper equation by a closed loop consisting of two integrators, while Fig. 2-15b & Fig. 2-15c models the electrostatic forces. Note that in the single ended excitation case, the force that is generated from one of the comb drives must be eliminated. Therefore, the input signal labeled  $V_-$  should be multiplied by a factor of zero to cancel its effect.

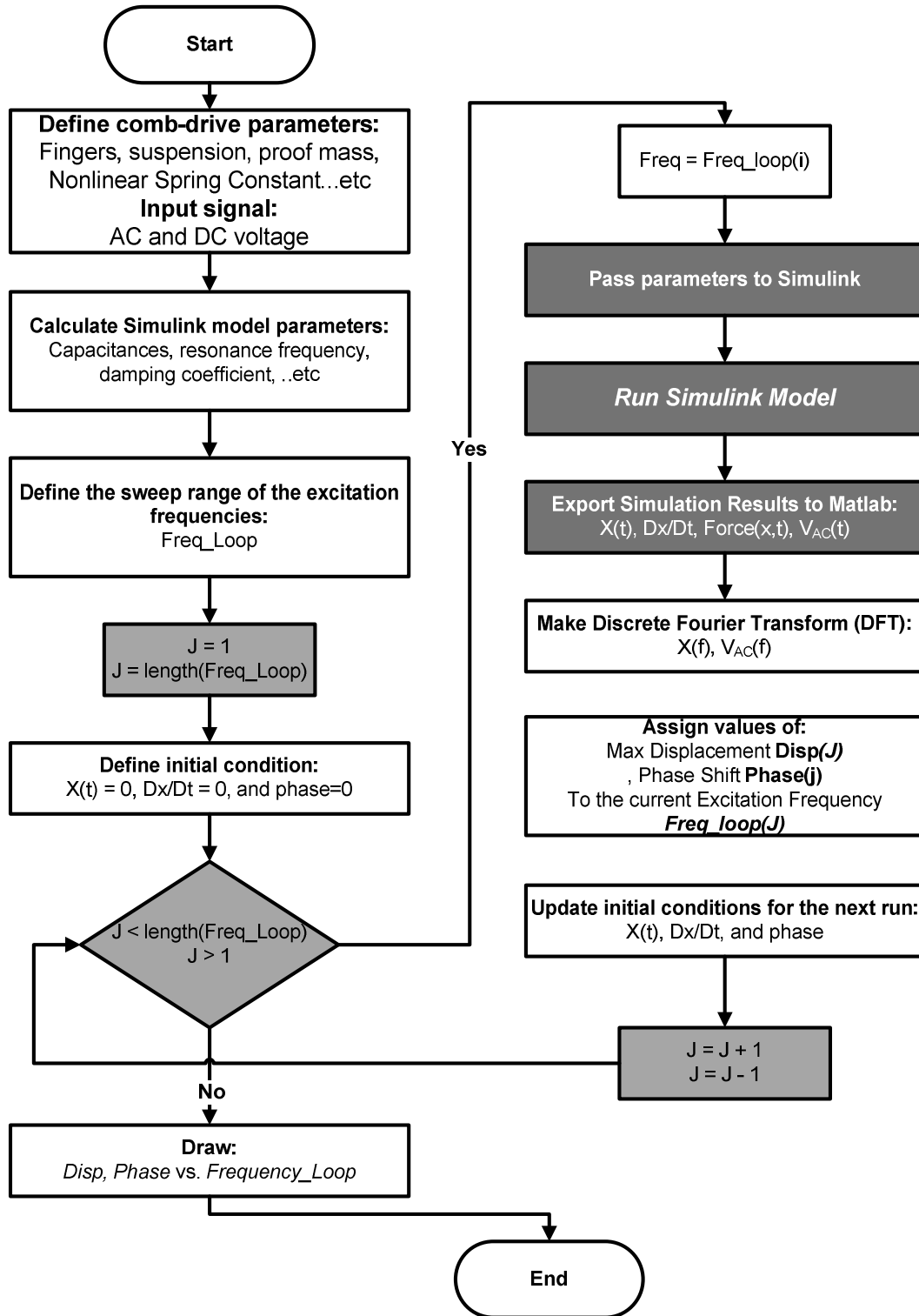


Figure 2-14: Solution methodology (dark gray blocks represent the Simulink Domain; white and light gray blocks represent Matlab Domain). The first lines written in light gray boxes are responsible for the sweep up, while the second lines written are responsible for the sweep down.

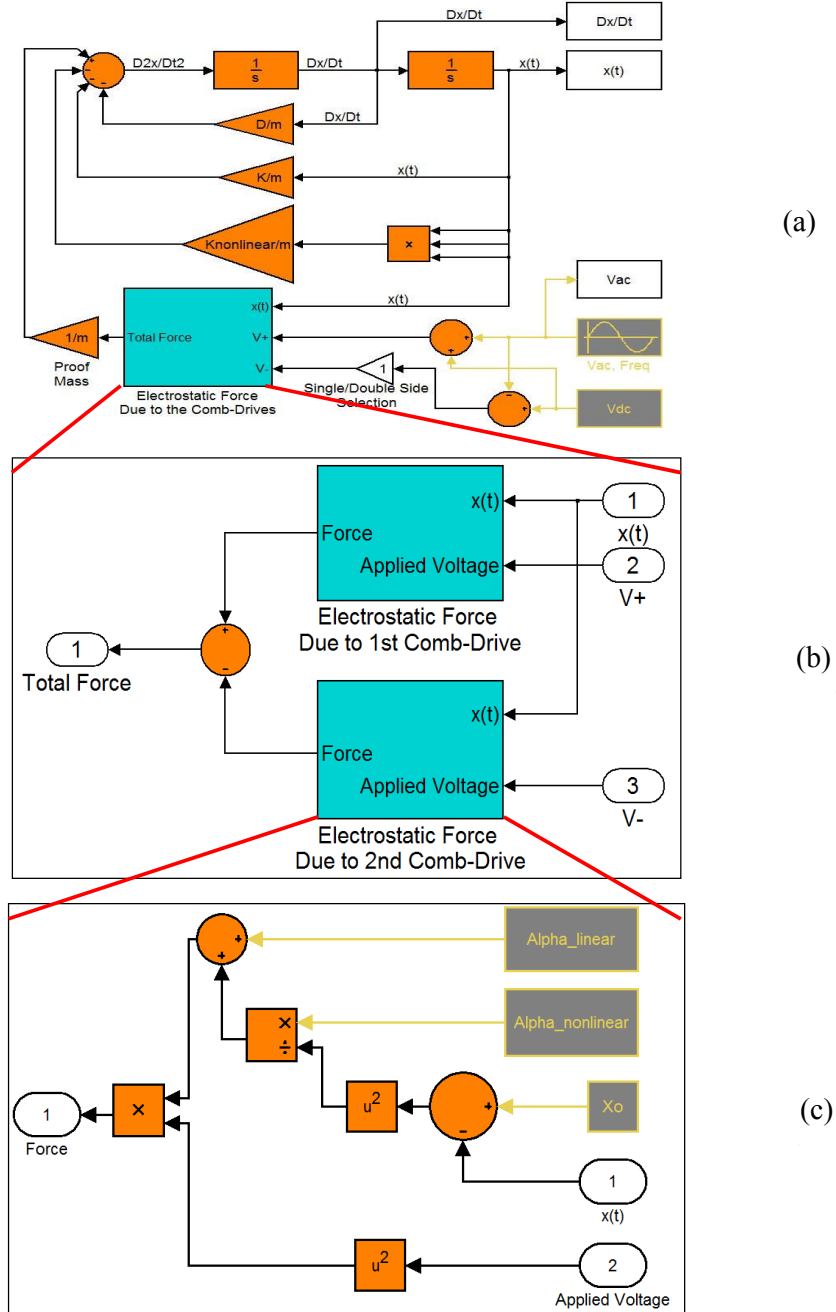


Figure 2-15: The spring-damper equation, (b) the electrostatic force, and (c) the electrostatic force

To solve differential equations, numerical methods usually take the following general form,

New value = old value + (slope  $\times$  step size). In mathematical form:

$$y_{i+1} = y_i + \phi(x_i, y_i)h \quad (2-22)$$

where  $\phi$  is the slope and  $h$  is the step size. The difference in numerical methods then arises in the manner in which the slope is estimated [49]. Many numerical methods are available and

each is used for a specific application. The method of choice here was the Runge-Kutta (RK) method [49].

The RK method was chosen to solve the problem herein because: (1) the RK method achieves the accuracy of a Taylor series approach without requiring the calculation of higher derivatives, (2) the slope in RK methods is dependent not only on the previous  $x$  and  $y$  values, but is also a function of the step size  $h$ , and (3) RK methods offers, in addition to a possible variation in the step size, a variation in the slope function. Note that the slope in the RK method is referred to as the increment function and hence equation (2-22) for RK methods can be rewritten as

$$y_{i+1} = y_i + \phi(x_i, y_i, h)h \quad (2-23)$$

where

$$\phi = a_1c_1 + a_2c_2 + \dots + a_nc_n \quad (2-24)$$

in which  $a_1, a_2, \dots, a_n$  are constants and  $c$ 's are functions that represent slopes, and both  $a$  and  $c$  are deduced using appropriate tables [49].

### 2.3.3. Model Verification (Case Study)

The ultimate verification of the numerical analysis is to compare the results attained with measured data. In this study, the numerical model is verified with a MEMS resonator driven using electrostatic force through comb-drive. As the model is only verifying the mass-spring-damping system of a pair of comb-drive (one mode of the gyroscope, either drive or sense) then it's acceptable to verify the model with a MEMS resonator instead of gyroscope. With respect to MEMS resonators, perhaps the resonator that has received the widest acclaim in the literature was the one presented by Nguyen and Howe while at the University of California at Berkeley [44]. In that seminal paper, Nguyen and Howe present only measured results of the spring softening without presenting sufficient theoretical analysis or numerical simulations. The measurement of concern was performed in [44] by varying the DC voltage from 10 V to 22 V in steps of 1 V.

We can infer from results that the resonance frequency reduces as the DC voltage increases even if the amplitude of oscillation were to be very small.

Although the resonance frequency of the resonator presented in [44] decreases as  $V_{DC}$  voltage increases for small amplitudes of oscillation, the device still experiences hardening but is not dominant for the specific excitation conditions. Fig. 2-16 shows the comparison between the proposed theoretical technique and the measurement results provided in [44]. Although the

parameters used to obtain the plot in Fig. 2-16 are available in [44], we include them here nonetheless in Table 2-3 for convenience. Fig. 2-16 was obtained using the numerical model and ignoring the hardening component because softening is dominant in this case at small oscillation amplitudes.

**Table 2-3: Parameters used to obtain the plots in Figs. 2-16 and 2-17.**

| Parameter                                   | Value                     |
|---|---------------------------|
| <i>Spring Constant, <math>k_m</math></i>    | 0.65 N/m                  |
| <i>Mass, <math>m</math></i>                 | $5.73 \times 10^{-11}$ kg |
| <i>Quality factor, <math>Q</math></i>       | 23'400                    |
| <i>Beam length, <math>L</math></i>          | 185.3 $\mu\text{m}$       |
| <i>Beam width, <math>W</math></i>           | 1.9 $\mu\text{m}$         |
| <i>Initial overlap, <math>l</math></i>      | 20 $\mu\text{m}$          |
| <i>Finger spacing, <math>d</math></i>       | 2 $\mu\text{m}$           |
| <i>Structural thickness, <math>h</math></i> | 2 $\mu\text{m}$           |
| <i>Finger width, <math>w</math></i>         | 2 $\mu\text{m}$           |
| <i>Initial rotor and stator separation</i>  | 16 $\mu\text{m}$          |
| <i>Young's Modulus, <math>E</math></i>      | 150 GPa                   |

Note how both results agree very well with each other in terms of the *shift in resonant frequency*. However, there is a deviation from the theoretical resonance frequency: the measured resonant frequency was in the range of 18,700 Hz while the theoretical resonant frequency is 16,950 Hz. Given that the resonant frequency  $f_r$  is calculated using  $(k_m/m)^{0.5}$ , this 10% deviation between theory and measurements is typical in MEMS and is expected here considering the well-known tolerance in the Young's Modulus (used to calculate  $k$ ), the tolerance in the density of polysilicon after deposition (used to calculate  $m$ ) [50], and the approximations used when calculating the spring constants of the cantilever beams which act as suspensions.

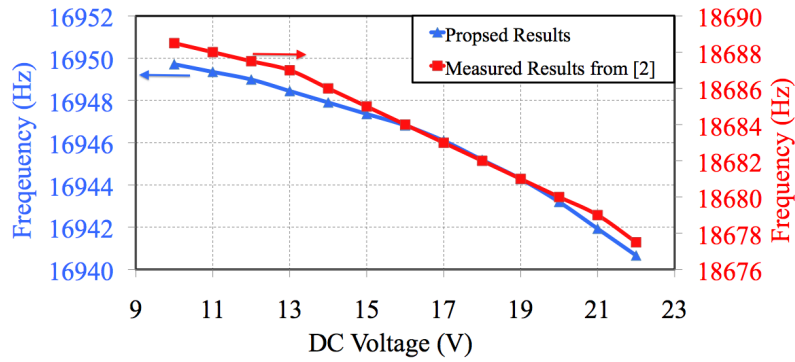


Figure 2-16: Comparing the proposed solution with the measured results from Nguyen and Howe in [44]. Graph taken from [52].

In case of increasing the input voltage achieving higher displacements, spring hardening effect dominates the shift in resonance frequency. In spring hardening case, the resonance frequency increases. Nguyen and Howe [44] experienced a hardening response in the measurements of large displacement amplitudes; explicitly, they found three steady state amplitudes for a specific excitation frequency and described this behavior as erratic.

Fig. 2-17 provides the behavior of the resonator after applying the same conditions mentioned in [44] and Fig. 2-18 shows the measured results in [44]. Note how both results agree very well with each other once again in terms of frequency shift. Fig. 2-17 provides the information for displacement in the y- axis, while the measurement of Nguyen and Howe [44] provides the current information; the output current however, is proportional to the displacement. As mentioned earlier in the softening case, the magnitudes of the frequency shift in both figures agree very well with each other. The discrepancy in the resonant frequency itself is attributed for the reasons just mentioned in the softening case.

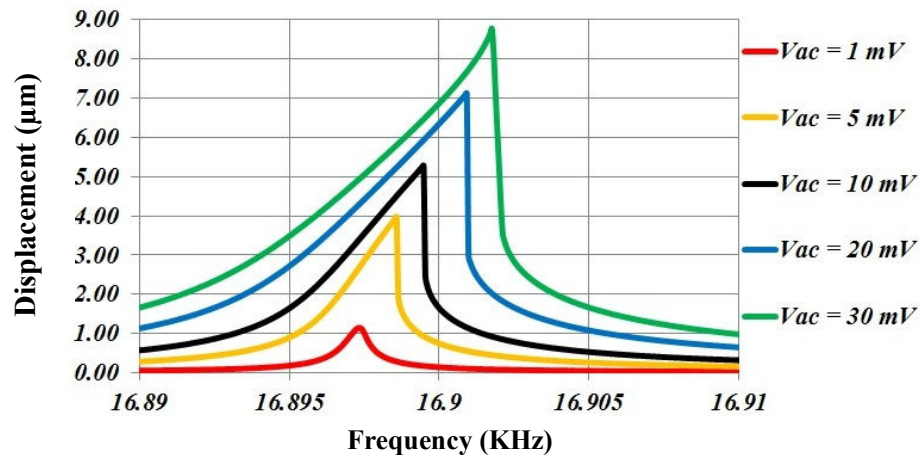


Figure 2-17: The hardening response of the resonator in [44] obtained by using the proposed analysis. Graph taken from [51]



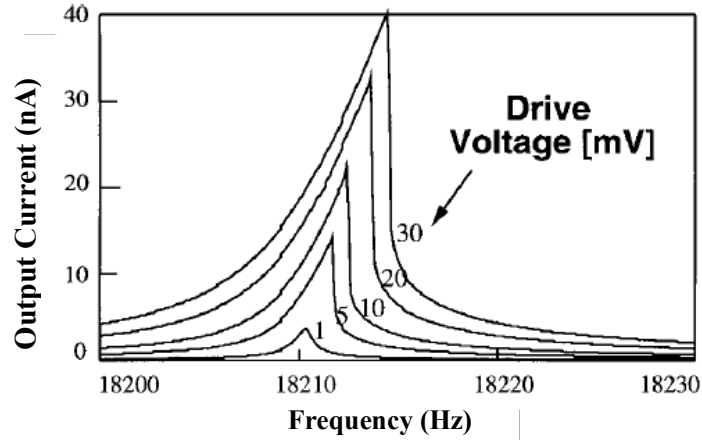


Figure 2-18: The measurement results of the output current of the resonator as presented in [44]. Note the similarities between that the measurements in this figure and the theoretical results shown in Fig. 2-17 above

Finally, it is worth mentioning that there are other sources that can introduce nonlinearity and affect the response of the device like levitation forces [52] and end effects [53] but are beyond the scope of this work.

#### 2.3.4. Results

The purpose of this section is to understand the effects of various parameters on the resonant frequency shift in comb drive structures to adjust these parameters properly for suitable frequency matching capability. Hence, a variety of typical combinations were solved for, vertical and hybrid suspension systems, double sided excitation while varying several affecting parameters. In order to account for the physical properties of the device, the solution was attained for various values of  $V_{AC}$ ,  $V_{DC}$ , and  $x_0$ . The solutions were acquired by changing one parameter at a time. When the solution is acquired, the amplitude of the displacement,  $x$ , is plotted versus frequency to detect the *new* resonant frequency. The parameter values used for, both, vertical and hybrid suspension gyroscopes are listed in Table 2-4.

It's worth noting that the spring softening is simulated solely in this section as the maximum displacement achieved is limited to less than 4  $\mu\text{m}$  ( $< 10\%$  of beam length), therefore, hardening effects can be neglected [51].

Table 2-4: Parameters values used for simulating both architectures.

| Figure                  | Varying Parameter   | Constant Parameters           |
|-------------------------|---|-------------------------------|
| Fig. 2-19<br>(Vertical) | $V_{DC} = \begin{cases} 10\text{ V} \\ 20\text{ V} \\ 30\text{ V} \\ 40\text{ V} \\ 50\text{ V} \end{cases}$                      | $V_{AC} = 5\text{ mV}$        |
| Fig. 2-22<br>(Hybrid)   |   | $Q = 21,000$                  |
|                         |   | $x_0 = 10\text{ }\mu\text{m}$ |
|                         |   |                               |
| Fig. 2-20<br>(Vertical) | $V_{AC} = \begin{cases} 1\text{ mV} \\ 10\text{ mV} \\ 20\text{ mV} \\ 30\text{ mV} \\ 40\text{ mV} \end{cases}$                  | $V_{DC} = 10\text{ V}$        |
| Fig. 2-23<br>(Hybrid)   |   | $Q = 21,000$                  |
|                         |   | $x_0 = 10\text{ }\mu\text{m}$ |
|                         |   |                               |
| Fig. 2-21<br>(Vertical) | $x_0 = \begin{cases} 5\text{ }\mu\text{m} \\ 10\text{ }\mu\text{m} \\ 15\text{ }\mu\text{m} \\ 20\text{ }\mu\text{m} \end{cases}$ | $V_{DC} = 10\text{ V}$        |
| Fig. 2-24<br>(Hybrid)   |   | $V_{AC} = 5\text{ mV}$        |
|                         |   | $Q = 21,000$                  |
|                         |   |                               |

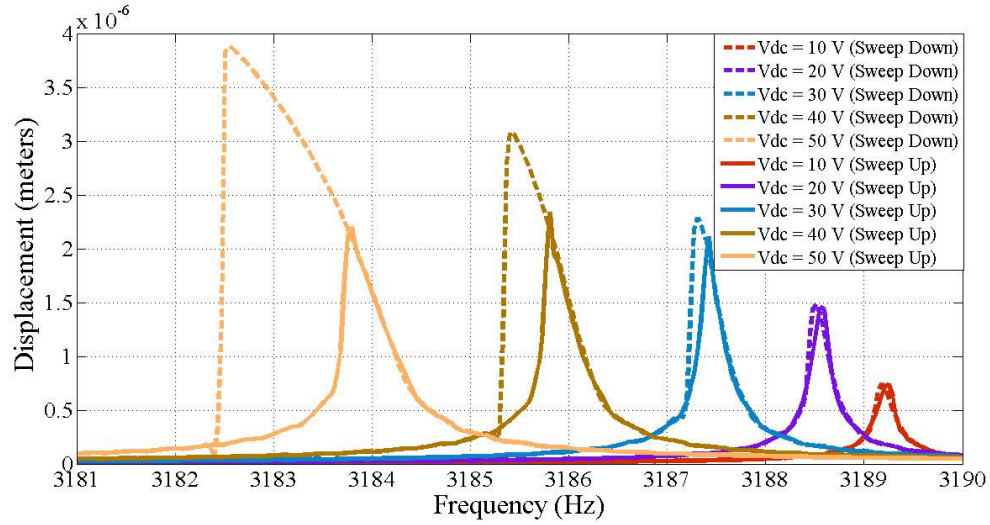


Figure 2-19: The double-sided response for various DC excitation voltages applied to the vertical suspension gyroscope

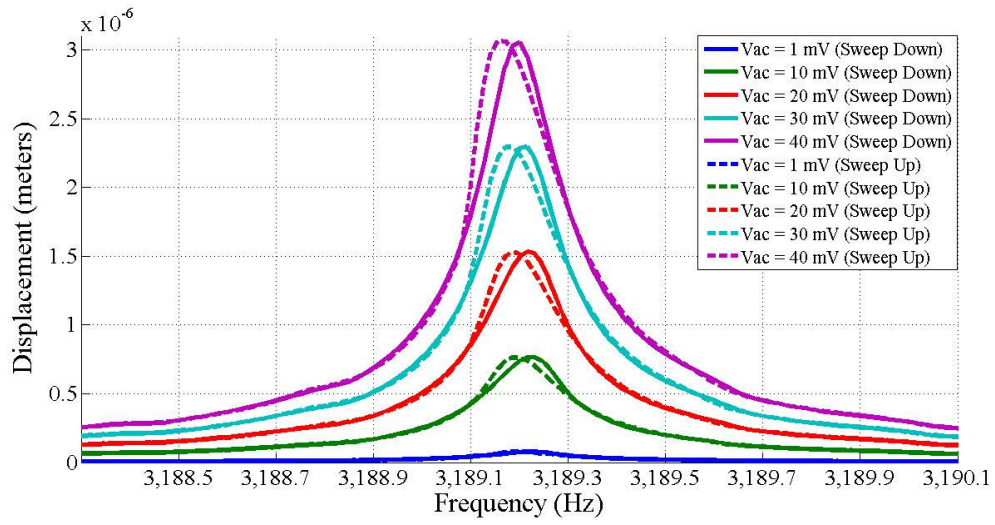


Figure 2-20: The double-sided response for various AC excitation voltages applied to the vertical suspension gyroscope

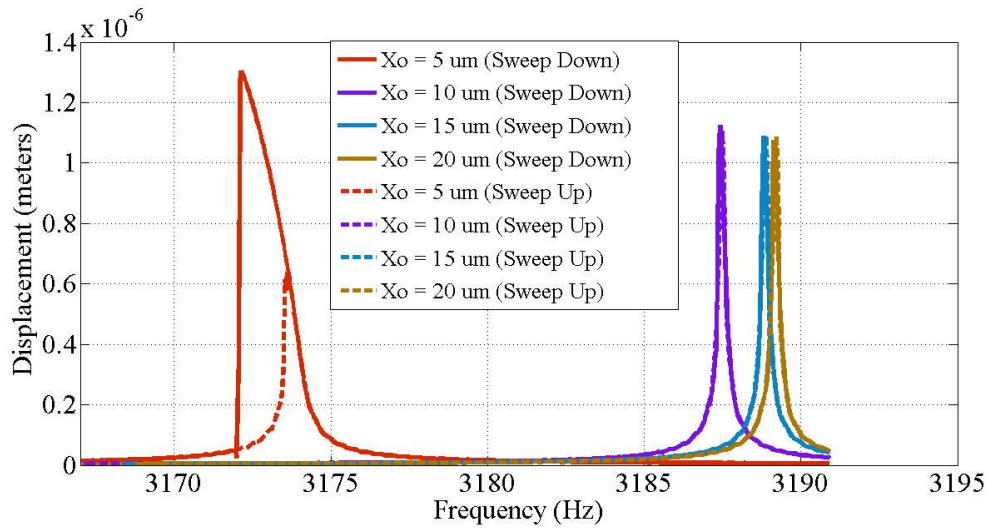


Figure 2-21: The double-sided response for various  $X_0$  values for the vertical suspension gyroscope

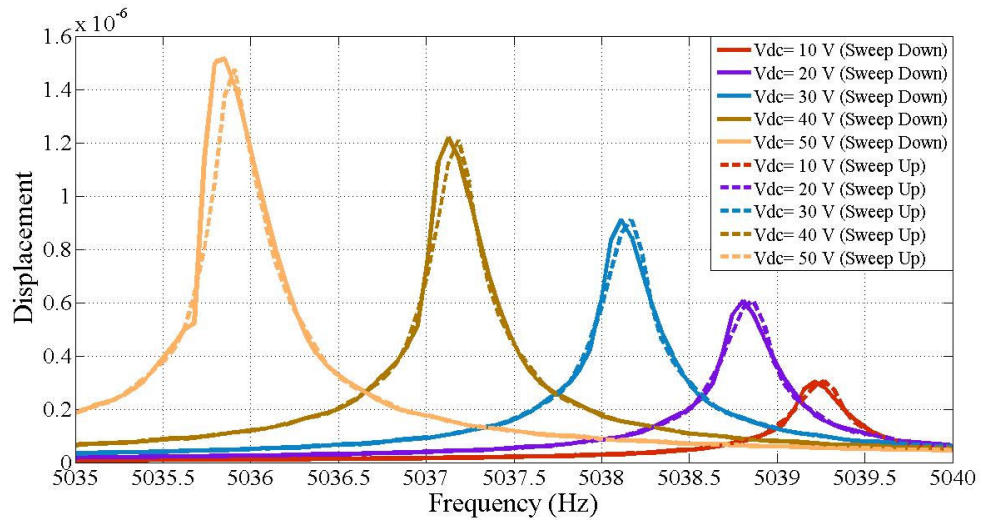


Figure 2-22: The double-sided response for various DC excitation voltages applied to the hybrid suspension gyroscope

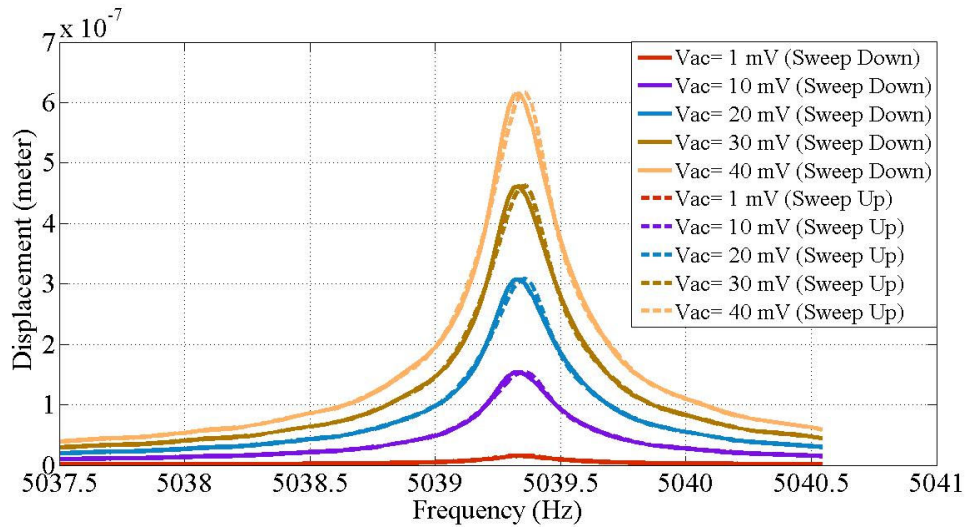


Figure 2-23: The double-sided response for various AC excitation voltages applied to the hybrid suspension gyroscope

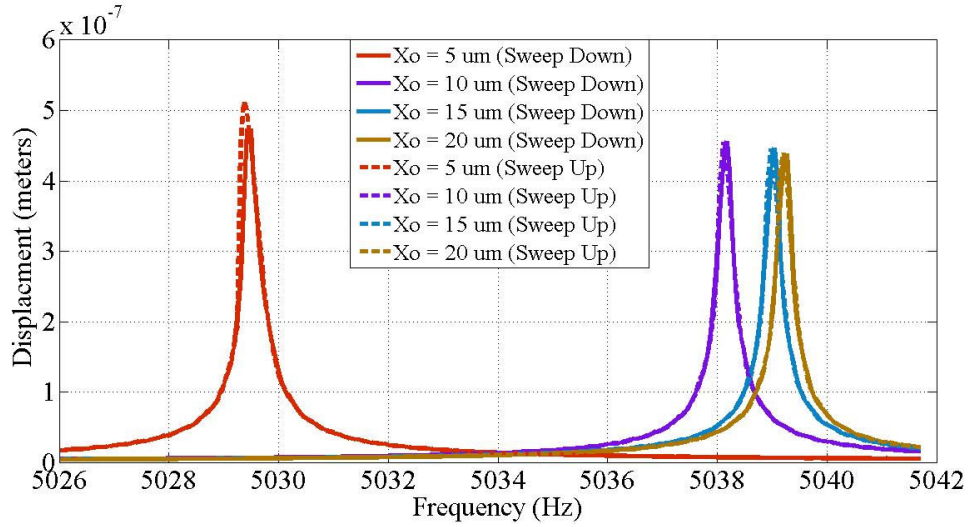


Figure 2-24: The double-sided response for various  $X_0$  values for the hybrid suspension gyroscope

The softening effect becomes dominant when both the DC voltages become relatively high as shown in Fig. 2-19 and Fig. 2-22 for the vertical and hybrid suspension respectively. In Fig. 2-21 and Fig. 2-24 (for vertical and hybrid suspension respectively) the separation distance between the stator and rotor decreases, an evident softening behavior is witnessed. Again, this was expected because the electrostatic force varies nonlinearly with displacement. Generally, all the results acquired are indeed sensible. However, the change in applied AC voltage only increases (shown in Fig. 2-20 and Fig. 2-23) the displacement amplitude without affecting the resonance frequency significantly. Because the typical values of the AC voltages are at least three orders of magnitude smaller than the DC polarization voltage.

The effect of the stiffer beams used in the hybrid suspension gyroscope can be inferred from the lower displacements shown in Fig. 2-23 compared to the vertical suspension gyroscope in Fig. 2-20. However, this effect can be compensated by using higher AC voltages given that the max voltage that can be used is 2.5 volt while the max volt simulated is 40 mV.

Also, the stiffer beams of the hybrid suspension gyroscope need larger DC voltages for resonance frequency tuning as shown in Fig. 2-22. However, this increase in the DC voltage is limited to the electronic circuits, used for driving the gyroscope, which is 50 volt. This problem can be solved by reducing the initial stator to rotor spacing from 10  $\mu\text{m}$  to 7  $\mu\text{m}$ . Fig. 2-25 shows a tuning range, for the hybrid suspension gyroscope of 10 Hz, more than that of the vertical suspension architecture.

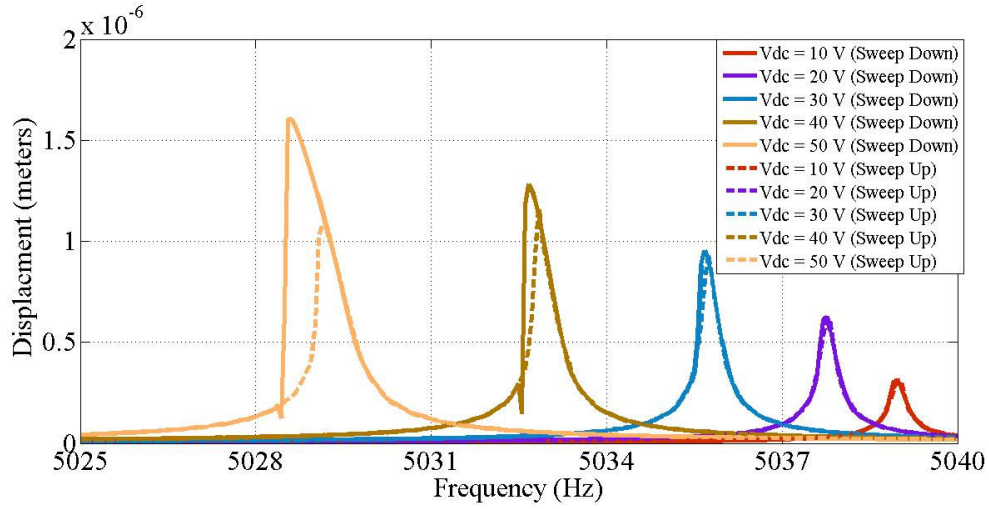


Figure 2-25: The double-sided response for various DC excitation voltages applied to the hybrid suspension gyroscope. However,  $x_0 = 7\mu\text{m}$  instead of  $10\mu\text{m}$ .

## 2.4. Gyroscope Performance Measures

The equations of motions governing the behavior of mass-spring-damping systems of both the drive and sense modes are shown below.

$$m\ddot{x} + D\dot{x} + kx = F \quad (2-25)$$

$$m\ddot{y} + D\dot{y} + ky + 2m\Omega\dot{x} = 0 \quad (2-26)$$

From these equations, we derive that the resonance frequency, quality factor, and bandwidth is calculated by (2-27) – (2-28) – (2-29) respectively:

$$\omega_0 = \sqrt{k/m} \quad (2-27)$$

$$Q = \sqrt{km}/D \quad (2-28)$$

$$BW = \frac{\omega_0}{Q} \quad (2-29)$$

While force  $F$  can be calculated from the electrostatic force, in the case of differential excitation, can be calculated from equations (2-14) and (2-20) to be equal to

$$F = 4\alpha_2 V_{DC} v_{AC} \quad (2-30)$$

Where  $\alpha_2$  is defined in equation (2-10) and represents the derivative of the linear capacitance with respect to the displacement.

The drive displacement at resonance frequency is defined as following:

$$x_d(t)|_{\text{resonance}} = Q \frac{F}{k} = \frac{4Q\alpha_2 V_{DC} V_{AC}}{k} \sin \omega_0 t = X_0 \sin \omega_0 t \quad (2-31)$$

Due to the Coriolis' Force, the sense displacement at resonance is calculated as in equation (2-32)

$$y_d(t)|_{\text{resonance}} = \Omega_z \frac{2Q}{\omega_0} X_0 \cos \omega_0 t = Y_0 \cos \omega_0 t \quad (2-32)$$

$$\text{Where } Y_0 = \Omega_z \frac{2Q}{\omega_0} X_0$$

Both architectures, vertical suspension and hybrid suspension gyroscope, (their dimensions summarized in Table 2-1 and Table 2-2 respectively) can achieve max driving amplitude of drive displacement equal to 4.0  $\mu\text{m}$  by adjusting the input AC excitation voltage and polarization voltages (using numerical model shown in Fig. 2-15). Therefore, and assuming max driving amplitude, equation (2-32) calculates the output sense displacement, for input angular rotation of 1 deg/sec, to equal 150 nm and 115 nm respectively.

From equation (2-4) the change in the output voltage can be derived as follows:

$$\Delta V = V_{\text{Out}}|_{\text{no\_rotation}} - V_{\text{Out}}|_{\text{rotation}} = V_s \left( 0.5 - \frac{l-y}{l} \right) = V_s \left( \frac{l-(l-y)}{l} \right) = V_s \frac{y}{l} \quad (2-33)$$

Where  $l$  is the overlap between the sense comb-drive fingers. So as seen from the latter equation, it's preferred to be as small as possible. The overlap is set to equal 10  $\mu\text{m}$  in both architectures and  $V_s$  equals 10 Volt. Hence,  $\Delta V$  for the sense displacements calculated earlier, equal 150 mV and 115 mV for the vertical and hybrid architectures respectively.

## 2.5. Performance Comparison with the State of The Art and Discussion

Table 2-5 compare between the performance of the vertical, hybrid, and state of the art gyroscope designs. The state of the art design was developed by Ayazi et al at Georgia Institute of Technology [34]. This architecture was used a reference not only because of its high performance but also, it's fabricated using the same SOI bulk micromachining technology. However, the fabrication technology capabilities available at STRC microfabrication facility at AUC are lower than the one used for fabricating the design reported [34]. Therefore, and for the sake of proper comparison, the performance measures reported in Table 2-5 for the proposed designs are calculated assuming same device layer thickness (so that capacitance values would be compared according to proof-mass area fill factor). Also, the comparison is done assuming max displacement for all the architectures.

[34]. Finally, the Mechanical Noise Equivalent Angular Rate is calculated assuming same displacement following the relation reported in equation (2-34) [34].

$$MNE\Omega = \frac{1}{2q} \cdot \sqrt{\frac{4k_B T}{\omega_0 m}} \sqrt{BW} \quad (2-34)$$

When driving displacement  $q$  is assumed to be the same for all the architectures, the  $MNE\Omega$  is reduced by a factor of  $\sqrt{\frac{1}{Qm}}$ .



**Table 2-5: Comparison between the vertical gyroscope, hybrid gyroscope, and state of the art**

| Performance Measure   | State of the art<br>Design [34]                | Vertical Design  | Hybrid Design  |
|---|--|--|--|
| Overall Gyroscope Area  | 2mm <sup>2</sup>                               | 2 mm <sup>2</sup>  | 2mm <sup>2</sup>   |
| Dimensions of the Proof<br>Mass and Proof Mass Area<br>Fill Factor ( <i>PMAFF</i> )                 | 570*570*40μm <sup>3</sup><br><i>PMAFF</i> ~17% | 1000*1000*700μm <sup>3</sup><br><i>PMAFF</i> ~80%<br>(The effective mass is around <b>53</b> times larger due to area<br>and thickness expansion inherent with the novel gyroscope<br>architecture)                      |  |
| Proof Mass ( <i>M<sub>e</sub></i> )   | 0.03mg   | 1.6mg (two orders of magnitude larger)   |  |
| Resonance Frequency ( <i>F<sub>r</sub></i> )<br>for the <b>SAME</b> Stiffness<br>and Support Losses | 17.4KHz  | 3.1 KHz  | 4.9 KHz  |
| Quality Factors for Drive<br>and Sense Modes ( <i>Q<sub>d</sub></i> and<br><i>Q<sub>s</sub></i> )   | 81,000 and 64,000                              | 21,000<br>The relative small aspect ratio of the vertical beams (4:1)<br>limited the quality factor due to the spring losses.<br>With advanced etching technology, this aspect ratio can<br>reach (1:10) and Q = 340,000 |  |
| Max drive Amplitude for<br>the SAME Voltage   | 3 μm   | 4 μm   | 0.6 μm   |
| Sense Amplitude   | 3 nm   | 150 nm   | 115 nm   |
| Mechanical Noise<br>Equivalent Angular Rate<br>(for the same displacement)                          | 0.3 °/hr                                       | 0.08 °/hr  |  |
| Drive and Sense<br>Capacitances ( <i>C<sub>d</sub></i> and <i>C<sub>s</sub></i> )                   | 0.16pF   | 2.2pF (The capacitance is increased only due to improving<br>the PMSAFF, as the active (or electrical) thickness is the<br><b>SAME</b> and equals 40 μm  |  |
| Parasitic or Coupling<br>Sustaining Area for the<br><b>SAME</b> SOI oxide<br>thickness              | 100*570μm <sup>2</sup>                         | 100*100μm <sup>2</sup> (The parasitic<br>Capacitance is then reduced<br>by a factor of 5.7 as a result<br>of the suggested support for<br>the fixed combs)   | The handle wafer is potential<br>less, and therefore, the<br>parasitic capacitance is<br>nearly zero |
| Electrical Output<br>Sensitivity ( <i>S<sub>e</sub></i> )   | 1.25mV/°/s                                     | 150 mV/°/s   | 115 mV/°/s   |
| Signal to Noise Ratio<br>( <i>SNR</i> )   | 4.17mV/ °/hr                                   | 1,875mV/ °/hr (The SNR is<br>improved by <b>three orders<br/>of magnitude</b> )  | 1,437mV/ °/hr (The SNR is<br>improved by <b>three orders of<br/>magnitude</b> )                      |

As shown in the previous table, the utilization of a full set of vertical beams in the vertical suspension architecture resulted in an increase of one order of magnitude in the drive/sense capacitances and area fill factor while the proof-mass increased with two orders of magnitude. The long, flexible, beams and large proof-mass contributed in the reduction of the

resonance frequency and, consequently, the mechanical theoretical noise by one order. Moreover, the output sensitivity of the gyroscope was increased by two orders of magnitude. Total SNR is enhanced by three orders of magnitude.

On the other hand, the hybrid suspension gyroscope nearly eliminated the parasitic capacitances between the drive/sense and the proof-mass. This would contribute significantly in eliminating any existent mechanical coupling using the differential sensing scheme discussed in section 2.2.1. In addition, and as shown in the next chapter, the fabrication process flow of this architecture is much easier and much cheaper (two masks instead of four in the vertical suspension gyroscope case). It's also worth mentioning that this architecture did not affect the proof-mass area fill factor, capacitance, or the quality factor (keeping the mechanical noise equivalent rotation the same as at the vertical suspension architecture). However, these advantages did not come priceless. The stiffer horizontal beams used caused an increase of the resonance frequency from 3.1 KHz to 4.9 KHz. Hence, slight decline in the output sensitivity and SNR. Nonetheless, the hybrid suspension architecture is considered to be fine trade-off between the fabrication simplicity (low cost) and the high performance (of the vertical suspension design).

### **3. Chapter III: Devices Fabrication & Characterization**

This chapter illustrates the fabrication process flow of vertical suspension and hybrid suspension gyroscopes studied in this thesis. Challenges such as selection of the masking material, etching profile optimization, notching effect, and the maximum achievable etching depth are presented in detail. It can be concluded from the discussions presented and the illustration of the fabrication process for both architectures that the hybrid suspension design is much easier in fabrication, and consequently, cheaper. After that, the working mechanism and the physics beyond the micromachining facilities, used during fabrication, are explored. Finally, the characterization of the gyroscope mechanical performance is provided. The frequency response of the mass-spring-damping system of the gyroscope drive and sense modes are presented, in addition to an illustration of the measurement setup.

#### **3.1. Vertical Suspension Device Fabrication**

The most important feature of the proposed novel design relies on the implementation of the out-of-plane suspension system. This requires fabricating vertical beams as shown in Fig. 3.1.A. The process flow is mainly based on defining the vertical beam using two prints (one from each side of the wafer). These two prints will be referred to in this study as Contacts and Suspension. The name contact was chosen because this print is used to define areas where the handle wafer is electrically connected to the device wafer. While the name suspension has been selected to define three side of the vertical beams used in the suspension system. Fig. 3-1-b shows the shape of the device wafer (from the backside of the wafer) after etching both Contacts and Suspension masks. On the other hand, Fig. 3-1-c shows the proof mass and the suspension (back-side of the wafer) after etching the Suspension mask only. It can be understood from the photos of Fig. 3-1 that one side of the vertical beam is defined using the Contact mask (etched from the wafer front side) while the other three masks are defined using the Suspension mask (etched from the wafer backside).

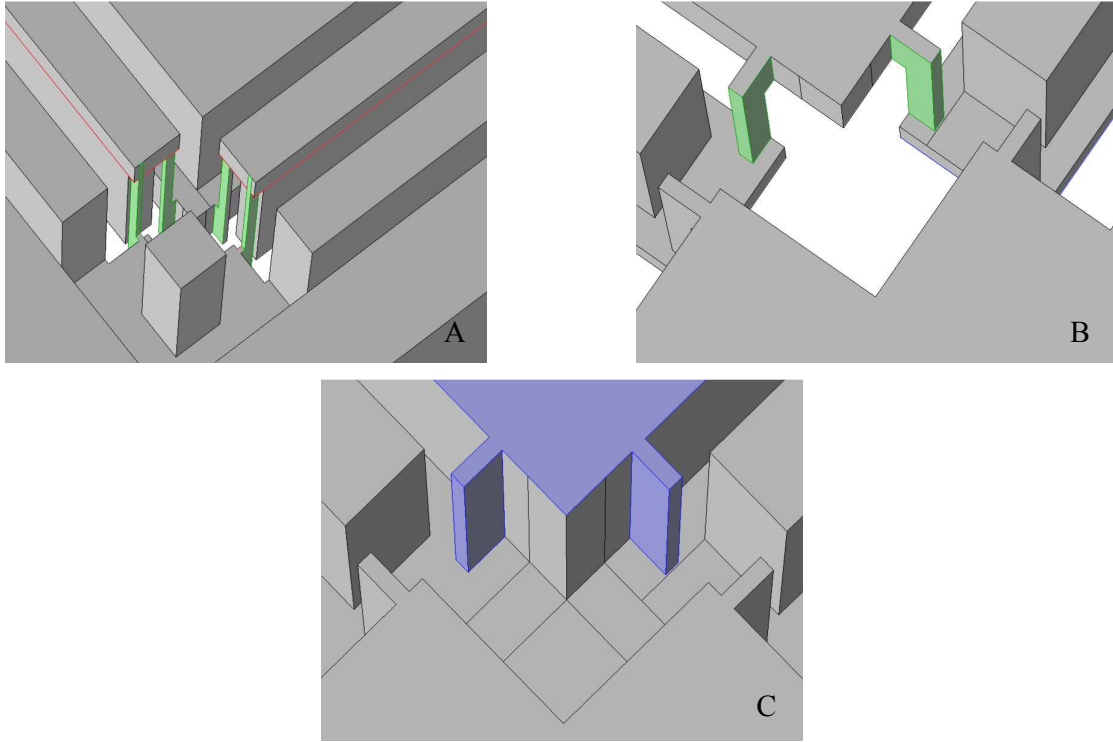


**Figure 3-1: Vertical suspension system 3D model. a) Front-side snapshot. b) Back-side snapshot. c) Back-side snapshot for vertical beams defined from three sides only (no Contacts etching).**

One of the main challenges in the device fabrication is realizing the adequate electrical connections. The bottom side of proof mass (in the handle wafer) is suspended (connected through the vertical beam) to the movable part of the comb-drive as seen in Fig 3-2. The latter is anchored, through another vertical beam, to the bulk of the handle wafer. As the device is planned to be fabricated on Silicon-On-Insulator (SOI) wafer, the middle of these two vertical beams is made of  $\text{SiO}_2$  which is electrically insulating. Thus, the proof mass, movable comb-drive, and the anchors will be electrically disconnected. This issue has been handled by forming via through the movable comb-drives and the anchors through the Si- $\text{SiO}_2$ -Si stack layers. These vias are later coated with a conductive layer of poly SiGe deposited using Low Pressure Chemical Vapor Deposition (LPCVD). This coating ensures the presence of the required electrical connection between the three different parts mentioned earlier. These vias are defined during the Contacts mask print.

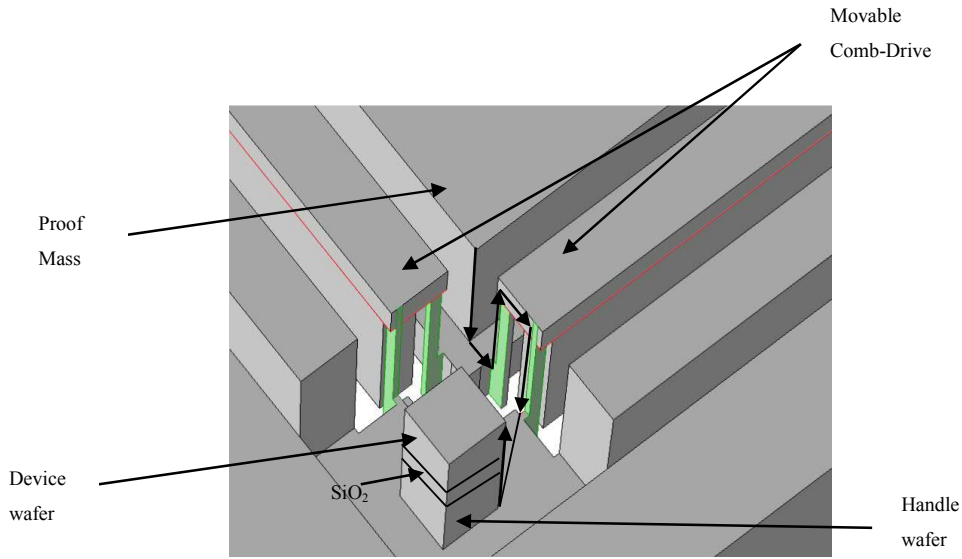


Figure 3-2: Electrical connection to the proof-mass in the vertical suspension design.

### 3.1.1. Fabrication Process Flow

The process flow is illustrated by examining the cross-section of the substrate through the device fabrication. An SOI wafer with 100  $\mu\text{m}$  device wafer, 1  $\mu\text{m}$   $\text{SiO}_2$  layer, and 500  $\mu\text{m}$  handle wafer is used. First, a layer of photoresist (AZ 9260) is spin (cf. Fig. 3-3) and the Contacts mask is printed on the front-side (cf. Fig. 3-4). This mask defines via (for electrical connections as illustrated before) and one of the four sides of the vertical beams (as illustrated in section 3-1). An etching process is performed in the Deep Reactive Ion Etching (DRIE) for etching Si of the device wafer,  $\text{SiO}_2$  layer, and 400  $\mu\text{m}$  inside the handle wafer (Figs. 3-4, 3-5). Then, high conductivity (boron doped) SiGe was deposited in CVD to provide the selected electrical short-circuit to the handle wafer as shown in Fig. 3-6. Then, photoresist is spray-coated on the front-side of the wafer and the Fingers mask is printed. This mask defines the size of the proof mass, fingers, and comb-drives. The SiGe mask was etched in DRIE followed by Si etching for the device wafer till the  $\text{SiO}_2$  layer was reached as shown in Figs. 3-7, Fig. 3-8.

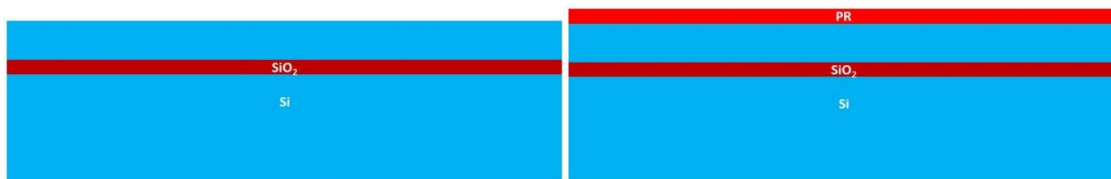


Figure 3-3: a) SOI wafer (100  $\mu\text{m}$  device wafer, 1  $\mu\text{m}$   $\text{SiO}_2$ , and 500  $\mu\text{m}$  handle layer). b) Coating wafer with positive photoresist (PR) on spinner.



Figure 3-4: a) print Contacts mask. b) Etch 100  $\mu\text{m}$  Si in DRIE.

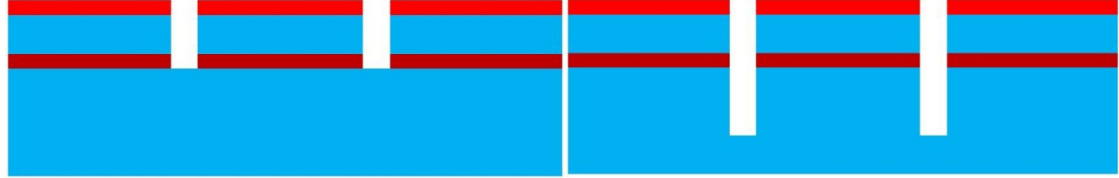


Figure 3-5: a) Etch intermediate  $\text{SiO}_2$  in DRIE. b) Etch 400  $\mu\text{m}$  Si in DRIE.



Figure 3-6: a) Strip photoresist using Acetone. b) Deposit poly SiGe in LPCVD.

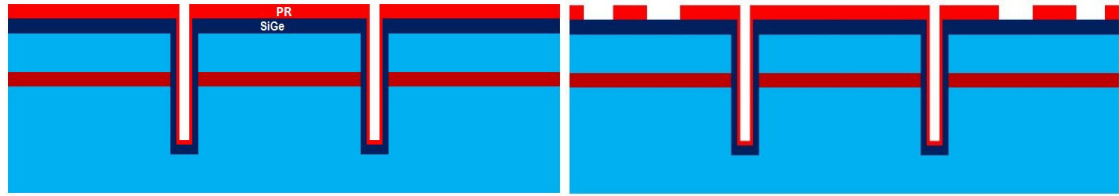


Figure 3-7: a) Spray coat photoresist (PR). b) Print Fingers mask.

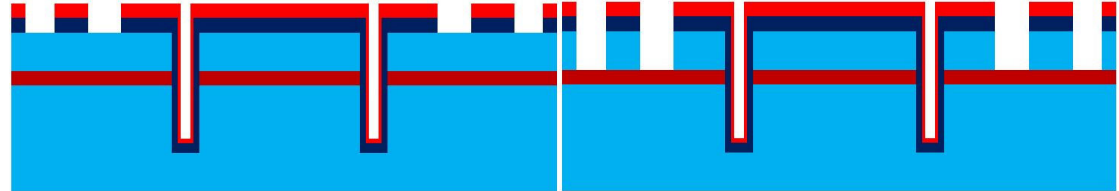


Figure 3-8: a) Etch SiGe film in DRIE. b) Etch 100  $\mu\text{m}$  Si in DRIE.

After that, a layer of photoresist (AZ 9260) is spin on the backside of the wafer and the Isolation mask is printed as show in Fig. 3-9, Fig. 3-10. The purpose of this mask is to create a different level between the moving proof mass and the bulk of the handle wafer to prevent friction during testing. Hence, this print is used to etch the Si for less than 30  $\mu\text{m}$  (as shown in Fig. 3-10). Also, it is important to etch all the silicon beneath the fixed comb-drives to reduce the parasitic capacitances between comb-drives and the movable proof-mass. Finally, photoresist is spray-coated on the back-side of the wafer and the Suspension mask is printed as shown in Figs. 3-11 to Fig. 3-12. The purpose of this mask is to define the other three parts of the vertical beams (as illustrated before in section 3.1) by etching Si of the handle wafer

for 470  $\mu\text{m}$ . Afterwards, a Cu metallization layer is deposited and patterned using lift-off process to enable wire bonding for testing purposes.

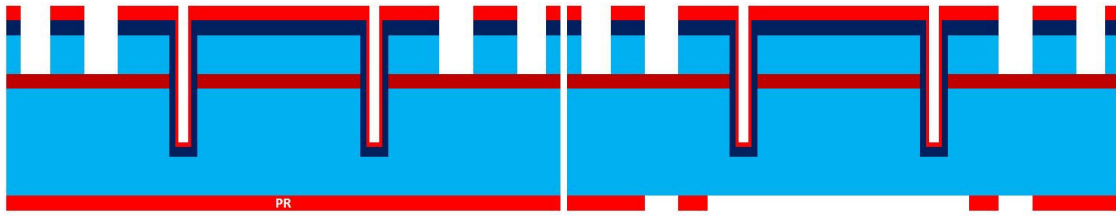


Figure 3-9: a) Spin photoresist on the wafer backside. b) Print Isolation mask.

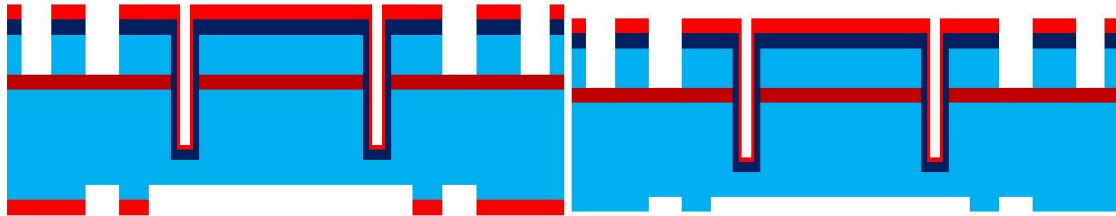


Figure 3-10: a) Etch 30  $\mu\text{m}$  Si in DRIE. b) Strip photoresist using Acetone.

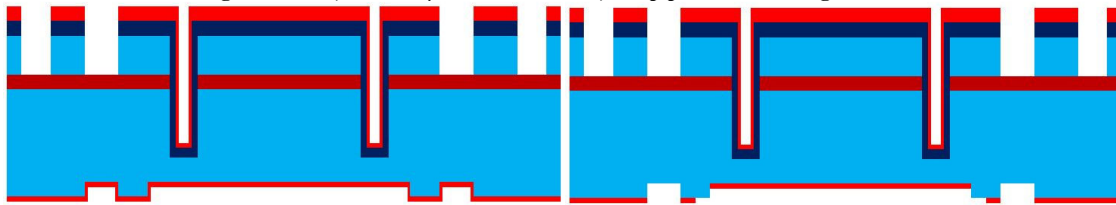


Figure 3-11: a) Spray coat photoresist. b) Print Suspension mask.

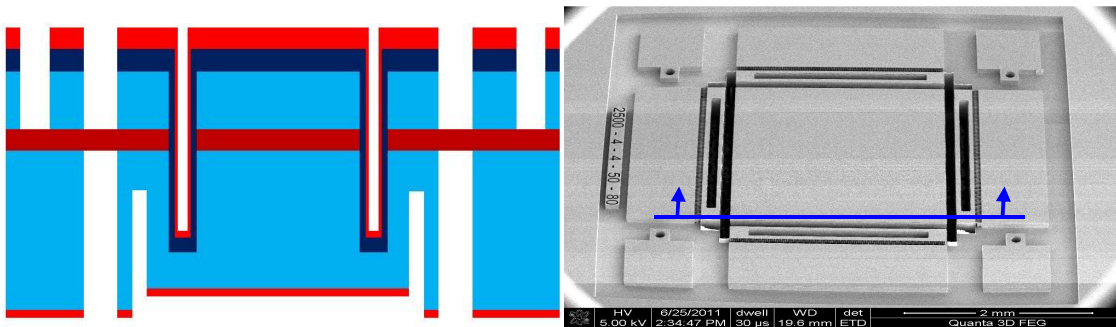


Figure 3-12: a) Etch 470  $\mu\text{m}$  Si in DRIE (Cross-section of the completed device). b) Frontside SEM photo of the fabricated device.

### 3.1.2. Layout

As illustrated in the process flow earlier, this version of the gyroscope needs four masks (excluding the metallization mask). These five masks are Contacts, Fingers, Isolation, Suspension, and Metallization are shown in Figs. 3-13 to Fig. 3-16. The Contacts, Fingers, and Metallization masks are printed on the device layer (front-side surface of the wafer)

while Isolation and Suspension masks are printed on the handle wafer (back-side surface). This requires that masks of each set are mirrored, around the y-axis, relative to the other set of masks to ensure proper alignments after fabrication. This mirroring is done while fabricating the Chrome masks.

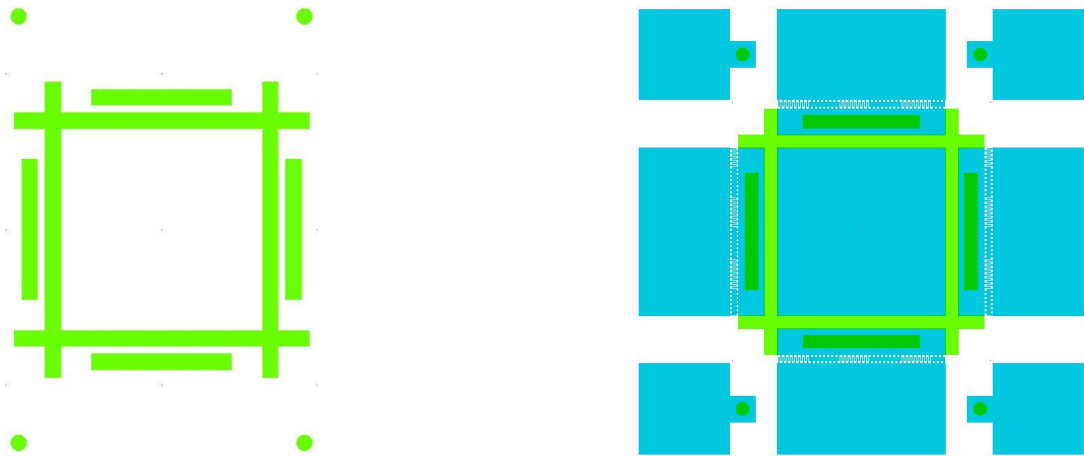


Figure 3-13: Fingers mask (light blue; light field) and Contacts (green; dark field)

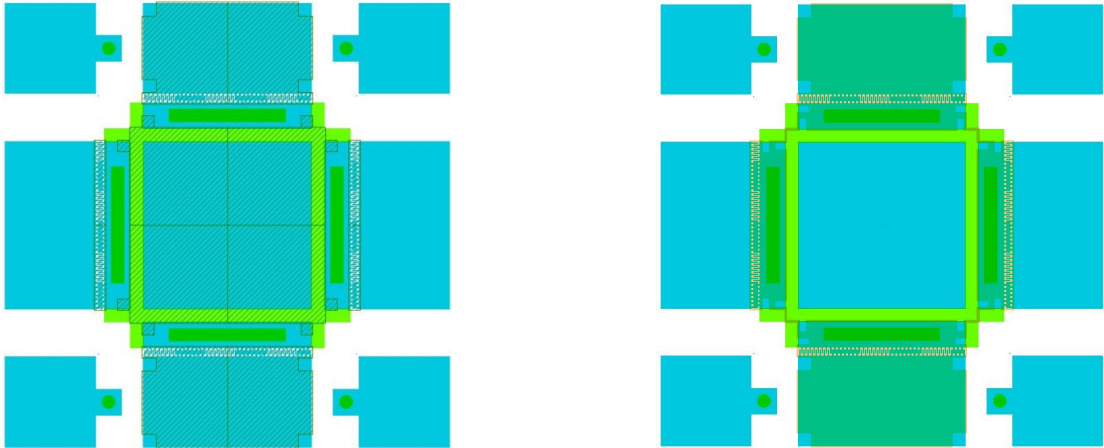


Figure 3-14: Contacts mask (green; dark field), Fingers (light blue; light field), Isolation (stripes; dark field), and Suspension (dark green; dark field).



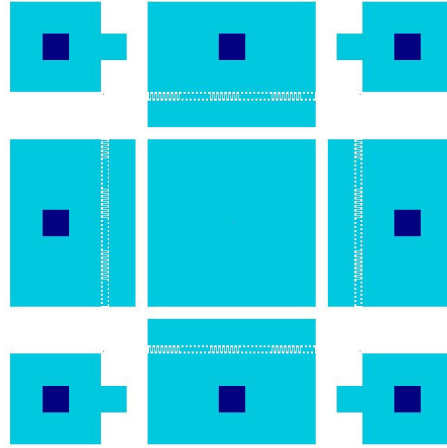


Figure 3-15: Fingers mask (light blue; light field) and Metallization (dark blue; light field).

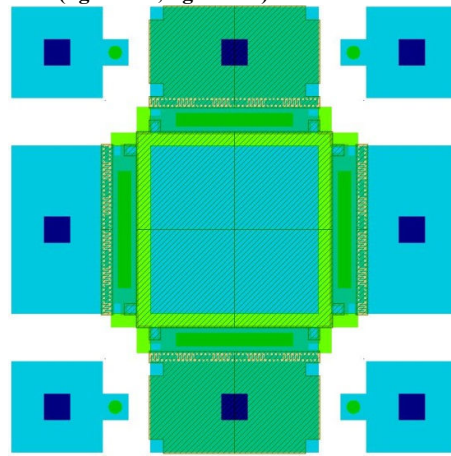


Figure 3-16: Layout of vertical suspension system based gyroscope.

It's worth mentioning that each mask defined by either being a Dark-Field or Light-Field mask. These definitions are provided, with the layout, to the masks manufacturers to obtain the right shape after fabrication. Dark-Field states that the areas drawn (colored) on the layout should be transparent on the mask while Light-Field identifies these areas as Cr (ultraviolet absorber).

### 3.2. Hybrid Suspension Device Fabrication

The main advantage of the latter architecture is the direct connections between the proof mass (the movable part of the comb-drive) to the anchors using horizontal beams. Such scheme enables merging Fingers and Contacts masks together into a single mask. This was done through etching the Fingers mask for 500  $\mu\text{m}$  in the SOI wafer and eliminating the Contact mask. This action was not feasible in the previous version because the Contacts mask was used to define (selected) areas where SiGe deposition is made to provide proper electrical

connections between anchors and proof mass (cf. Fig. 3-17). SiGe was selected because it's deposited using CVD which has good step coverage. Also, it has good conductivity and not as contaminated as most of the metals.

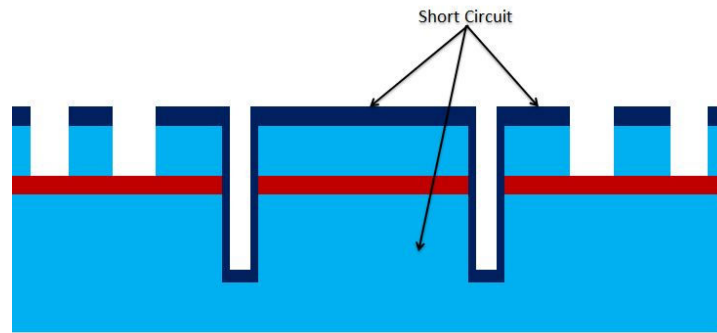


**Figure 3-17: Electrical signal connection using through handle wafer in vertical suspension version.**

The electrical connections are made directly between the proof-mass and the anchors through horizontal beam in the hybrid version as seen Fig 3-18.

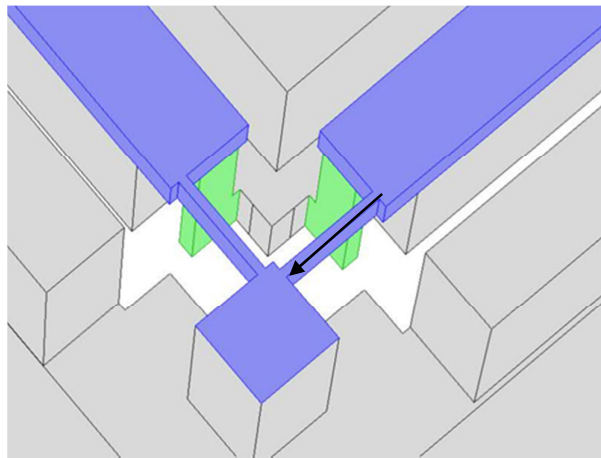


**Figure 3-18: Electrical connection to the proof-mass in the hybrid suspension design**

Also, realizing this connection in the device wafer leads to cancelling the parasitic capacitance (cf. Fig. 3-19) between different electrodes completely. Hence, the fabrication process is more simplified as both the Contacts and Isolation masks are not needed.

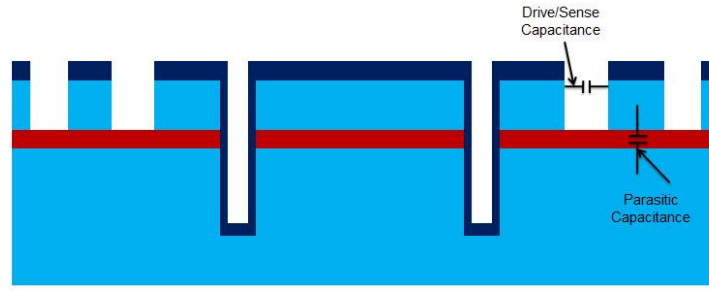


Figure 3-19: Origin of the parasitic capacitance between the drive/sense comb-drive and proof mass in vertical suspension version.

In addition, the need for the Isolation mask to provide raise the level of the proof mass to prevent any friction with the characterization table is not needed anymore. This is due to the use of the lower cap wafer, bonded to the SOI backside, with a recess beneath the proof mass. This step is discussed in detail at chapter 4 which deals with the devices packaging.

### 3.2.1. Fabrication Process Flow

Also an SOI wafer with 100  $\mu\text{m}$  device wafer, 1  $\mu\text{m}$   $\text{SiO}_2$  layer, and 500  $\mu\text{m}$  handle wafer is used. First, a layer of photoresist (AZ 9260) is spin and the Fingers mask is printed on the front-side (Fig. 3-20 to Fig. 3-21). This mask defines the horizontal beams (part of the suspension system and used electrical connections as illustrated before) and one of the four sides of the vertical beams. Besides, it defines the size of the proof mass, fingers, and comb-drives. An etching process is performed in the DRIE for the device wafer Si,  $\text{SiO}_2$  layer, and 400  $\mu\text{m}$  inside the handle wafer (cf Fig. 3-22).

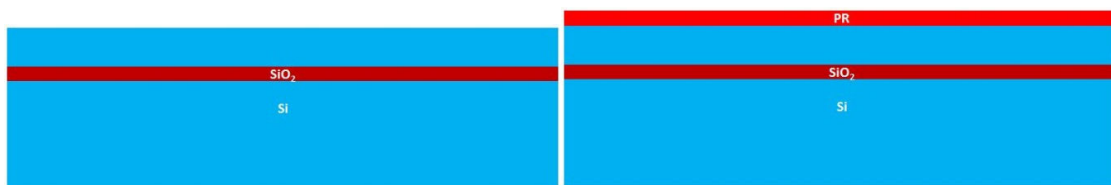


Figure 3-20: a) SOI wafer (100  $\mu\text{m}$  device wafer, 1 $\mu\text{m}$   $\text{SiO}_2$ , and 500  $\mu\text{m}$  handle layer). b) Coating wafer with positive photoresist (PR) on spinner.

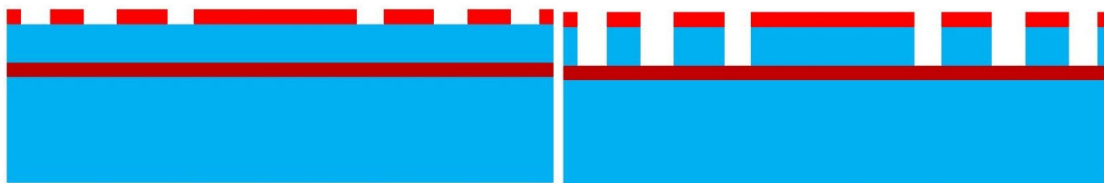


Figure 3-21: a) Print Fingers mask. b) Etch 100  $\mu\text{m}$  Si.

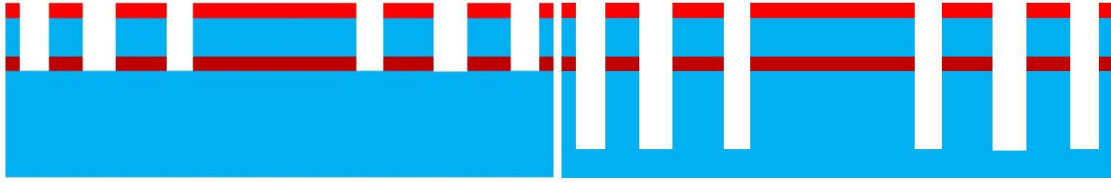


Figure 3-22: a) Etch 1  $\mu\text{m}$   $\text{SiO}_2$ . b) Etch 400  $\mu\text{m}$  Si.

Then, a layer of photoresist (AZ 9260) is spin on the backside of the wafer as shown in Fig. 3-23 and the Suspension mask is printed as shown in Fig. 3-23. The purpose of this mask is to define the other three parts of the vertical beams by etching Si of the handle wafer for 500  $\mu\text{m}$  (i.e. etching through the handle wafer and stops by reaching the intermediate  $\text{SiO}_2$ ) as seen in Fig. 3-24. Finally, a Cu metallization layer is deposited and patterned using lift-off process to enable wire bonding for testing purposes. Fig. 3-25 shows the substrate final cross-sections and SEM image of the final fabricated device.

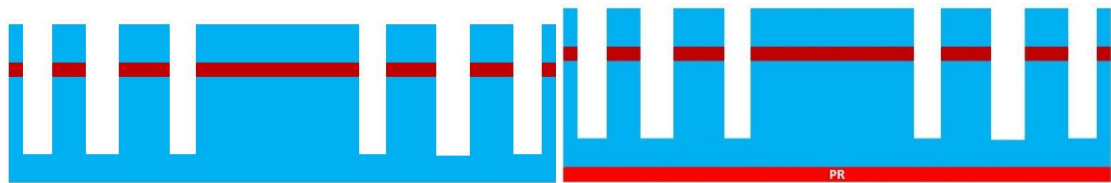


Figure 3-23: a) Strip photoresist. b) Spin photoresist on substrate backside.

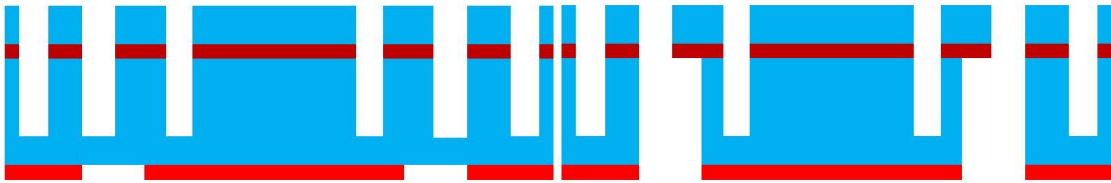


Figure 3-24: a) Print Suspension mask. b) Etch 500  $\mu\text{m}$  Si.

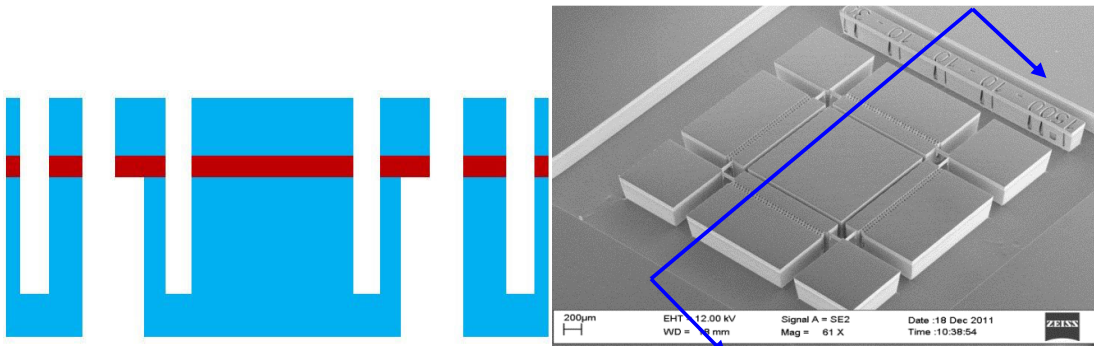


Figure 3-25: Strip photoresist (Cross-section of the completed device).

### 3.2.2. Layout

As discussed in the previous section, the simplicity of the process flow for fabricating this version of the gyroscope results in the need of using two masks only (excluding the Metallization mask). These masks are Fingers and Suspension and they are shown in Figs. 3-26 to Fig. 3-28.

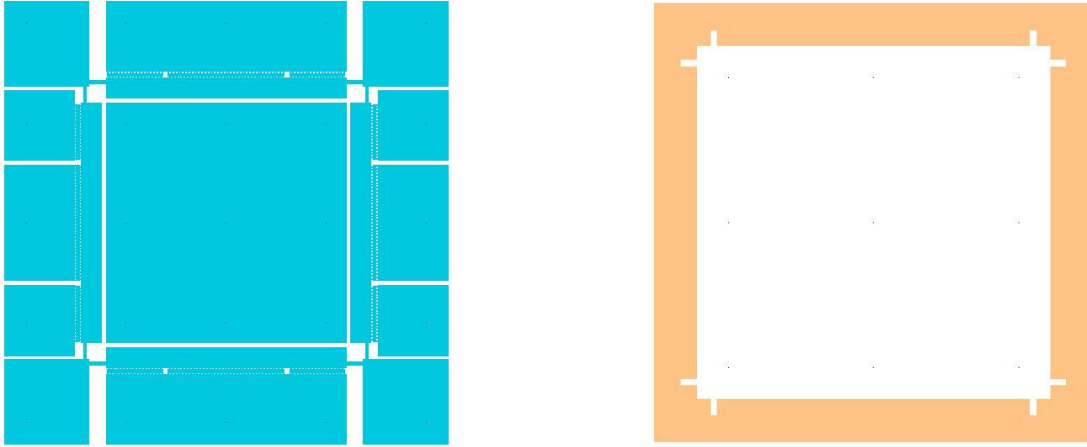


Figure 3-26: a) Fingers mask (light field), b) Contacts mask (dark field).

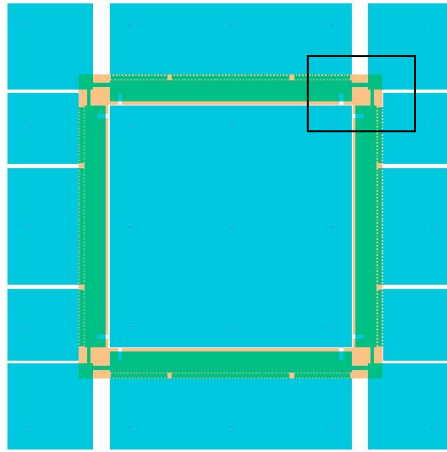
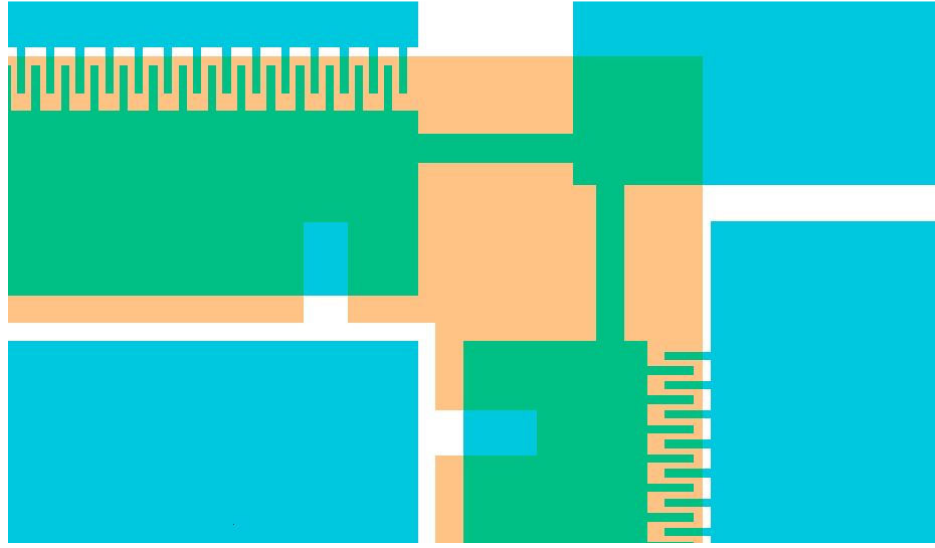


Figure 3-27: Layout of hybrid suspension system based gyroscope.



**Figure 3-28: Hybrid (vertical and horizontal) suspension system.**

### **3.3. Developing the Etching Process**

A prerequisite for the successful realization of the two proposed high performance inertial sensor is a reliable and reproducible micromachining technology. For the proper functioning of the two proposed MEMS devices, it is required to realize structures that involve high aspect ratios, deep trenches, and through wafer etching. Meanwhile, it is required to maintain high surface finish, vertical sidewalls, fast etch rates and high anisotropy, which, when combined represent great challenges in the micromachining processes. Consequently, a systematic technology development procedures were adopted with four specific optimization criteria in mind, namely, enhancing sidewall smoothness, controlling profile inclination, maximizing etch rate and mask selectivity, and finally, process reproducibility. As a result of this study, we could successfully realize trenches up to 400  $\mu\text{m}$  with high aspect ratios up to 1:20 at high etch rates up to 4  $\mu\text{m}/\text{min}$  using our microfabrication facilities at the AUC and KAUST.

#### **3.3.1. Cryogenic DRIE Process**

Deep cryogenic etching of silicon using an inductively coupled plasma reactive ion etcher (ICP-DRIE) is gaining much attention as it eliminates scalloping typically observed in the Bosch process, hence enabling the realization of smooth vertical walls. In this process, the silicon etch product from the  $\text{SF}_6$  etch chemistry,  $\text{SiF}_x$ , condenses on the sidewalls and combines with the reactive oxygen to create the  $\text{SiO}_x\text{F}_y$  passivation layer, which protects the

sidewalls and results in anisotropic etching (i.e., vertical sidewalls). The passivation layer is mainly maintained by reducing the temperature which should be lower than  $-80^{\circ}\text{C}$  and its thickness is determined by the ratio of  $\text{SF}_6$  to  $\text{O}_2$ . The process parameters to be optimized are the  $\text{SF}_6$  flow, RF power, oxygen content, and process temperature. It is well known from literature that the temperature and oxygen content are the most sensitive parameters in cryogenic etching. Therefore, they will be the major players in the fine-tuning of the profile and surface finish. Whereas, the process pressure was fixed at 10 mTorr for minimal bottling and footing effects. Also, the helium backside pressure was fixed at 10 Torr for most experiments and 20 Torr for thick SOI wafers for most efficient cooling.

### 3.3.2. Profile Optimization

The etched profile is influenced by all parameters. Generally, the profile becomes more positively inclined with lower  $\text{SF}_6$  flow, higher oxygen content, lower RF power (dc-bias), and higher temperature. Our optimization approach started with a process provided by Oxford Instruments. Then we proceeded by adjusting  $\text{SF}_6$  flow and oxygen content for coarse profile control, and then adjusted the process temperature for fine profile control.

The adopted approach has two major limitations; the first is the formation of black silicon under some oxygen content/temperature conditions (cf. Fig. 3-29), which represents the upper ceiling of the oxygen content. And the second is the undercut, which is caused due to isotropic etching either due to loss of passivation at the interface with the mask or due to excessive chemical etching, which represents the upper ceiling for  $\text{SF}_6$  flow and temperature.

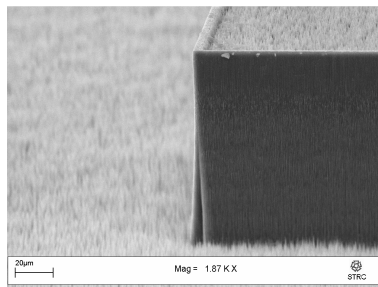


Figure 3-29: Black Silicon formed at 13 sccm  $\text{O}_2$ , 100 sccm  $\text{SF}_6$  at  $120^{\circ}\text{C}$

### 3.3.3. Surface Finish

Better surface finish (i.e., smooth sidewalls) can be achieved by maintaining strong passivation throughout the etching process as well as increasing etching directivity. This can

generally be achieved through increasing both oxygen content and RF power (i.e., dc-bias) while reducing temperature.

### 3.3.4. Undercutting

As the trench gets deeper, the top part of the passivation layer heats up and accordingly passivation starts to break at this region and under-etching occurs (cf. Fig. 3-30). Such phenomenon imposes major limitations on the maximum possible depth.

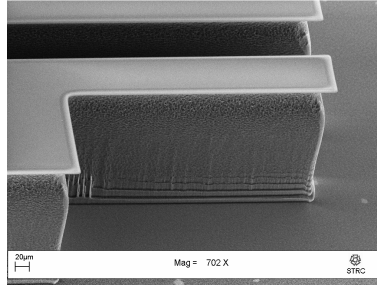


Figure 3-30: Undercut formed after 64 minute etching at 120°C and variable O<sub>2</sub> to SF<sub>6</sub> concentrations

### 3.3.5. Masking Material

Having a masking layer that can stand deep etching is another process challenge. Thick layer photoresist cracks at low temperatures (<100°C) due to inherent stresses. The etching selectively of SiO<sub>2</sub> depends strongly on the preparation conditions being either plasma enhanced chemical vapor deposition or thermal oxide. For both cases a thick oxide layer (> 4 μm) might not be sufficient for etching trenches beyond 250 μm. Hence, imposing another limitation on getting deep trenches.

#### 3.3.5.1. Copper as an etching mask

Therefore, Copper (Cu) was tried as an etching mask to overcome the latter problem. A copper film of 2 μm thickness was deposited by RF Magnetron Sputtering on the front-side of SOI wafer to be used as a protective mask for Si-SiO<sub>2</sub>-Si etching. However, several problems were faced during this process such as the reduction in the features resolution (especially affecting the Fingers) due to the isotropic wet etching used to pattern the Cu mask (cf. Fig. 3-31). Also, the DRIE chamber contamination due to Cu sputtered off the film (during ion bombardment in the etching process). Moreover, the Cu mask had high intrinsic stresses relative to the SiO<sub>2</sub> or SiN films. This high stresses causes high risk of mask destruction of even getting peeled off the substrate (cf Fig. 3-32). Also, It's believed that this



stress causes under etching (etching underneath the protected features) which destroys the important structures such as comb-drive fingers as demonstrated in Fig. 3-33.

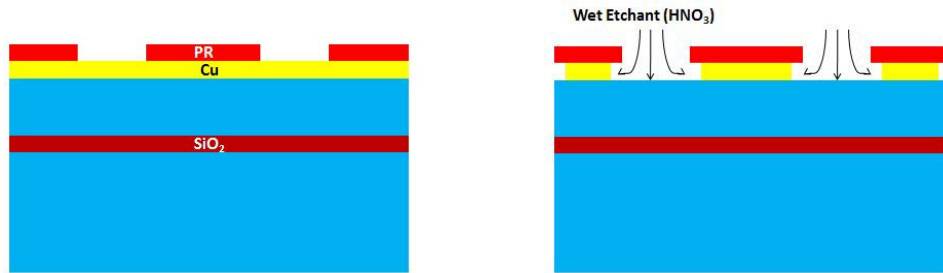


**Figure 3-31: Wet isotropic etching on reduces the resolution**

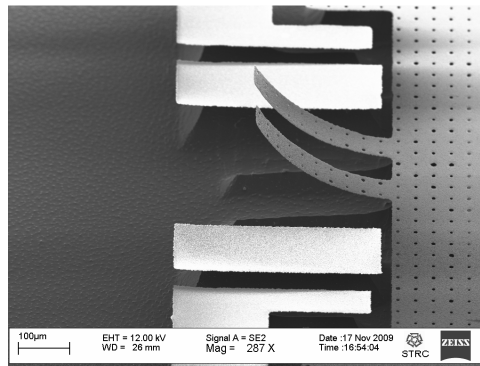


**Figure 3-32: SEM of cantilevers showing the high intrinsic stresses associated with Cu film**

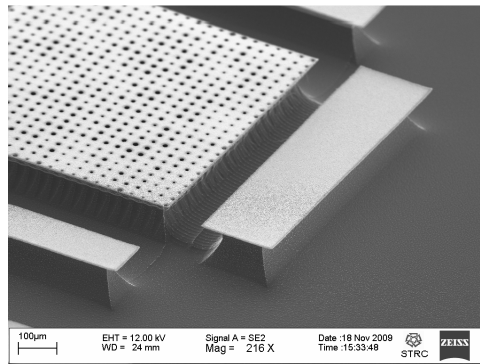


**Figure 3-33: Undercut which destroyed critical features of the structures**

### 3.3.6. Depth Dependent Profile

It was observed in literature, that for high aspect ratio trenches, there are some depth limitations beyond which concentration of the etching to passivation gases become imbalanced which results in weaker passivation and excessive chemical etching which leads to negative profile. One way to overcome this limitation is by increasing the RF power,

which helps to flush away the etching products from the bottom of the trenches and help maintain the balance between the etching and the passivation species.

### 3.3.7. Profile Optimization Results

The reactive radicals in  $\text{SF}_6$  are responsible for the chemical etching of silicon, therefore, increasing  $\text{SF}_6$  flow results in increasing Etch rate while reducing anisotropy which generally results in negative profile and might lead to undercutting in extreme cases (cf. Figs. 3-34-a & 3-34-b).

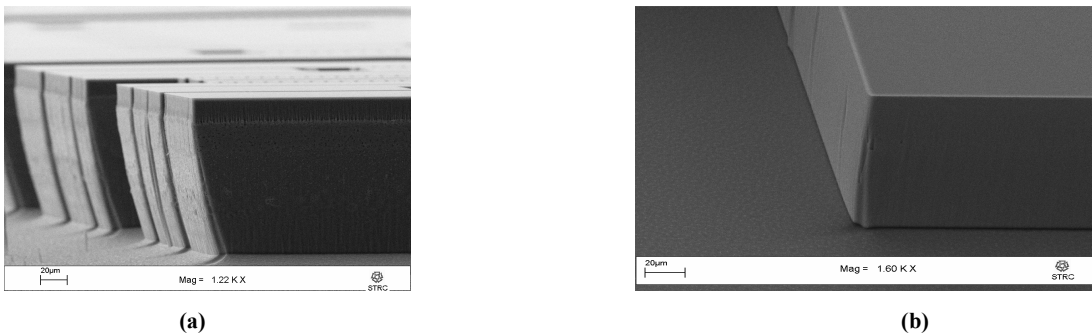


**Figure 3-34: a) Negative profile generated after 60' etching at 9 sccm  $\text{O}_2$ , 100 sccm  $\text{SF}_6$  and  $-120^\circ\text{C}$ . b) Positive profile generated by decreasing  $\text{SF}_6$  content to 90 sccm**

Adjusting the oxygen content affects the etch profile and surface finish. By increasing oxygen, a positive sidewall slope is generated with the risk of grass formation (black silicon). Decreasing oxygen weakens the passivation and might increase the risk of undercut (cf. Figs 3-35-a to 3-36-b).

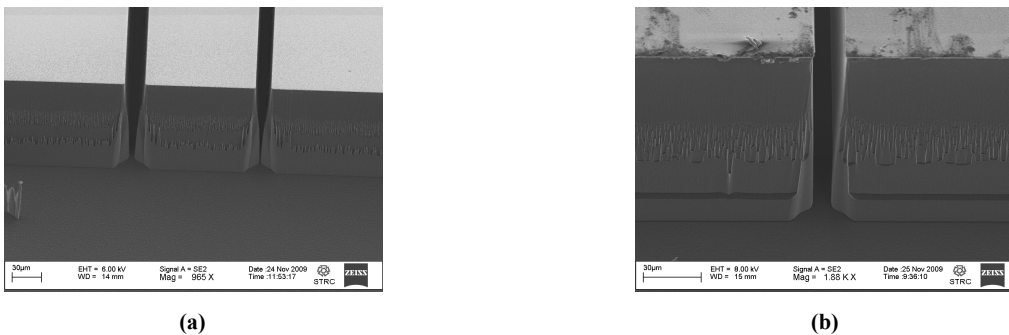
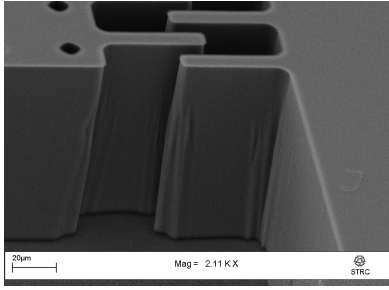
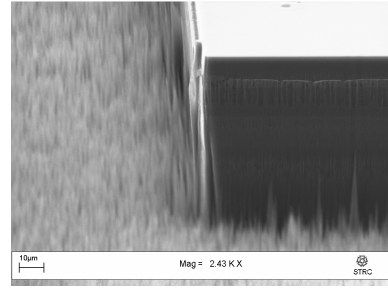


**Figure 3-35: a) Positive profile generated at 11 sccm  $\text{O}_2$  content and 100 sccm  $\text{SF}_6$  at  $-100^\circ\text{C}$ . b) Profile became less positive by reducing  $\text{O}_2$  content to 10 sccm**



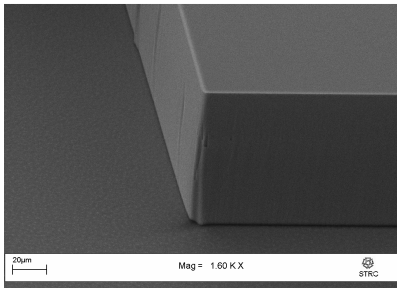
(a)



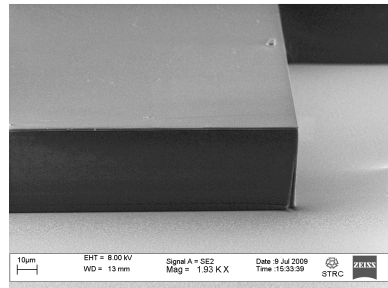
(b)

**Figure 3-36: a) Further reduction of  $O_2$  to 9 sccm while adjusting  $SF_6$  to 90 sccm at  $-120^\circ C$  results in more straight profile. b) Increasing  $O_2$  content beyond 13% at  $-120^\circ C$  results in black silicon formation**

Cooling enhances the selectivity of Si with respect to mask. Moreover, the temperature can be utilized as an independent factor to control the profile without affecting the other parameters. Generally higher temperatures require more oxygen to maintain the passivation and prevent undercut (cf. Figs 3-37-a & 3-37-b).



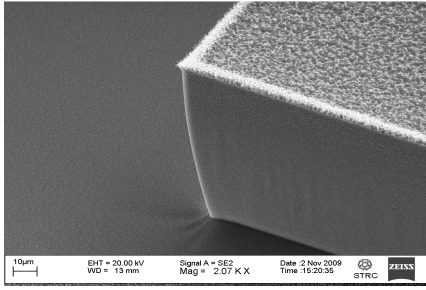
(a)



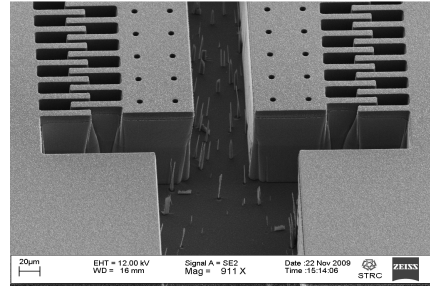
(b)

**Figure 3-37: a) A slightly positive profile at  $-120^\circ C$  and 9 sccm  $O_2$ , 90 sccm  $SF_6$ . b) Profile became less positive by increasing the temperature  $-115^\circ C$**

Increasing RF power increases dc-bias, which provides more directivity to the ions and results in higher anisotropy. However, excessive RF power can result in loss of mask (i.e. lower selectivity), undercutting and damaged sidewalls (cf. Fig. 3-38). Reducing the RF power improves mask selectivity and surface finish by reducing the physical etching due to ion bombardment.

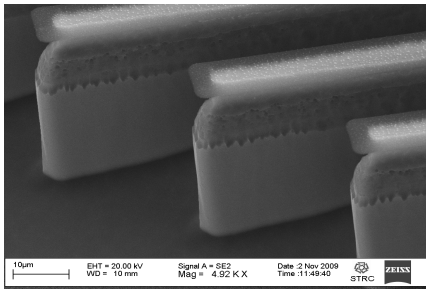


(a)

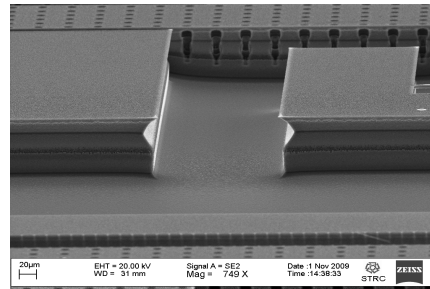


(b)

**Figure 3-38: a) Loss of mask after 60 minute etching at 5 W RF power, 6 sccm O<sub>2</sub>, 90 sccm SF<sub>6</sub>, and -140°C. b) Also negative profile is observed at same conditions in Fig. 3-36-a**



(a)



(b)

**Figure 3-39: a) Undercutting and damage of mask after 30' minute etching, at 10 W RF power and 6 sccm O<sub>2</sub>, 90 sccm SF<sub>6</sub>, -140°C. b) Complete sidewall damage when RF power was increased to 15 W and 6 sccm O<sub>2</sub>, 90 sccm SF<sub>6</sub>, -140°C**

Increasing ICP power help increase the density of the etching species and therefore increases the etch rate. Nevertheless, increasing the chemical etching species from SF<sub>6</sub> can result in increased risks of undercut.

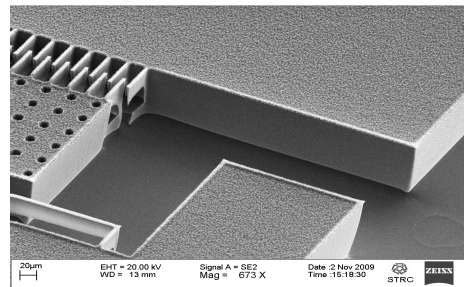
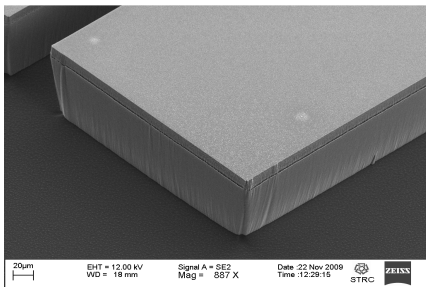


**Figure 3-40: a) at 1000 W ICP power, a negative profile started to form (9 sccm O<sub>2</sub>, 90 sccm SF<sub>6</sub>, 60" 4 W, -120°C). b) at 900 W ICP power, profile is more straight (6 sccm O<sub>2</sub>, 90 sccm SF<sub>6</sub>, 60" 5 W, -140°C)**

### 3.3.8. Notching effects at the Si-SiO<sub>2</sub> interface

Notching effect is a problem associated with intermediate SiO<sub>2</sub> layer is reached during etching Si of the device wafer. It's observed that the bottom layer of the structures, at the interface of SiO<sub>2</sub> and device wafer Si, was suffered from severe destruction. This observation

was reported before in the literature [54] and called as the notching effect. As the  $\text{SiO}_2$  is an insulating material, the charged ions used in the etching process are charged upon its surface and consequently attacks the sidewalls of the structures. The authors in [54] solved this problem by using a low-frequency power supply to generate the plasma while etching the intermediate layer. As this special tool was not available at YJSTRC labs, a different etching recipe is used to etch the intermediate  $\text{SiO}_2$  layer. This recipe is using different reactive gases ( $\text{CHF}_3$  and Ar) that etch, chemically not by ion bombardment, directly the intermediate  $\text{SiO}_2$  layer. Afterwards, the Si etching process is resumed till the required depth of 500  $\mu\text{m}$  is reached. However, the execution of the latter process limited the materials of the etching masks that can be used. As the use of  $\text{SiO}_2$  or  $\text{SiN}$  as a etching mask is not possible because the mask would be destroyed while etching the intermediate  $\text{SiO}_2$ .

### **3.3.9. Switching to Bosch process**

Due to the failure of the Cu mask, thick (10  $\mu\text{m}$ ) positive photoresist was tried to be used for etching the stack. However, cryogenic process (process temperature  $<-90^\circ\text{C}$ ) caused severe cracks in the etching mask and hence etching was not successful. A technology was developed in the YJSTRC lab of using  $\text{CHF}_3$  plasma in DRIE chamber to strengthen the photoresist film. When the photoresist is treated in  $\text{CHF}_3$  plasma, the film is fluorinated where H atoms are replaced by heavier F atoms increasing the film capability to withstand the cryogenic temperature [55]. Although, the technology succeeded in strengthens the photoresist film to the extent that it did not crack at cryogenic temperatures, the film (due to reduction in its thickness) could not survive the etch of the required 500  $\mu\text{m}$ .

Therefore, the etching mechanism for Si is switched from Cryogenic to Bosch process. For this technology the etching is done at moderate temperatures (process temperature  $>-20^\circ\text{C}$ ) where photoresist can be used as a protective etching mask. Therefore, a positive photoresist can be sufficient for etching both  $\text{SiO}_2$  and Si.

## **3.4. Micromachining Facilities**

Fabricating the micromachined gyroscope required the use of several fabrication techniques which required a lot of optimization to realize the required features of the device. This section introduces these different techniques, their working methodologies, and the optimized recipes for different processes which were developed in the YJSTRC labs.

### 3.4.1. Deep Reactive Ion Etching (DRIE)

Two etching mechanisms are used generally in micromachining technology, which are wet and dry etching. Wet etching is done by immersing the substrate in a chemical that is selectively etch a targeted material previously formed on the substrate or etch the substrate material itself. This technique is favored in industry because of its high throughput, low cost, and smooth surfaces [56]. However, the etching direction of the chemical results in isotropic etching which could be disfavored in many applications [56].

On the other hand, dry etching is done through plasma ions (inert or reactive gases) bombarding, the surface of the substrate performed in vacuum chamber. Although many techniques originate of this mechanism, DRIE is the most famous. In DRIE, the reactive gases ( $\text{SF}_6$  in the case of etching Si) enter a chamber where they are ionized by a glow discharge. Then a DC potential is used to direct the movement of these ions to the surface of the Si substrate where they react to form volatile components that are desorbed [56]. There are two main processes using DRIE for etching Si wafers which are Bosch and Cryogenic process.

The **cryogenic process**, at which the etching is done at temperatures of the range 120-140 degrees below zero Celsius, performs etching and sidewalls passivation simultaneously.

The cryogenic process is understood by studying the chemical reactions between  $\text{SF}_6/\text{O}_2$ . Equations (3-1) and (3-2) illustrate the formation of ion and radical species by electron (e) impact dissociation (3-3). These equations neglect  $\text{S}_x\text{F}_y + \text{O}$  interactions, which act to decrease  $\text{S}_x\text{F}_y$  polymers and increase F (radical) formation assuming the O concentration is not in saturation:



The role of the O primarily seen as passivation of the silicon surface by reacting with the silicon to adsorb on the surface to form an oxide film [57]:



where (s) and (sf) indices denote surface and surface film respectively.

The ions bombardment is responsible of removing the passivation layer from the surface only letting a chance for the fluorine ions to react with Si surface resulting in volatile product (etching Si) as shown in equations (3-4)-(3-6).





Where (ads) and (g) denote adsorbs and gas respectively.

The ions bombardment is essential to provide the directionality and hence controls the anisotropy of the etching. Moreover, the sidewall passivation and etching of the silicon occur simultaneously and must be in balance to maintain profile anisotropy [57].

**Bosch process** is characterized by separating the isotropic etching step (using  $SF_6$ ) with the passivation step (using  $C_4F_8$ ) [2]. These two steps are performed in an alternating method till the etching process is complete. This alternating mechanism causes a scalloping shape of the etched sidewalls as shown in Fig. 3-41.

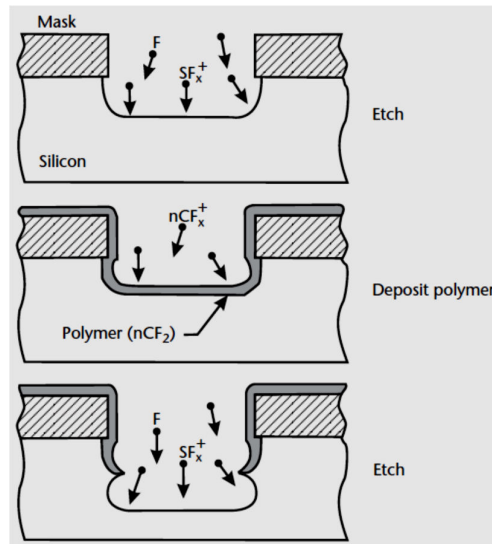


**Figure 3-41: Profile of a DRIE trench using the Bosch process. The process cycles between an etch step using  $SF_6$  gas and a polymer deposition step using  $C_4F_8$ . The polymer protects the sidewalls from etching by the reactive fluorine radicals [2]**

The main advantage of this process is the relatively high etching temperature ( $>20^\circ C$ ) as compared to the cryo process. This allows using photoresist as etching mask for both Si and  $SiO_2$  and at the same time maintain high selectivity and aspect ratio. Therefore, Bosch process is used for etching the intermediate oxide and Si of the handle wafer. The optimized etching recipes are listed in Tables 3-1 and 3-2.

**Table 3-1: Buried Oxide Etching Recipe**

| CF <sub>4</sub><br>(sccm) | O <sub>2</sub><br>(sccm) | ICP<br>(W) | RF<br>(W) | Pressure<br>(mTorr) | Temperature<br>(°C) | He<br>(Torr) | Etch Rate<br>(nm/min) |
|---------------------------|--------------------------|------------|-----------|---------------------|---------------------|--------------|-----------------------|
| 40                        | 5                        | 1000       | 100       | 10                  | 10                  | 10           | 210                   |

**Table 3-2: Bosch Process Used for Etching Si**

|      | C <sub>4</sub> F <sub>8</sub><br>(sccm) | SF <sub>6</sub><br>(sccm) | ICP<br>(W) | RIE<br>(W) | Pressure<br>(mTorr) | Temperature<br>(°C) | He<br>(Torr) | Step<br>Time |
|------|---|---------------------------|------------|------------|---------------------|---------------------|--------------|--------------|
| Dep  | 100                                     | 5                         | 1300       | 5          | 35                  | -15                 | 10           | 7            |
| Etch | 5                                       | 100                       | 1300       | 30         | 30                  | -15                 | 10           | 8            |

### 3.4.2. Photolithography

Photolithography is the process at which the pattern of device is transferred from a master mask to the substrate [2]. This is achieved through three main steps: 1) photoresist coating 2) ultraviolet (UV) exposure 3) Developing. The photoresist is a light sensitive pre-polymer that's coated on the wafer either through spinning or spraying. Then it's exposed to ultraviolet (UV) radiation through a glass mask with pattern made of Cr. As Cr absorbs the UV and glass transfers it, selectivity of photoresist exposure is achieved. After that, the substrate is immersed in a base developer that dissolves the exposed photoresist (in case of positive photoresist). Therefore, the pattern on the master mask is transferred to the photoresist.

There are two processes of coating wafer with photoresist. First method is called spinning. It's done by pouring photoresist on the wafer followed by spinning at high speed to achieve uniform resist distribution. The other method is called spray coating. In the latter case the photoresist is diluted in solvent to reduce its viscosity and sprayed through ultrasonic spray nozzle on the spinning wafer as shown in Fig. 3-42 [58]. This technique has the advantage of conformal coating of the surfaces, edges, and sidewalls of deeply etched microstructures. As it can be inferred from section 3.1 and 3.2, both technologies were used for the realization of the gyroscope version that utilizes vertical suspension system.



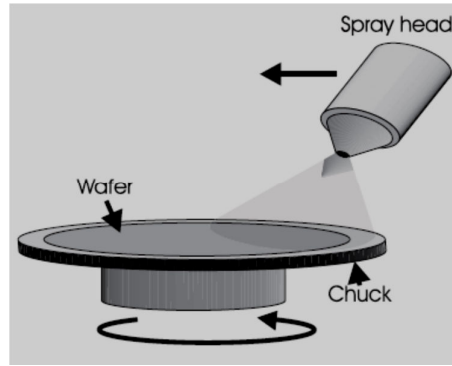


Figure 3-42: Schematic drawing of the spray coating [58]

The optimized process for photolithography by spinning photoresist is the following:

1. Spin HMDS (Hexamethyldisiloxane). It's an adhesion promoter used to enhance photoresist adhesion to Si surface. It's baked at 110 °C for 1 minute then spin resist at 1500/2000 rpm.
2. Pre-bake the photoresist using the following conditions: 110 °C for 2 minutes.
3. Expose photoresist through Suspension mask V6 for 74 seconds.
4. Develop photoresist using AZ 826 MIF developer for ~135 seconds.
5. Hard bake the photoresist at 115 °C for 4 minutes (Optional).

Table 3-3: Optimized photoresist spinning parameters

| Photoresist Type | HMDS Speed-Acceleration             | Spinning Speed-Acceleration         | Pre-back Temp/time | Exposure Time | Developer Type | Developer Time |
|------------------|-------------------------------------|-------------------------------------|--------------------|---------------|----------------|----------------|
| AZ9260           | 1500/2000 rpm- rad/sec <sup>2</sup> | 1500/2000 rpm- rad/sec <sup>2</sup> | 110/2 °C /mins     | 57 sec        | AZ 826 MIF     | 135 sec        |

The optimized process for photolithography by Spray Coating photoresist is the following:

1. Spray coat photoresist using EVG Spray Coater with the parameters listed in Table.
2. Expose the photoresist for 20 seconds.
3. Develop the photoresist using AZ 826 MIF For 80-90 seconds

Table 3-4: Optimized spray coating parameters

| Number of Coating Layer | Dispensing rate | Spinning Speed | Spinning Acceleration    |
|-------------------------|-----------------|----------------|--------------------------|
| 4                       | 8 $\mu$ L       | 80 rpm         | 100 rad/sec <sup>2</sup> |

It's worth noting that the photoresist used in spray coating is a mix of AZ 9260, methyl ethyl ketone (MEK), and AZ EBR (PGMEA) Solvent for dilution with ratio 1:8:1.

### 3.4.3. Chemical Vapor Deposition (CVD)

CVD is most common deposition system in the field of growing different materials in IC technology and micromachining. Moreover, it's used for the synthesis of nanostructures such as carbon nanotubes and of course Nanowires [59].

The simple architecture of the CVD is shown in Fig. 3.43. The main part of the CVD is the deposition chamber where the substrate is placed. Also, and at the top of the chamber, a shower which is used to inlet the different gases used in the process. A heat table for adjusting the substrate temperature is placed beneath it. At last but not least, the chamber connected by powerful pump for vacuuming purposes. The vacuum system is crucial to work as an exit of the unwanted product gases from the deposition chamber during the reaction.

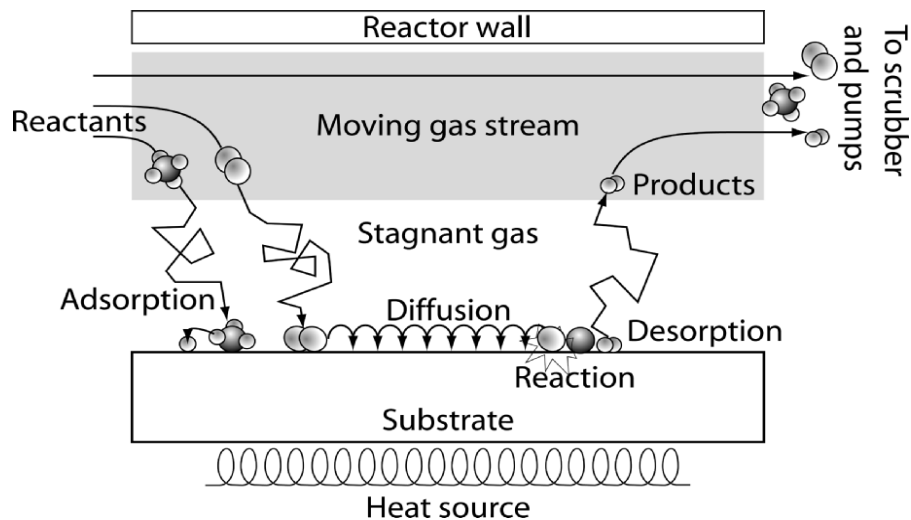


Figure 3-43: Chemical Vapor Deposition working principle diagram [59]

Moreover, in many CVD systems an RF generator is attached to the system for plasma ignition for the purpose of reducing the thermal budget of the deposition process. The term thermal budget refers to the deposition processing temperature.

The CVD is a deposition system in which the deposited materials are realized by the chemical reaction between different gases on or near the surface of the substrate. Certainly the type of the used gases in the process depends mainly on the required material for deposition. The chemical reaction which takes place inside the CVD deposition chamber

requires a special atmosphere. Adjusting this atmosphere implies controlling two parameters inside the CVD chamber: 1) Pressure 2) Temperature [59].

Over the years, CVD proved how crucial it is for realizing micro/nano structures. CVD has been used in different fields of micro and nano structures for depositing thin films of, almost, most of the elements of the periodic table [59]. Also it can be used for compounds. Moreover, the CVD proved that it has much higher potential as a conformal deposition system more than any physical deposition system, such as sputtering or evaporator. Conformal deposition typically refer to the ability of covering the surface and the side walls of the grooves and hills of high aspect ratio in the substrate [59].

However; the CVD process is based on the use of different gases which usually have many safety hazards, some of them might be toxic, corrosive, or explosive. Moreover, the CVD requires higher thermal budget than physical deposition systems [59].

CVD is used during the gyroscope fabrication in the vertical suspension based version to provide good electrical connections between anchors and proof-mass. The resultant SiGe film has a resistivity ranges between 0.6-0.8 m $\Omega$ .cm and the film was realized using the optimized parameters in Table 3-5.

**Table 3-5: Optimized LPCVD SiGe deposition parameters.**

| <b>SiH<sub>4</sub></b><br><b>(sccm)</b> | <b>GeH<sub>4</sub></b><br><b>(sccm)</b> | <b>B<sub>2</sub>H<sub>6</sub></b><br><b>(sccm)</b> | <b>N<sub>2</sub></b><br><b>(sccm)</b> | <b>Pressure</b><br><b>(mTorr)</b> | <b>Temperature</b><br><b>(°C)</b> | <b>RF</b><br><b>Power</b><br><b>(Watt)</b> | <b>Dep.</b><br><b>Time</b><br><b>(mins)</b> |
|---|---|--|---------------------------------------|-----------------------------------|-----------------------------------|--|---|
| 25                                      | 50                                      | 4  | 100                                   | 1500                              | 600                               | 0  | 60  |

### 3.5. Characterization

Micromachined gyroscope has several figures of merits such as sensitivity, resolution, Brownian noise, SNR, and resonance frequency. The latest figure is considered to be the most important parameter as it's considered as a general measure of the gyroscope performance. The resonance frequency is the vibrating frequency at which the mechanical mass-spring-damping system generates a max output displacement for the same input voltage.

The next section provides full gallery of the fabricated versions of the gyroscope (vertical and hybrid suspension system). This is followed by a description of the gyroscope characterization setup for measuring frequency sweeps of the gyroscope drive and sense modes. Resonance frequency, quality factors, and bandwidth are provided for both modes under atmospheric conditions.

### 3.5.1. Fabricated Devices

Scanning Electron Microscope (SEM) is a characterization technique that uses the wavelength associated with beam of electrons to hit micro and nanostructures surfaces and image the surface by sensing the reflected electrons from the surface. SEM images of the realized gyroscope with vertical suspension are shown in Figs 3-44 to Fig. 3-48.

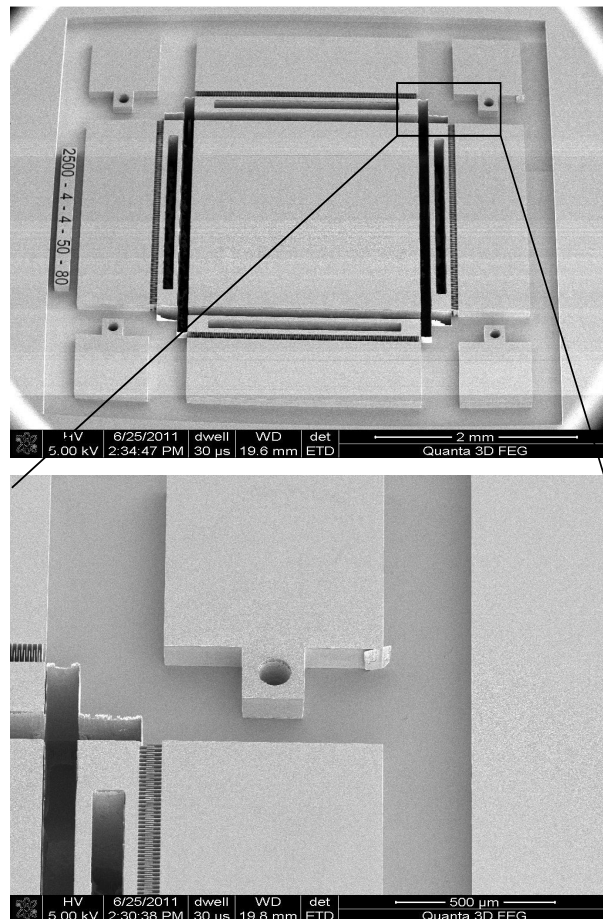
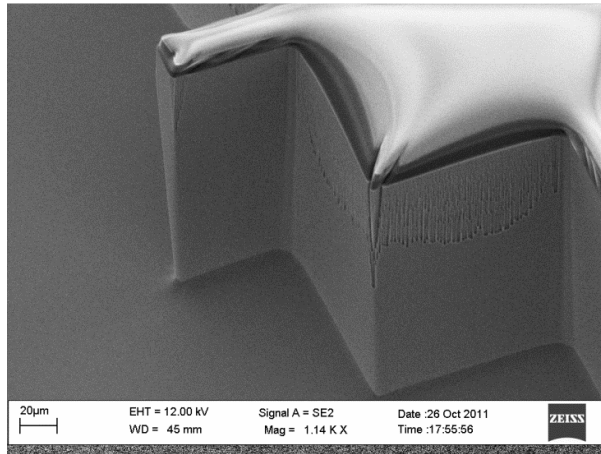
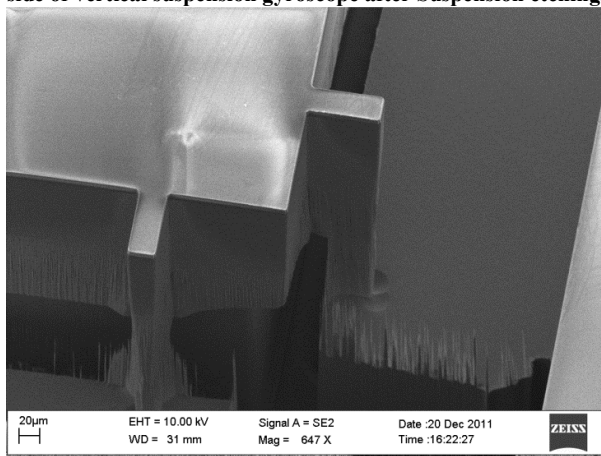


Figure 3-44: SEM of the front-side vertical suspension gyroscope after etching Contacts and Fingers mask



**Figure 3-45: SEM of back-side of vertical suspension gyroscope after Suspension etching. Without etching front-side**



**Figure 3-46: SEM of back-side of vertical beam that's fully defined by etching both Contacts and Suspension masks**

Figs. 3-39 and Fig. 3-40 show the fabricated version of gyroscope with hybrid suspension system.

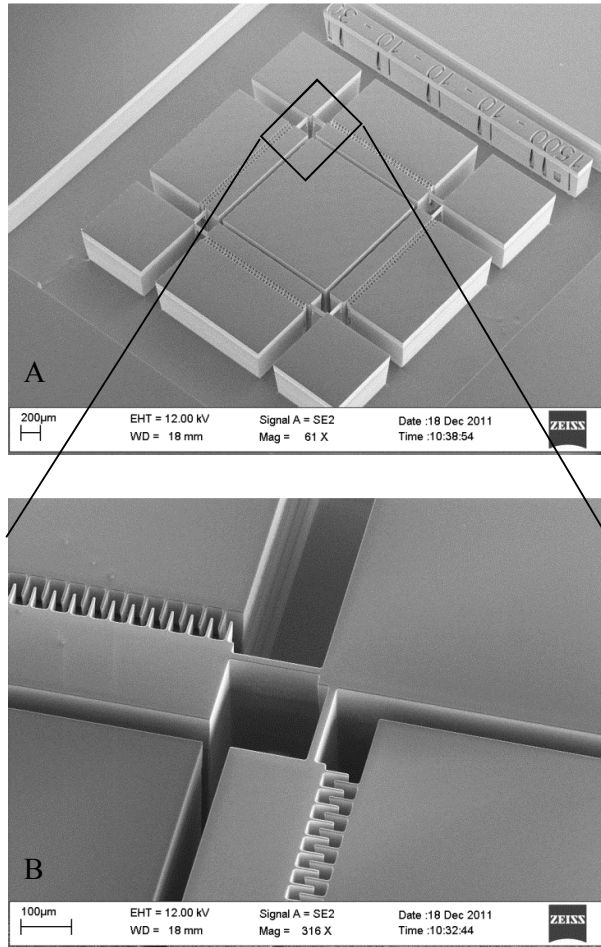


**Figure 3-47: SEM of front-side of the hybrid suspension gyroscope**

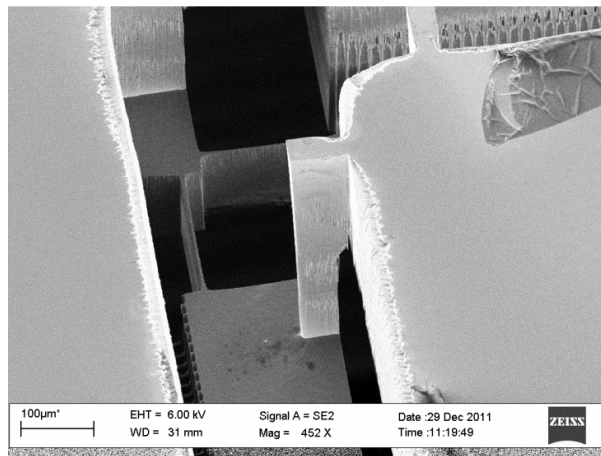


**Figure 3-48: SEM of back-side of hybrid suspension gyroscope**

The next section illustrates the measurement setup and the frequency sweep of the latter device.

### 3.5.2. Measurement Setup

Fig. 3-49 shows the main measurement setup for the resonance frequency characterization. The microprobe station was used to support the gyroscope. This is done by using the vacuum stage to hold the fabricated wafer. Using the four micro probes available on the microprobe station, the input/output connections with the gyroscope can be performed. The Agilent 4395A Network/Spectrum/Impedance Analyzer is used to measure the resonance characteristic of the fabricated gyroscope as well as the quality factor and the bandwidth. Agilent 87512A transmission/reflection test set is used as interface test set between the RF output port and the device under test. LM741 operational amplifier is connected as a transimpedance amplifier to convert the output (current) to voltage signal. The Agilent, 4395A Network/Spectrum analyzer feeds the AC drive signal to the Gyroscope drive via its RF output port. It also receives the Gyro output at its B port. Three Micro-positioners are attached to DC probes for device connections. Three DC power supplies are needed; one for DC voltage polarization and two for the operation of the operational amplifier. Various cables and connectors are used for wiring and connection.

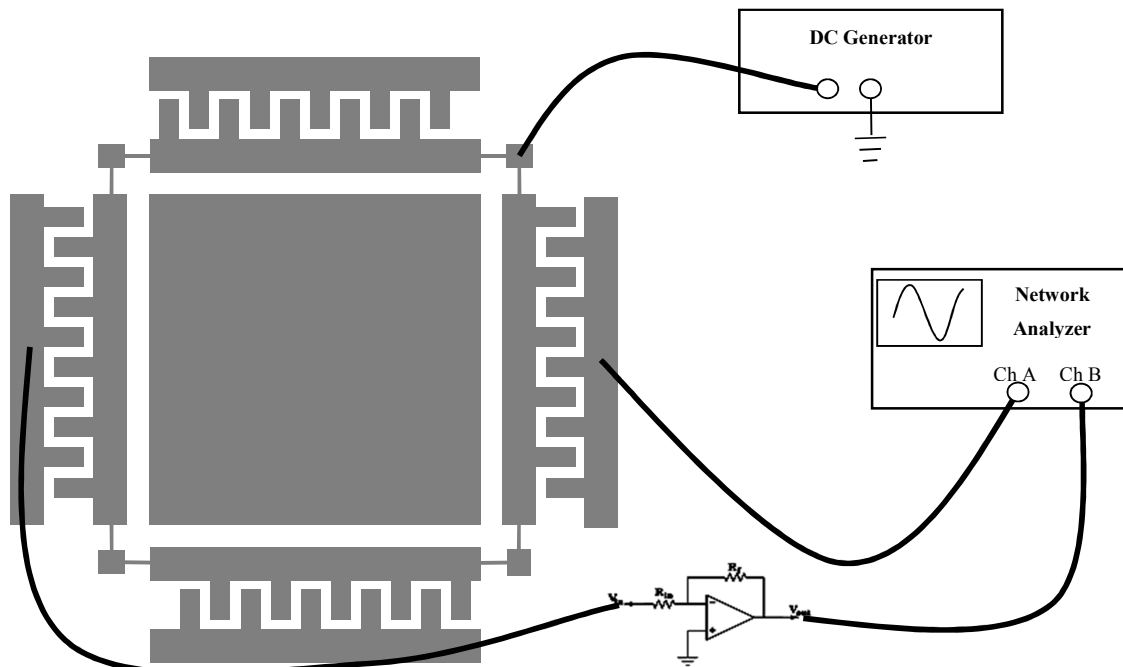


Figure 3-49: Resonance frequency measurement setup

### 3.5.3. Frequency Sweep Results

Figs 3-50 to Fig. 3-51 are the results of the frequency sweep performed to the drive and sense modes of the micromachined gyroscope. The version that was tested is based on the hybrid suspension system with dimensions listed in Table 3-6.

**Table 3-6: Measured gyroscope dimensions in micro-meters**

| Horizontal<br>Suspension<br>(WxLxH) | Vertical<br>Suspension<br>(WxLxH) | Proof Mass<br>(WxL) | Fingers (Width x Gap) |
|-------------------------------------|-----------------------------------|---------------------|-----------------------|
| 10x100x230                          | 50x80x350                         | 1500x1500x600       | 8x8                   |

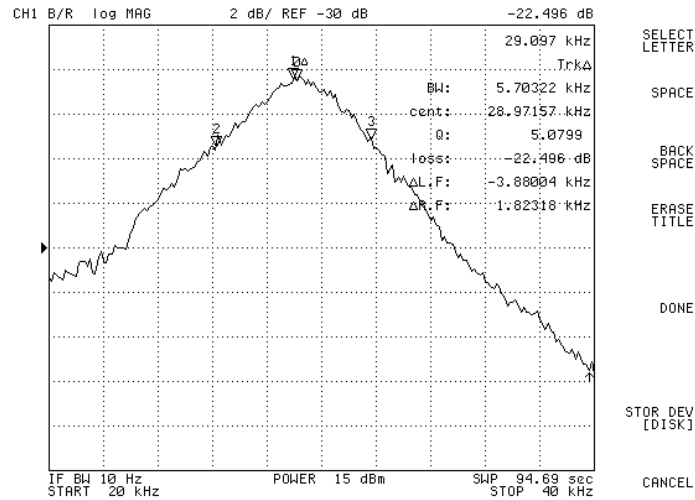


**Figure 3-50: Sense mode frequency response**





Figure 3-51: Drive mode frequency response

By investigating Fig. 3-50 and Fig. 3-51, it is clear that all designed gyroscopes have the approximately matched resonance frequency. Second, the measured quality factors are very small,  $\sim 6$ , in all experiments since the characterization was performed under air pressure conditions. Also, the small length of the vertical beams ( $350\text{ }\mu\text{m}$  instead of  $400\text{ }\mu\text{m}$  in the simulated design) besides the thicker cross-section ( $50\times 80\text{ }\mu\text{m}$  fabricated instead of  $10\times 40\text{ }\mu\text{m}$  designed) clipped the quality factors due to the support and thermoelastic losses. As a result of the very small quality factors, the band width of all designed gyroscopes is very large which approaches a value of 4-6 KHz. A summary of the measured values of the frequency sweeps is listed in Table 3-7. The high resonance frequencies  $\sim 28\text{ KHz}$  (instead of  $4\text{ KHz}$  of the proposed design) for the drive and sense modes are expected due to the reduction of the vertical beam lengths resulting in a stiffer beams and most importantly, because of the use of short in-plane beams in the hybrid suspension system.

Table 3-7: Frequency response results

| Mode  | Quality Factor | Bandwidth (KHz) | Measured Resonance Frequency (KHz) | Simulated Resonance Frequency (KHz) |
|-------|----------------|-----------------|------------------------------------|-------------------------------------|
| Drive | 6.73           | 4.26            | 28.68                              | 29.52                               |
| Sense | 5.08           | 5.7             | 28.97                              | 29.52                               |

## 4. Chapter IV: Devices Packaging

Through the development of different semiconductor applications, it was found that packaging micro/nano systems has a critical role in its implementation. Not to mention that MEMS packaging costs 60-80% of the device full price [60]. In the cases of integrated circuits (IC) packaging was required to provide: 1) circuit protection 2) good electrical interfaces with the outside environment [61]. However; packaging MEMS devices turned out to be more critical than it is in ICs. This is due to the custom nature of the different MEMS devices, which require different needs for their package. Besides the general needs for protecting the device and providing electrical contacts to the outer environment, MEMS devices such as inertial sensors with moving parts requires high vacuum to reduce the damping effects of air, and accordingly, sealing the device hermitically under vacuum is required [62]. Also hermitic sealing under vacuum is necessary in the case of IR bolometers to reduce the thermal connection by convection to the surroundings [60].

Wafer Level Packaging (WLP) is one of the most promising technologies in packaging MEMS devices. This is due to the small size of the package which is as small as the device itself as shown in Fig. 4-1-g, moreover; it's more economical. That's because WLP is characterized by packaging the devices on the wafer (all at once) before the step of wafer dicing [63].

This chapter discusses the packaging of the 3D bulk micromachined gyroscope. A proper design of the package (at which Wafer Level Packaging (WLP) mechanism is utilized) is illustrated with a detailed process flow. After that, the development of Through Silicon Via (TSV) technology is given with more focus on the copper electroplating. Although wafer bonding process was not performed in the lab, the famous mechanisms reported in the literature for Wafer Level Bonding (WLB) are reported and the methodology beyond selection of the optimum technique for our case is explained. The working principle, advantages and disadvantages, from the point of view of packaging the gyroscope intended with this study, of each method are illustrated.

### 4.1. Package Design

There are two main technologies for WLP, which are microencapsulation and wafer bonding. The microencapsulation technique is a mechanism where the MEMS device is coated with a sacrificial layer (e.g.  $\text{SiO}_2$ ) and a package film (e.g. silicon nitride) is deposited on top [64].

After that release holes are defined to allow a particular solvent to dissolve the sacrificial layer leaving the device covered with the package film, yet untouched to each other, leaving the actuators movable. Fig. 4-1 shows a schematic clarifying the flow of the various steps discussed above. After that the release holes are sealed under vacuum with different deposition means such as chemical vapor deposition. Also, the authors in [65] have suggested the use of hydrogen annealing over  $1000^{\circ}\text{C}$  to seal the release holes without adding any new materials. However; the latter technology could cause severe damages to the MEMS device (due to the high process temperature). Hence, the authors in [66] modified the holes sealing technology by using excimer KrF laser. In this approach, only the upper few micrometers of the film are affected with the laser leaving the bulk of the wafer (and MEMS device) at room temperature.

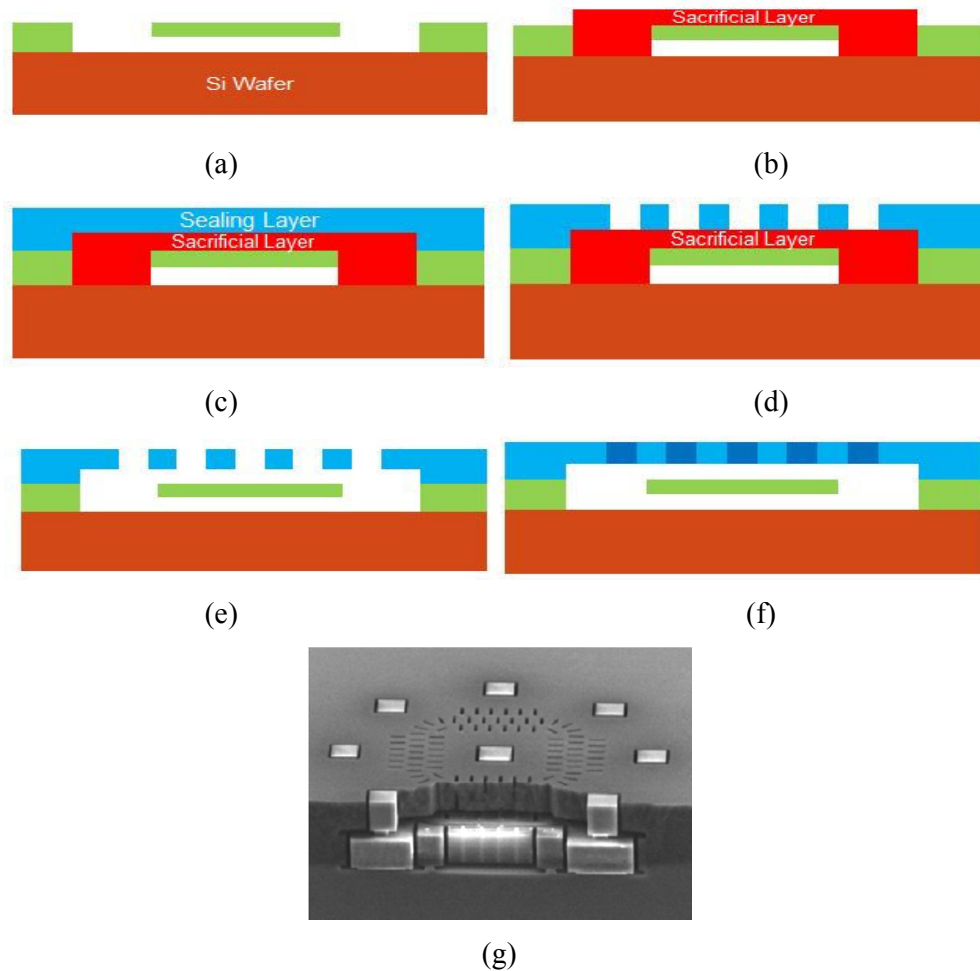


**Figure 4-1: a) Fabricated MEMS device on Si wafer. b) Deposition and patterning of sacrificial layer. c) Deposition of sealing layer. d) Patterning sealing layer to define the release holes. e) Etching the sacrificial layer. f) Sealing the release holes under vacuum conditions. g) SEM taken at step number (e) for a microencapsulated MEMS device [60]**

Although, microencapsulation is used in literature for packaging several MEMS devices [67, 68], it is not suitable for packaging the proposed gyroscope in this thesis. This due to the large thickness of the device layer (100  $\mu\text{m}$ ) while microencapsulation only used, so far, with bulk micromachined devices that are 10  $\mu\text{m}$  thick and for surface micromachined MEMS devices [60]. Therefore, wafer bonding is the optimum solution for achieving wafer level packaging in this study.

The other WLP technology is wafer bonding. In this approach the whole wafer with MEMS devices fabricated on it (device wafer) is bonded to another wafer (cap wafer). The cap wafer has recessed cavities (etched at previous step) aligned to the MEMS devices on the device wafer. This would allow the devices actuation inside the package without the surface of the cap wafer. Wafer bonding technology is recommended to be used for packaging the proposed gyroscope because the whole devices are packaged, simultaneously, followed by dicing step. Instead of dicing the wafer and package each device separately.

Before discussing the design of the package, several requirements should be fulfilled to ensure appropriate operation of the MEMS sensors/actuator; namely:

- 1- Hermetic sealing as micromachined gyroscopes requires vacuum ambient for operation. This environment is crucial to reduce the air damping and increase quality factor of the mass-spring-damping system for performance enhancement.
- 2- Low thermal-budget for avoiding the destruction of the MEMS device
- 3- Package design which should consider the following
  - a. Etched cavities in the cap wafer to provide the required spacing for the actuators movement
  - b. Electrical connections, typically in the case of wafer level packaging (WLP), by Trough Silicon Via (TSV) to connect through bulk of the wafer by Cu electroplating filling.

As the package is intended to be 3D bulk micromachined device, with deep etching from both sides of the wafer, it requires that two cap wafers will be used to cover the device form the top and bottom sides as shown in Fig. 4-2.

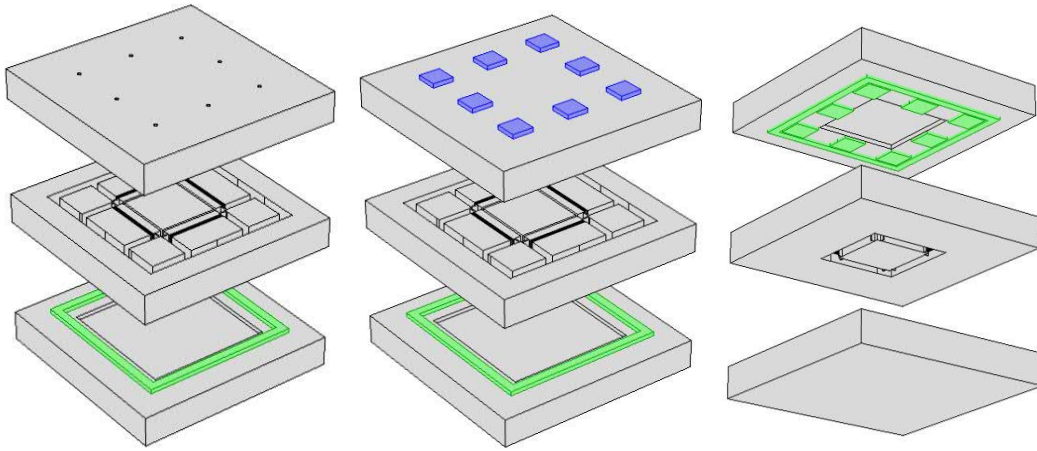


**Figure 4-2: Device wafer with two cap wafers (lower and upper). Green is the adhesive layer, blue is copper pads**

It's worth noting that design proposed Fig. 4-2 TSV (made for electrical connections through cap wafer) are made right above the comb-drive pads instead of routing outside the device area, as typically reported in the literature. The typical procedure is not recommended because the 100  $\mu\text{m}$  depth of the device layer would not allow durable metal lines to be routed outside the device as shown in Fig. 4-3.

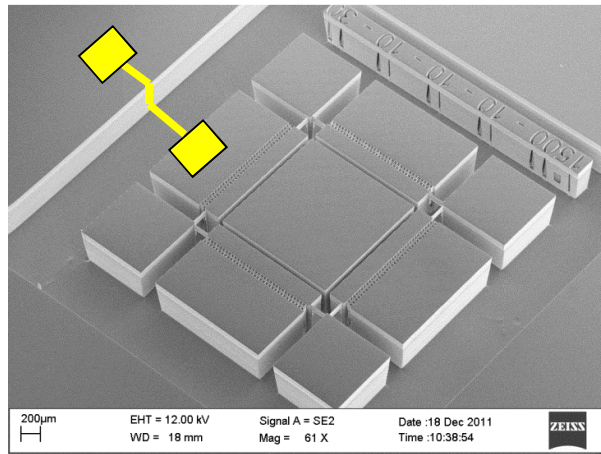


**Figure 4-3: Schematic for metal line route on gyroscope.**

The next two sections discuss the enabling technologies for wafer level packaging (WLP). WLP is mainly composed of two steps. First, the formation of Through Silicon Via (TSV). TSV are considered as metallization but through wafer. It's responsible to transfer the electrical signals from the device to outside the package. Second, wafer bonding which is responsible for capping the device wafer and provide the optimum environment for proper operation.

## 4.2. Through Silicon Via (TSV)

Through silicon via (TSV) are widely utilized these days in the implementation of 3D Integrated Circuits (ICs) [69]. Also, in MEMS field they are widely used in WLP for electrical connections [70]. TSV as shown in (Fig. 4-4-b) is a hole formed (by DRIE) in the cap wafer and filled with metal (typically done with electroplating) to transfer the electrical signal from the MEMS device to the outer environment. The greatest advantage of TSV that it enhances area utilization compared to conventionally used wire bonding. By using TSV, the electrical pads of the MEMS device after packaging are located right above their places on the device while using wire bonding the pads are located on a much farther perimeter, thus consuming more area as shown in Fig.4-4.

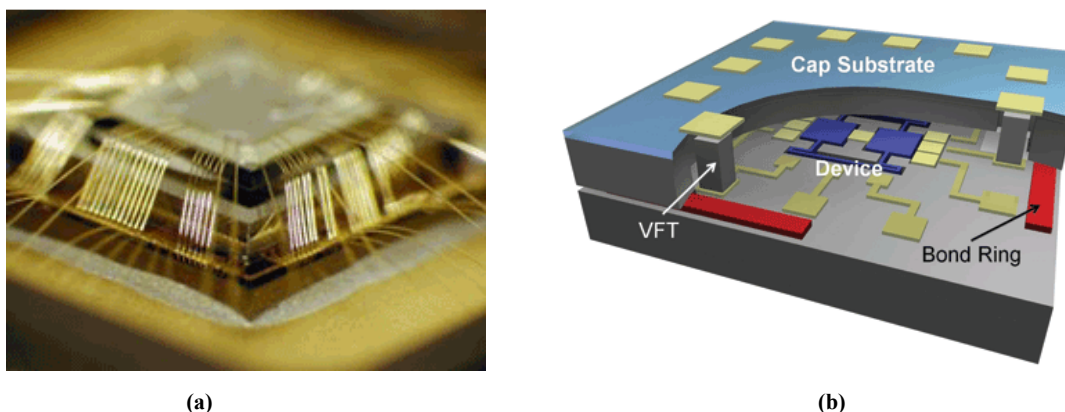


Figure 4-4: a) Conventional packaging using wire bonding [60]. b) Wafer level packaging using TSV [60]

Several facilities are required to perform TSV. DRIE is used to etching the hole in the cap wafer, physical vapor deposition (PVD) for seed layer growth for filling the hole with a metal that's finally achieved by electrodeposition means. The electrodeposition step is the most critical step as several issues are facing filling TSV with metal (typically Cu) such as uniformity of the filling Cu especially with high aspect ratio TSV [71].

Several techniques for manufacturing TSV were reported in literature [69, 70, 72, 73]. Another way of manufacturing TSV without the need of electroplating by using Nickel wires directed to fill the TSV by magnetic field is reported in [71]. It should be mentioned that one of the critical steps in forming TSV is the isolation step to prevent any short-circuit between the different signals. For preventing such issue, thermal oxidation is performed on the cap wafer after etching TSV. This forms a  $\text{SiO}_2$  layer on the TSV sidewalls and hence achieves the required electrical isolation. However, as it's not possible to form this passivation with

the current facilities available at YJSTRC, a high resistivity Si wafers were used as cap wafers to ensure the electrical isolation.

In the next sections, the facilities such as PVD and DRIE, which are crucial for forming TSV, are discussed. After that, a detailed explanation of the electroplating method is provided. Finally, the two setups typically used for filling the TSV by Cu electroplating are studied followed by discussing the results from using each one of them.

#### **4.2.1. Deep Reactive Ion Etching (DRIE)**

The Deep Reactive Ion Etching process is used for etching via through the whole thickness of silicon wafers. The mechanism and physics beyond the DRIE technology are discussed in details in section 4.3 of this thesis.

#### **4.2.2. Physical Vapor Deposition (PVD)**

Physical vapor deposition is a useful technique for depositing thin films of different materials such as metals and alloys on the Si substrates. The general mechanism is mainly based on physically transferring material from a target (made of the required material to be deposited) to the substrate [74]. Based on the mechanism of transferring the material different techniques of PVD are defined.

Another commonly used technique of PVD is called evaporation. In this case the target (source of the deposited material) is heated to the evaporation temperature using several techniques such as filament heating source or by bombarding using electron beams. The metal vapor condenses on the substrate forming the final film. Evaporation in general requires very low pressures ( $10^{-7}$  mbar) for deposition which results in much more pure films than those made with sputtering [75]. Also, evaporation has higher growth rate than sputtering but cannot be used to grow alloys.

##### **4.2.2.1. RF Magnetron Sputtering**

One of the most famous techniques of PVD is the sputtering where high density plasma is used to bombard the source platen (target) to sputter off atoms from its surface. These atoms travel in vacuum chamber till they cover the substrate. Several parameters, such as vacuum pressure, temperature of the substrate, distance between target and substrate affect the growth rate, film stresses, uniformity, and purity [75]. The gas used for generating the plasma plays a critical role in the deposition process as it could be either inert gas which affects physically

on the target (such as Ar) or reactive gas that not only sputter atoms of the target but also reacts with them and affect the final chemical composition of the deposited film (such as O<sub>2</sub>). Sputtering technique is known for its capability of depositing large range of materials such as metals. Moreover, more than one target is used to deposit different compositions of alloys using more than one target [75]. The sputtering has good step coverage as the sidewalls are coated with the film as well as the surfaces. However, sputtering suffers from a low deposition rate (relative to evaporation).

As mentioned earlier, PVD is essential for depositing a seed layer prior to the electroplating process. Therefore, RF magnetron sputtering is used to deposit Cu on Si wafers to serve this purpose.

First of all, it was found on the trials of sputtering Cu on bare Si wafers that the adhesion of Cu with Si is very poor. The Cu film peeled off the substrate during next processing steps such as rinsing in deionized water as shown in Fig. 4-5.

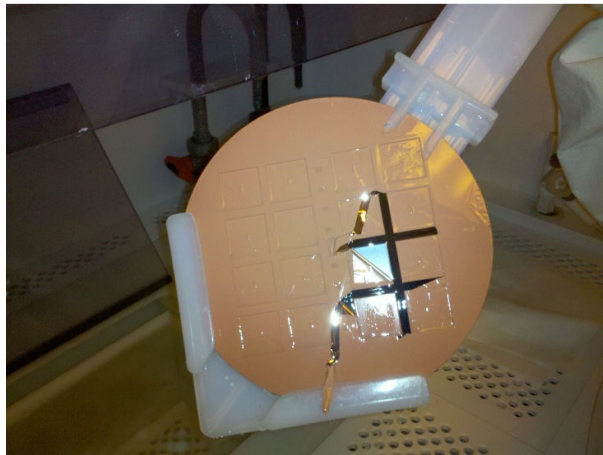


**Figure 4-5: Cu film sputtered on Si substrate directly without any adhesive layers peeled off during rinsing in deionized water.**

Therefore, a 1  $\mu\text{m}$  Ti film was deposited first on the wafer as an adhesion promoter. Also, PECVD SiO<sub>2</sub> improved adhesion purposes between Cu and Si; however, due to its electrical insulating properties it's not proper for our electroplating purposes.

The optimized process used to deposit 1.5  $\mu\text{m}$  thick Cu film on Si wafer is listed in Table 1. Film stresses were determined by measuring the curvature of the wafer before and after depositing the films by using a wafer geometry gauge. Mean stress has been found to be around 250 MPa. Film resistance was measured with four point probe and it was found to be in the order of 1  $\mu\Omega\cdot\text{cm}$ . Also, film uniformity was found to be around 10% across 6 inch wafers.

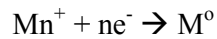


Table 4-1: Optimized Cu sputtering parameters

| RF Power | Substrate Temp | Base Pressure              | Active Gas | Process Pressure          |
|----------|----------------|----------------------------|------------|---------------------------|
| 250 Watt | 400 °C         | $3.75 \times 10^{-4}$ torr | Argon      | $7.5 \times 10^{-3}$ torr |

#### 4.2.3. Electroplating

Electroplating is a process where the metal ions  $Mn^{+}$  (in the electrolyte) are reduced to metal (or the cathode surface) by adding electrons ( $e^{-}$ ) in a cathode reaction carried out with a DC or pulsed power supply [76].



In the electroplating process, the user fixes either the current or the potential with the power supply. Typically, the electroplating processes are carried out at constant current. The current is set on the basis of different variables including type of Cu plating solution, specific pattern design and resist aspect ratio.

The electroplating setup consists of the following four parts that are also shown in Fig. 4-6.

1. The external circuit is a direct current (DC) source connected to the cathode and anode. The voltage between the two electrodes is varied during the process to fix the DC current that ensures constant deposition rate.
2. The negative electrode is the cathode, which is the material to be plated. In this experiment the Si wafer is the cathode.
3. The plating solution itself (electrolyte) is in most cases aqueous and is called the bath. The electrolyte used for Copper deposition is Copper Sulfate.
4. The positive electrode is the anode is usually made of the metal being plated (Copper in that case) but sometimes insoluble electrodes such as Platinum are used.

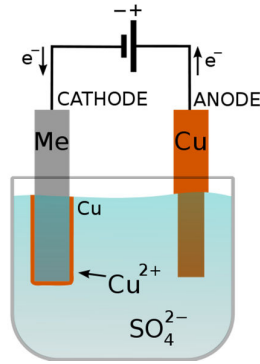


Figure 4-6: Electroplating setup for Cu deposition [60].

The electroplating cannot be processed directly on bare Silicon (Si) wafers because the process is based on an electric current that flows between the anode (the metal target) and the cathode (the Si substrate), and this requires a highly conductive substrate to enable the flow of the current. Thus, the bare semiconductor Si wafers used in the batch fabrication process must be coated with a metal seed layer as a prerequisite for the electroplating deposition.

The electroplating process were performed in IKO3 FIBRotools and optimized by electroplating blanket Si wafers covered with 1 $\mu$ m Ti film deposited using RF Magentron Sputtering facility. The optimized recipe is listed in Table 4-2. The electrolyte used as bath for the electroplating process was a mix of 98% Electrolyte + 1% Carrier + 1% Brightner. Where the electrolyte is a 10% copper sulfate and 20% sulfuric acid. The addition of the sulfuric acid is required to increase the conductivity of the solution. Carriers, also known as suppressors, are usually large molecular weight polyoxy-alkyl type compounds. They are adsorbed at the surface of the cathode and, in concert with chloride ions, suppress the plating rate. Brighteners are small molecular weight sulfur containing compounds that increase the plating reaction by displacing adsorbed carrier on the TSV sidewalls. This mixture works on enhancing the filling uniformity inside the TSV.

Table 4-2: Optimized process for Cu electroplating temperature.

| Current             | Electrolyte         | Cathode/Anode | Anode Reciprocation |
|---------------------|---------------------|---------------|---------------------|
| Density             | temp                | Separation    | Rate                |
| 4 A/cm <sup>2</sup> | Room<br>temperature | 1 mm          | 2 Hz                |

#### 4.2.3.1. Conventional Setup

The conventional setup IKO3 FIBRotools, for filling TSV in Si wafers by Cu electroplating, based on supplying the electrical current on for the cathode (metal seed layer deposited on the wafer) from the front-side of the Si wafer. Therefore, a seed layer as shown in Fig. 4-7 needs to be prepared using physical methods (such as sputtering). The seed layer needs to cover the surface of the frontside of the upper cap wafer (from which the DC electrical current is supplied). Also, the bottom of the trench needs to be coated with the seed layer to ensure that the electroplating step will grow Cu from the bottom up (filling the whole TSV). Moreover, the deposition needs to cover the sidewalls of the TSV to ensure that the electrical current is supplied to the Cu on the bottom of the trench. This conformal deposition (shown in Fig. 4-7-b) is crucial to ensure that the TSV is filled with Cu after deposition (as shown in Fig. 4-8). However, several problems were encountered in this approach.

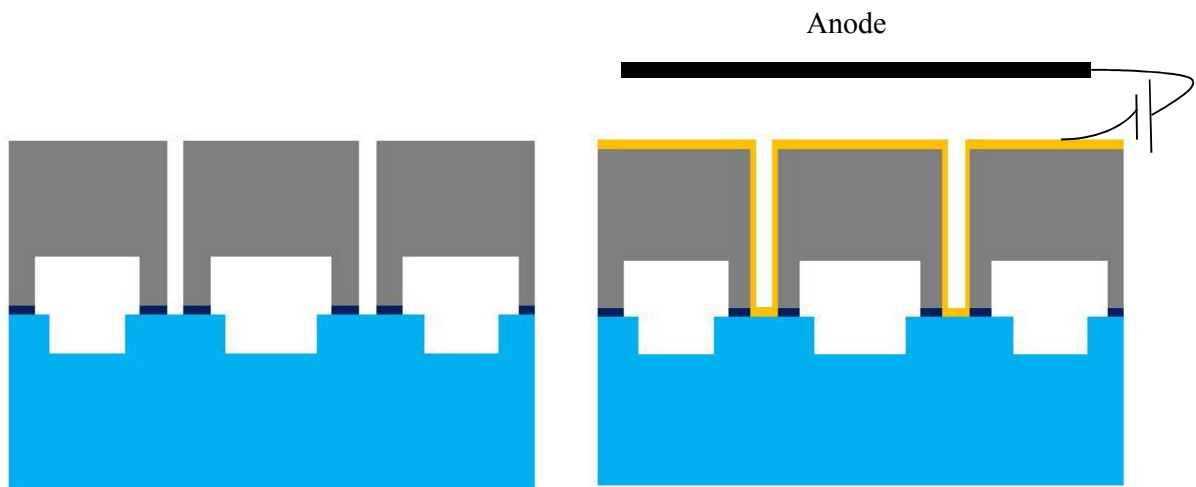


Figure 4-7: a) TSV formed in the cap wafer then wafer bonded to the device wafer. b) Seed layer deposited using PVD then the stack was connected as the cathode in the electroplating setup.

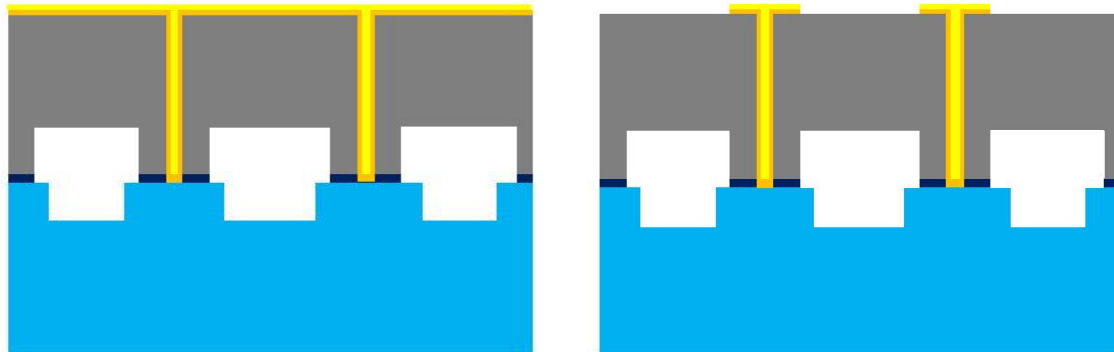
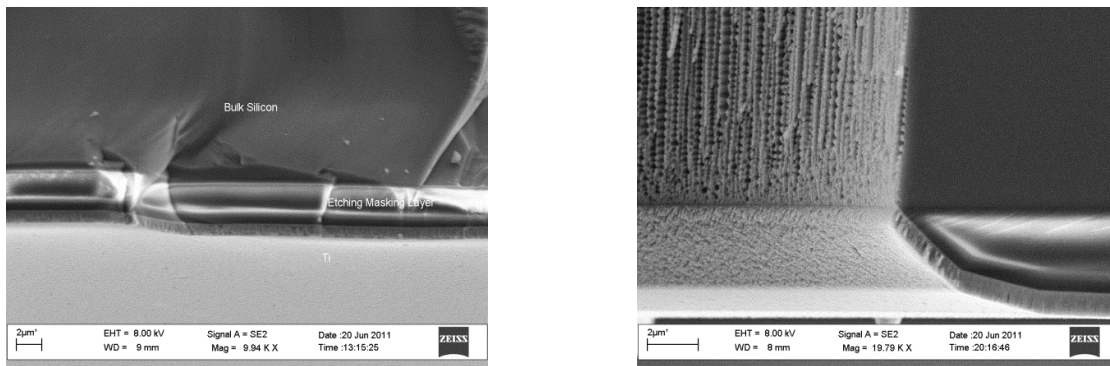
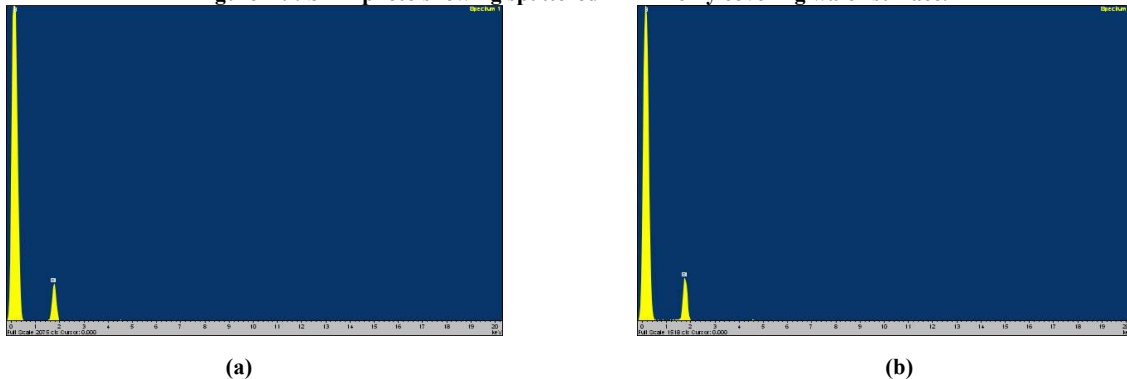


Figure 4-8: a) Cu electroplating. b) Metal pads patterining through wet etching.

As the e-beam evaporation process is known for its bad step coverage, it requires developing a deposition recipe using RF Magnetron Sputtering that guarantees that all the structures and their sidewalls of depth of 700  $\mu\text{m}$  will be coated completely. This mainly requires adjusting the process pressure of the Argon (Ar). The Ar in the sputtering process works as the active gas which is ionized under the generated RF power then the Ar ions bombard the target, which is Cu in this case, and sputter Cu atoms on the substrate. The Ar pressure values were swept from  $10^{-3}$  to  $10^{-1}$  mbar, and it was found that the optimum step coverage is achieved at a pressure of  $10^{-2}$  mbar. However, it was found that only the features with wide spacing etched around it (in range of  $\text{mm}^2$ ) were coated with Cu. On the other hand, small holes areas ( $40 \times 40 \mu\text{m}^2$ ) with aspect ratios (between width and etching depth) down to 10 were not covered as shown in Fig. 4-9. Moreover, energy dispersive X-ray (EDX) scans shows no sign of Ti on the trench bottom and sidewalls as shown in Fig. 4-10.



**Figure 4-9: SEM photo showing sputtered Ti film only covering wafer surface.**



**Figure 4-10: EDX scans showing no sign of Ti on the trench sidewalls (a) and trench bottom (b).**

Hence, due to the absence of a conformal deposition technology (in the lab) for metallic seed layer, the conventional electroplating setup is not useful. A modified setup is introduced in the next section and showed excellent results for filling TSV with Cu using electrodeposition.

#### 4.2.3.2. Modified Setup

Due to the unavailability of metallization conformal deposition system for forming a proper seed layer, the electroplating setup was modified accordingly. First, the seed layer was deposited on the backside of the cap wafer. Then, the TSV were patterned using photolithography techniques and Si etched deep through the wafer using Bosch process in DRIE till the metal seed layer is reached as shown in Fig. 4-11. In this case, the electroplating process can be achieved where the electrodeposited Cu is selectively grown in the TSV only where they are the only areas where the electroplating cell (anode, cathode, and electrolyte) is formed as shown in Fig. 4-12-a. After that metal seed layer is patterned according to application and finally, the cap wafer is bonded to the device wafer as shown in Fig. 4-12-b.

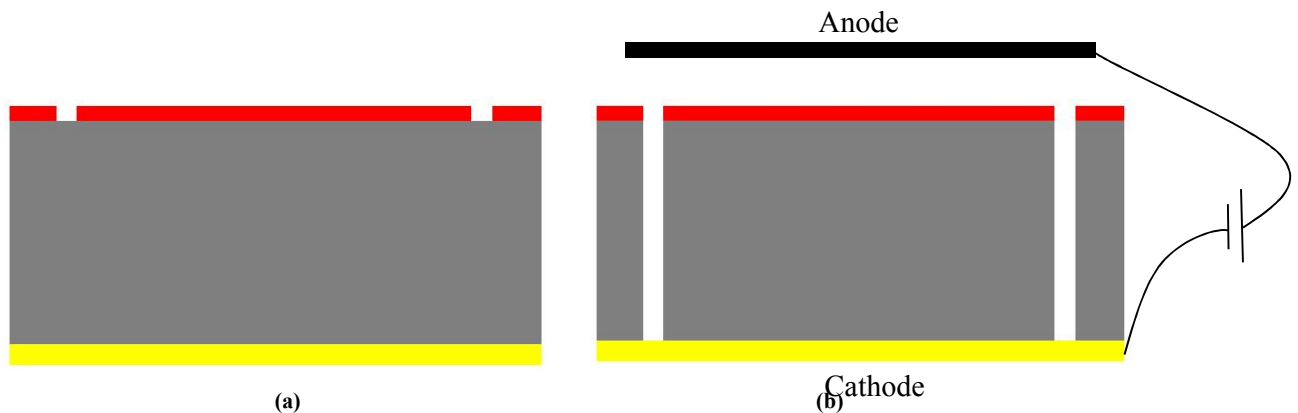


Figure 4-11: a) Printing areas of TSV on high resistivity Si wafer. b) After etching Si wafer, seed layer grown on the backside of the wafer and served as the cathode in the electroplating process

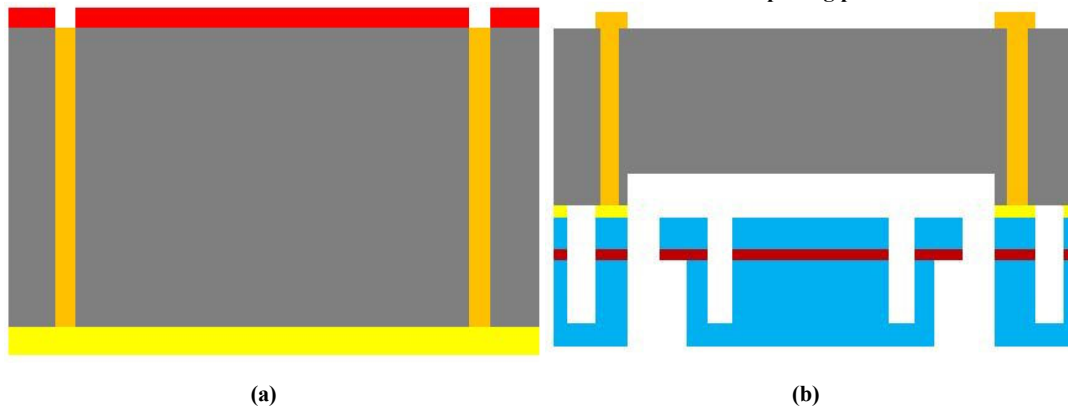
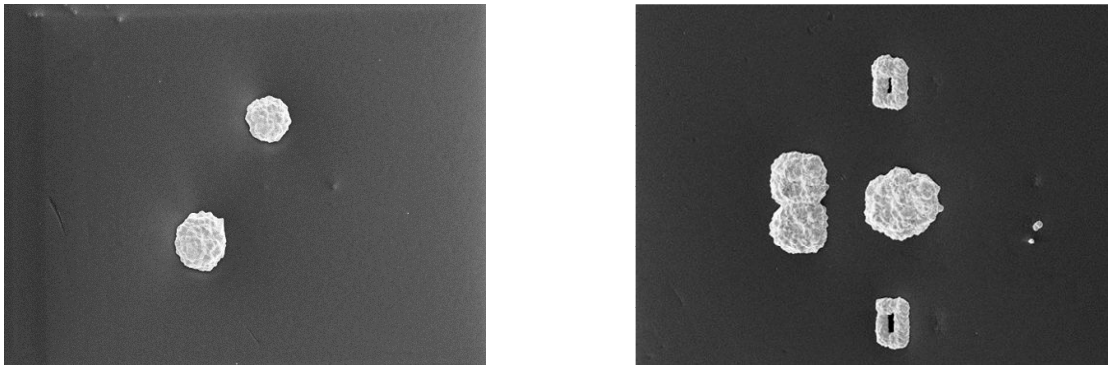


Figure 4-12: a) Electroplating Cu. b) Patterning backside Cu seed layer using wet etching and bond cap and device wafers together.

The SEM photos in Fig. 4-13 show the results of using the modified setup for forming TSV. The TSV had areas of  $40 \times 40 \mu\text{m}$  and they were  $670 \mu\text{m}$  deep (wafer thickness) while the seed layer on the backside is  $10 \text{ nm Ti}$  and  $1.5 \mu\text{m Cu}$ . The Ti and Cu seed layer can be replaced

with gold (Au) film as Au is known for its good adhesion to bare Si besides it serves as the adhesion material in the case of eutectic wafer bonding as it's illustrated in the next section.



**Figure 4-13: TSV filled with Cu after electroplating. It's notable that the electroplating process is selective to TSV other than Si surface.**

It's worth mentioning that the same experiment was performed except that the TSV trench etching did not reach the metal seed layer on the backside and Cu growth was observed. This ensures that the Cu shown in Fig. 4-13 is grown from the seed layer on the backside. Hence, electrical connection is achieved between both sides on the TSV places.

### **4.3. Wafer Bonding**

The previous sections studied the optimum way of packaging the proposed gyroscope by utilizing wafer level packaging and introduced a design of the package. Then illustrated the experiments made for developing Through Silicon Via technology which are used for the electrical connections. After that, the enabling technologies for TSV were studied with more focus on the Cu electroplating process.

In this section the second most important part of the wafer level packaging technology is studied. This part is wafer bonding. The different bonding methodologies (direct, anodic, glass frit, and anodic bonding) are explained with a focus on the pros and cons of each one of them. Based on the latter, the optimum bonding technology for packaging the proposed gyroscope is selected. The four mentioned bonding technologies were selected for study because of their reliable capabilities, reported in literature, for achieving hermetic sealing (air tight) which guarantees vacuum environment for the gyroscope for proper operation. For instance bonding techniques using polymer as an intermediate layers were reported in the literature [77] but not considered in the discussion because they are incapable for achieving

hermetic sealing and generally used for microchannels formation for microfluidics applications.

#### **4.3.1. Direct (Fusion Bonding)**

Bonding without any adhesive material has been very useful technique, typically used, for fabricating Silicon-On-Insulators wafers [60]. The researchers at Toshiba Corporation [78] found that strong bonding occurs when a two clean, mirror-polished silicon wafers are contacted at room temperature after hydrophilic surface formation where hydrogen bonding provides a modest degree of adhesion. Bonding strength, between the silicon surfaces, is raised till the fracture strength of bulk silicon after heating the Si wafers above 1000°C where the fusion process is achieved [74]. Also, it was found that the electrical resistivity at the interface is less than  $10^{-6}$  Ohm/cm<sup>2</sup>. Moreover, if two wafers (one p-type silicon and one n-type silicon) are bonded together, they will form a diode at the interface.

##### **Advantages**

The main advantages of direct bonding is that the cap wafer is made of double sided polished standard Silicon wafer which can be patterned and etched with conventional Deep Reactive Ion Etching processes. Also the direct bonding, as inferred from its name, bonds silicon wafers directly to each other without any additional steps of depositing, and patterning, additional adhesion layer. Moreover, fusion bonding is reported to successfully to be used in bonding between Si-Si, SiO<sub>2</sub>-SiO<sub>2</sub>, and Si-SiO<sub>2</sub> materials.

##### **Problems**

Many drawbacks are associated with the direct bonding technique that excluded it from being used for packaging the gyroscope. First, it needs high temperature that could reach up to 1000°C. Even if this temperature can be achieved with the current facilities, there is risk that it would destroy some structures especially metallization pads. Also, this technique requires very clean environment and is performed at class 10 clean rooms [60]. Moreover, it requires very smooth and clean surfaces for bonding with surface roughness of the order of few hundred angstroms. Such smooth surfaces can only be found with blank wafers (not processes) and hence this technique is generally suitable for fabricating SOI wafers. The authors in [78] mentioned, the absence of clean and smooth surface will likely cause voids in the bonding edge which prevent the hermetic sealing because of the probability of vacuum leaking.

### 4.3.2. Anodic Bonding

Anodic bonding is the other technology where cap wafers are directly bonding on a Si substrate [79]. Glass wafers with a high concentration of sodium ions (for example, Pyrex 7740 of Glass, Corning) is connected as the cathode, during the bonding, while the silicon wafer is the anode as shown in the Fig. 4-14. The two wafers are heated, during contact, to 300-400°C, under a voltage of about 200 to 1000 volts. The applied voltage produces a very high electrostatic force that pulls the silicon and glass in intimate contact. Sodium ions in the glass wafer (the cathode side) diffuse towards the other side of the interface, while the oxygen ions leaves a negative charge which is accumulated at the bonding interface [80]. The available oxygen ions and silicon atoms at the interface forms a strong Si-O bonds, while the electrical current flows between the poles, which show the movement of ions and the completion of this process. By the time electrical current drops to zero, the bonding process is finished.

It is preferred to use cap wafers made of Corning Pyrex 7740 as its thermal expansion coefficient is very close to that of silicon [81]. Also, this type of wafers has very high resistivity ( $\sim 8 \times 10^{10}$  ohm.cm) at room temperature. Therefore, there is no need for any electrical isolation layer (such as  $\text{SiO}_2$ ) to cover TSV sidewalls before electroplating.

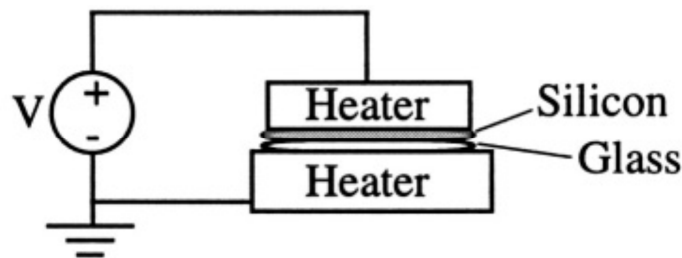


Figure 4-14: Anodic bonding diagram [74].

#### Advantages

The process has several advantages. First of all, it's a direct bonding process with no need for any intermediate adhesion layer between the Si and glass (cap) wafers. Also, the process is done at low temperature (300-500°C) relative to the direct (fusion) bonding. Moreover, it is less susceptible to surface roughness and contamination than direct bonding. That latter characteristic makes it more reliable in packaging heavily processed MEMS applications. Both the substrate and the cap wafer can contain through holes, etched cavities and patterned



metallization. Substrates with SiO<sub>2</sub> or SiN films on their surfaces can be bonded to glass wafers also but requires higher voltages [80].

### **Problems**

One of the problems associated with anodic bonding that the alignment capabilities for anodic bonding using the available AML wafer bonder/aligner. The machine requires that the Glass wafer to have thickness of 0.2-0.3 mm while the standard wafers are around 0.5 and 1 mm [81]. Due to the existence of the cavities and TSV, which requires wafer alignment with resolution of min 100  $\mu$ m, which can be achieved with the naked eye, wafer thinning facility would be required. Otherwise, thinner Pyrex wafers should be bought and used; however, they would be more expensive (not economically preferred). Also, they would be more vulnerable so the waste rate would increase.

Second, and most important, the etching capabilities in Pyrex wafers are limited. Wet etchant can be used but it's isotropic (etch in all directions with same rate) [82]. This will cause a problem when etching TSV for electrical connections. Also, etching through wafer (TSV) requires an etching mask that last for relatively long time. This is due to the fact that Pyrex wafers are etched in hydrofluoric acid (one of the harshest acids) [82]. On the other hand, dry etching using SF<sub>6</sub> was previously reported for etching Pyrex wafers in DRIE [83]. However, it has slow etch rate of 0.6  $\mu$ m/min and not efficient for etching TSV. Laser drilling can etch through Pyrex wafer for electrical interconnections. However; this process is not suitable for batch fabrication because it requires scanning the wafer for etching all the TSV. Moreover, severe cracks were noticed during the process. Sand blasting is a potential successful etching technique for etching Pyrex wafers [84]. However, it has wide etching angle of  $>50^\circ$  which would reduce the features' resolution and consequently increase the package area. Also, the latter facility is not available at YJSTRC lab.

### **4.3.3. Glass Frit Bonding**

The glass frit wafer bonding is utilizing a paste of glass printed on cap and device wafers by screen printing. The bonding process is thermocompressive where the glass frit is softened, by the act of heat, and wet the bonding surfaces due to applied pressure on the wafers [85]. During the cooling process, the glass frit form a strong bond between the two wafers and hermetic sealing is achieved. The typical heating temperature of glass frit bonding is the temperature where paste (e.g. FX-11-036 by Ferro) is softened which is 450°C [86].

## **Advantages**

Glass frit bonding is known to be more robust against surface roughness and contamination (up to 1  $\mu\text{m}$ ). This is due to the wetting process that occurs to the glass during the bonding, which covers all the contamination and rough surfaces. Also, the glass frit process is known for its high yield, which could reach, almost, 100 % [85]. That's why it's preferred for commercialized applications. Moreover, this bonding mechanism provides high bonding force with a relatively low temperature (450°C).

One of the biggest advantages in glass frit bonding that the paste is of thickness that reaches 15  $\mu\text{m}$  which can cross over metal leads for electrical connections without causing any short-circuit between them. Also, glass frit bonding is used for several surfaces such as Si,  $\text{SiO}_2$ ,  $\text{SiN}$ , and Pyrex [87]. Finally, the bonding process is selective as it bonds where the glass frit is located.

## **Problems**

Glass frit paste is deposited and patterned (simultaneously) using technology named screen printing. This process requires fabricating silk mask through which the paste is deposited through it. A logistical problem with using glass frit bonding for packaging, in this study, that the screen-printing facility is not available at YJSRTC labs. In addition, the screen-printing technology has high feature sizes of min  $\sim 150 \mu\text{m}$  [60] which consequently increase the required area of the package.

### **4.3.4. Eutectic Bonding**

#### **Operation Principle**

Eutectic bonding is a mechanism where an intermediate layer used as glue [88]. However, in this case, the glue is not based on glass frit or polymer, but it's a metal [89]. Typically, the adhesive metal used is gold (Au). One of the most notable characteristics of metal alloy is that its melting temperature is less than its original constituents [88]. As shown in Fig. 4-15, the melting point of the Au-Si alloy depends on the concentration of Si. However; there is a certain concentration where the Au-Si alloy has its minimum melting point. This point is called the eutectic point of the alloy. The bonding process is performed at the eutectic temperature of Si-Au alloy. This would melt the interface of between Si wafer surface and Au film surface causing tough adhesion and hermetic bonding.

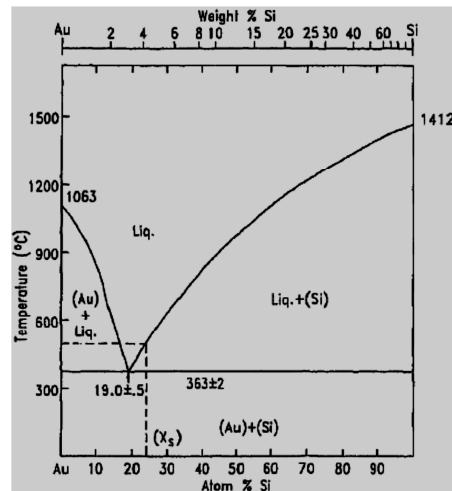


Figure 4-15: Phase diagram for the gold-silicon system [88]

Bonding is performed at the eutectic point of Au-Si and pressure of roughly 100kPa under low pressure (10 mbar).

### Advantages

Although this technology is not as reliable or durable as glass frit bonding, the use of Au as the adhesive material enables better resolution for printing. Also, this gold layer can be used (as demonstrated in the process flow section) as a seed layer for depositing the Cu by electroplating. In addition, the Au has good adhesion to Si surfaces so the adhesion promoter layer (eg. Ti) would not be needed. Moreover, the required facilities for achieving the bonding process are available locally at YJSTRC labs. This is due to the low thermal budget of the process (< 400°C bonding temperature) which can be achieved using the AML wafer bonder/aligner. Besides, the availability of the RF Magnetron Sputtering that can be used for depositing the Au layer.

As it's shown in the previous sections, direct bonding was ousted from the selection because it requires high thermal budget process and not reliable in bonding to processed wafers (with high surface roughness). Also, anodic bonding was not selected because it requires especial Pyrex wafers for bonding which is quite tricky for etching cavities and TSV through it. Glass frit boning is considered one of the best mechanisms for packaging MEMS devices under vacuum for its durability against rough and contaminated surfaces and its high reliability. That's why glass frit bonding is widely recommended for commercialized MEMS applications [85]. However, it requires special facility for depositing glass frit paste on the bonding surfaces which is not available in YJSTRC labs, AUC. Finally, it is concluded that

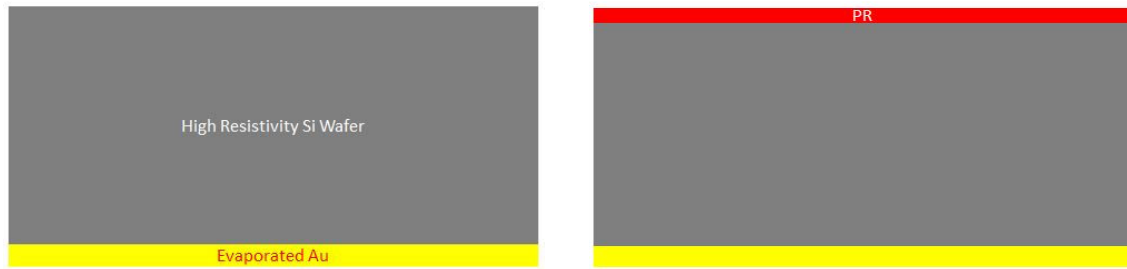
eutectic bonding is the optimum technique. Several reasons (technically and logistically) were explained for verifying the choice.

#### **4.4. Process Flow**

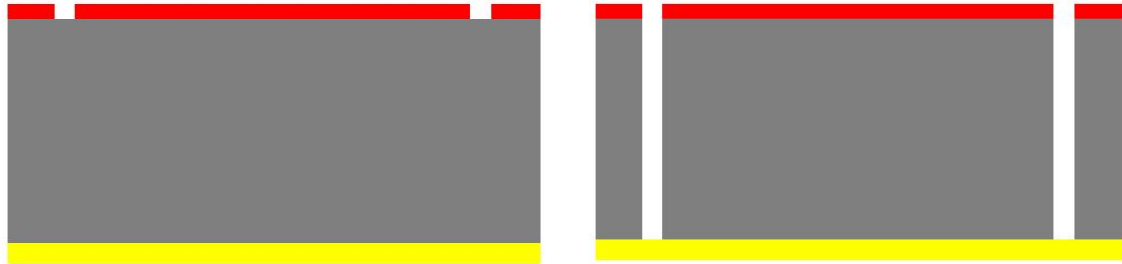
In this section, the development of forming TSV and selection of the optimum wafer bonding technique from literature (taking the available facilities into the consideration) are used in finalizing the detailed process flow for packaging the 3D bulk micromachined gyroscope proposed in this study.

As explained before, the device has areas around the vertical beams where air can be leaked inside the device from both sides of the wafer. Hence, two cap wafers are required to package the device, which are here forth called upper cap wafer (packaging front side of the device wafer) and lower cap wafer (packaging backside of the device wafer).

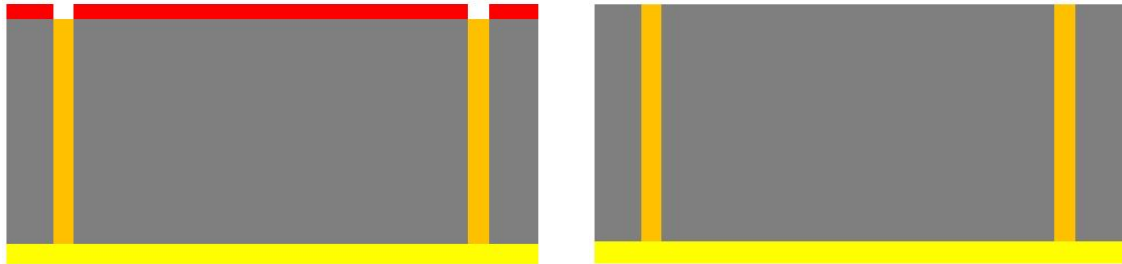
The process begins by first preparing the two cap wafers followed by the bonding process. Cap wafer preparation step includes, etching TSV, filling them with Cu by electroplating, etching backside cavities, add and define the adhesive bond. As shown in Fig. 4-16, the upper cap wafer is selected to be made of high resistivity Si wafer. This choice ensures electrical isolation between the different pads of the device. Also, this wafer needs to be double sided polished as fabrication processing is required on both sides of the wafer. First, Au layer is deposited by e-beam evaporator on one side of the wafer. This layer serves two purposes for the further fabrication steps. First, it's used as a cathode for the Cu electroplating process. Second, it's serves as the adhesive bonding layer for the eutectic bonding. This step should be followed by forming of the TSV. This is done by spinning positive photoresist AZ 9260 on the other side of the wafer and patterning it with TSV mask. After DRIE is performed through Si wafer till reaching the gold layer (Fig. 4-17), Cu electroplating is performed as shown in Fig. 4-18. The latter Cu deposition is selected to the TSV as these are the only areas where the electrolyte in contact with the cathode (Au layer). After that, photoresist is stripped using Acetone followed by sputtering 2  $\mu\text{m}$  Cu film. Then, the latter film is patterned with Metallization Mask and etched (using 5% ammonium persulfate for 6 minutes); hence, the electrical pads are formed as shown in Figs. 4-19 to Fig. 4-20.



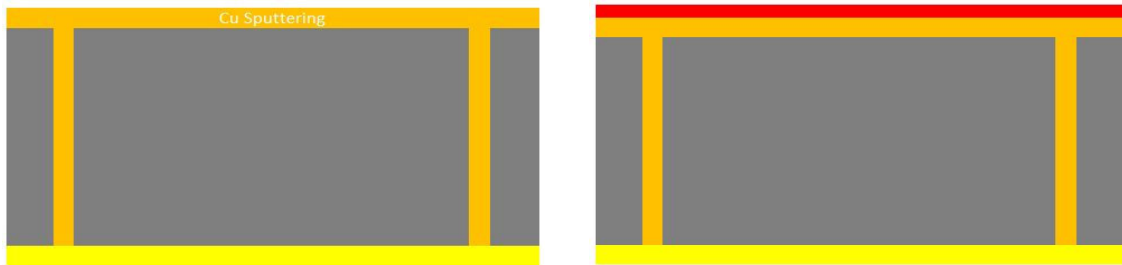
(a) (b)  
Figure 4-16: a) High resistivity double side polished Si wafer with Au evaporated on the backside. b) Spin Photoresist (PR) on the front-side.



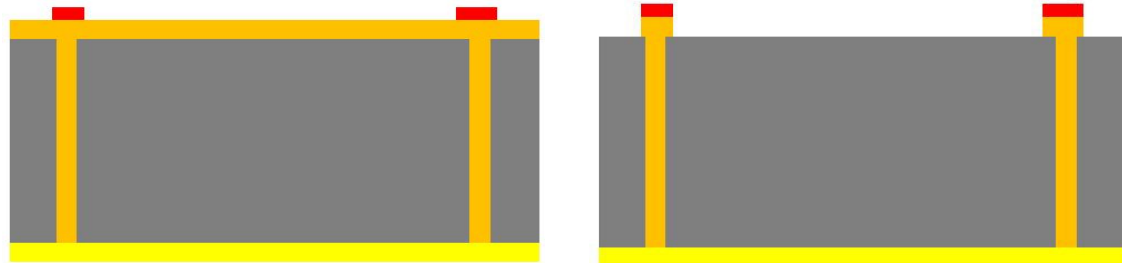
(a) (b)  
Figure 4-17: a) Print TSV mask. b) Si etching through wafer till gold film is reached.



(a) (b)  
Figure 4-18: a) Cu electroplating. b) Strip positive photoresist in Acetone.

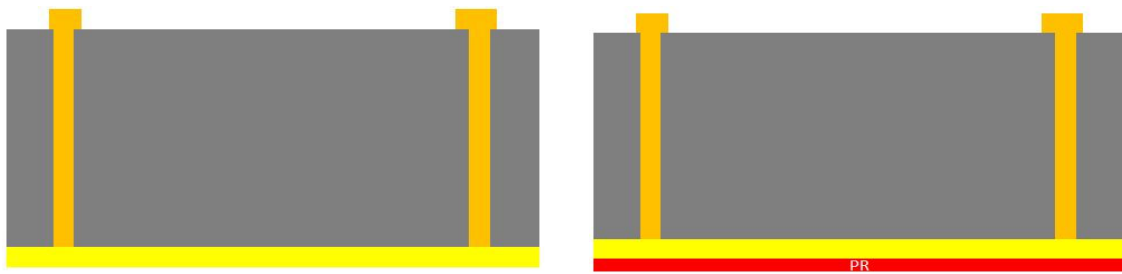


(a) (b)  
Figure 4-19: a) Deposit Cu film using RF Magnetron Sputtering. b) Spin positive photoresist AZ 9260.

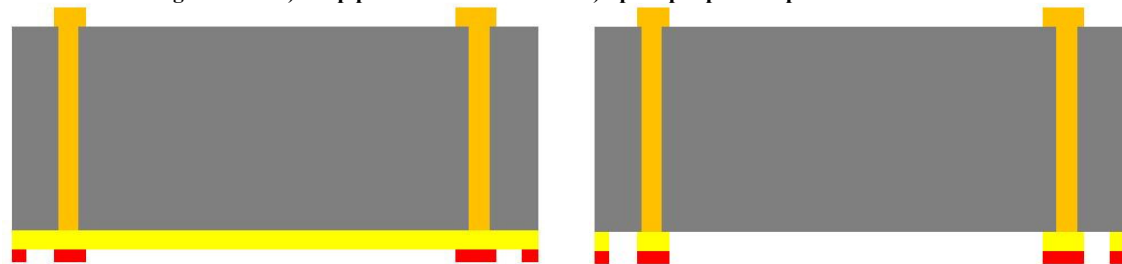


(a) (b)  
Figure 4-20: a) Print Metallization mask. b) Cu wet etching in 5% ammonium persulfate.

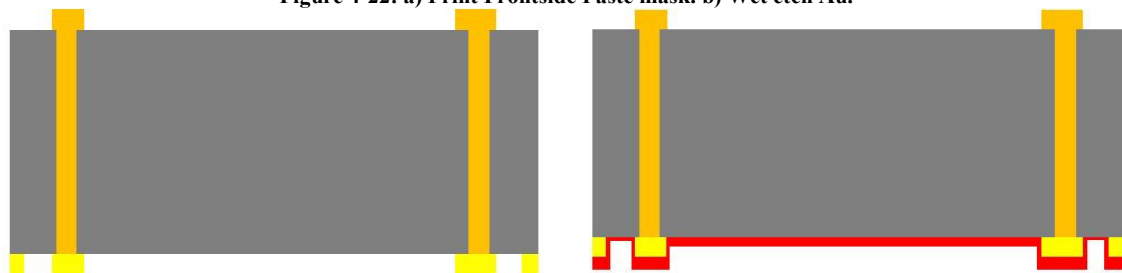
Three goals need to be provided on the backside of the upper cap wafer. First, defining the gold ring required for bonding. Second, isolating the different TSVs from each other is crucial to avoid any short circuit between different output and input signals. At last, a recess to allow the actuation of the gyroscope proof mass. Hence, the backside of the upper cap wafer is coated with positive photoresist AZ 9260 and patterned with Frontside Paste Mask as shown in Figs. 4-21 to Fig. 4-22. This mask performs the first and second goal as the Au film is wet etched afterwards. After that another photoresist coating is processed and Frontside Cavity is printed. The latter step defines the cavity (recess) above the moving parts of the gyroscope. Finally, 50  $\mu\text{m}$  recesses is etched in Si wafer using Bosch process in DRIE as shown in Figs. 4-23 to Fig. 4-24.



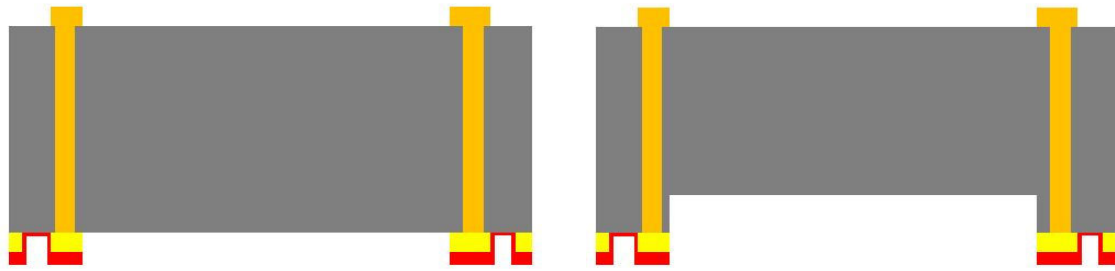
(a) (b)  
Figure 4-21: a) Strip photoresist in Acetone. b) Spin Spin positive photoresist AZ 9260



(a) (b)  
Figure 4-22: a) Print Frontside Paste mask. b) Wet etch Au.

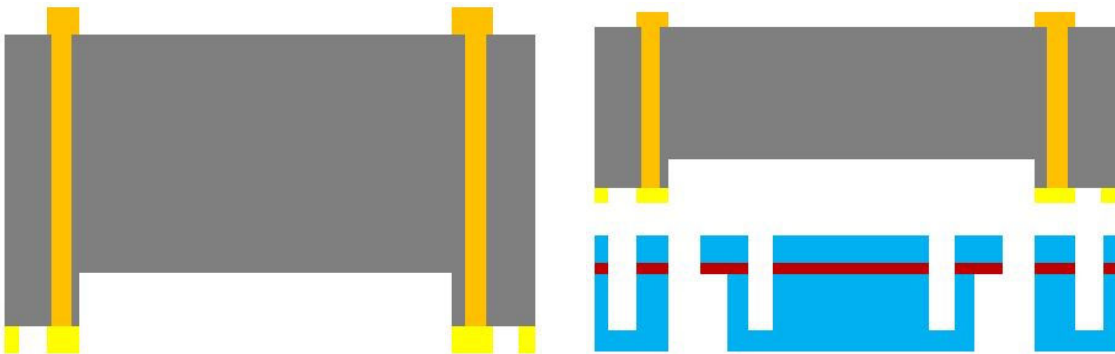


(a) (b)  
Figure 4-23: a) Strip photoresist in Acetone. b) Spin positive photoresist AZ 9260 on the backside.

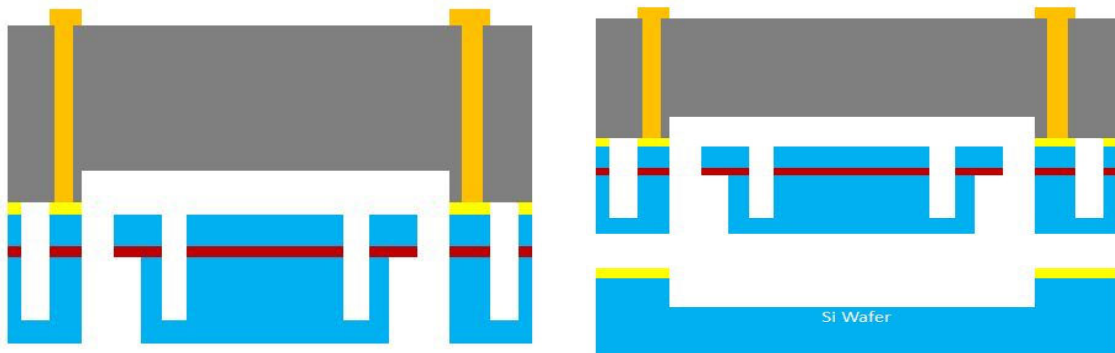


(a) (b)  
Figure 4-24: a) Print Frontside Cavity mask. b) Etch Si in DRIE for 50  $\mu\text{m}$ .

After the upper cap wafer is completely prepared from both point of views: the electrical connections (TSV and electrical pads) and bonding (cavity and Au rings), the upper cap wafer is bonded to front side of the device wafer As shown in Fig. 4-25. On the other hand, and as shown in Fig. 4-26, the lower cap is patterned, using positive photoresist, with Backside Cavity paste mask followed by Au wet etching and 50  $\mu\text{m}$  Si etching using Bosch process at the DRIE. This ensures the presence of a cavity beneath the moving parts of the gyroscope (proof mass).



(a) (b)  
Figure 4-25: a) Strip photoresist in Acetone. b) Align Upper Cap wafer with Device wafer.



(a) (b)  
Figure 4-26: a) Bond two wafers under vacuum conditions. b) Align Lower Cap wafer with Device Wafer.

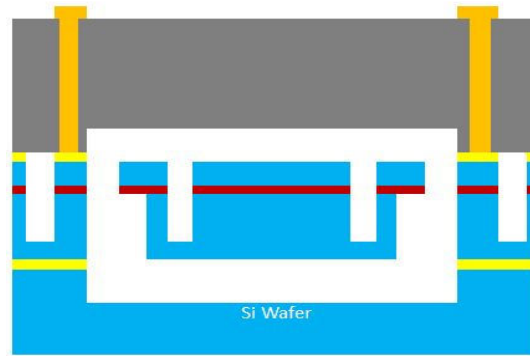


Figure 4-27: Bond stack wafers with Lower Cap wafer under vacuum conditions.

## 4.5. Layout

The different masks needed to realize the package were designed using CleWin 4.0. As illustrated in the process flow earlier, this package design needs two cap wafers (upper and lower cap wafers). The upper cap wafers requires three masks (excluding the metallization mask). These three masks are Through Silicon Via (TSV), Frontside Cavity, and Frontside Paste are shown in Fig. 4-28. The TSV and metallization masks are printed on the front-side of the upper cap wafer while Front side Cavity, and Front side Paste masks are printed on the back-side of the same wafer.

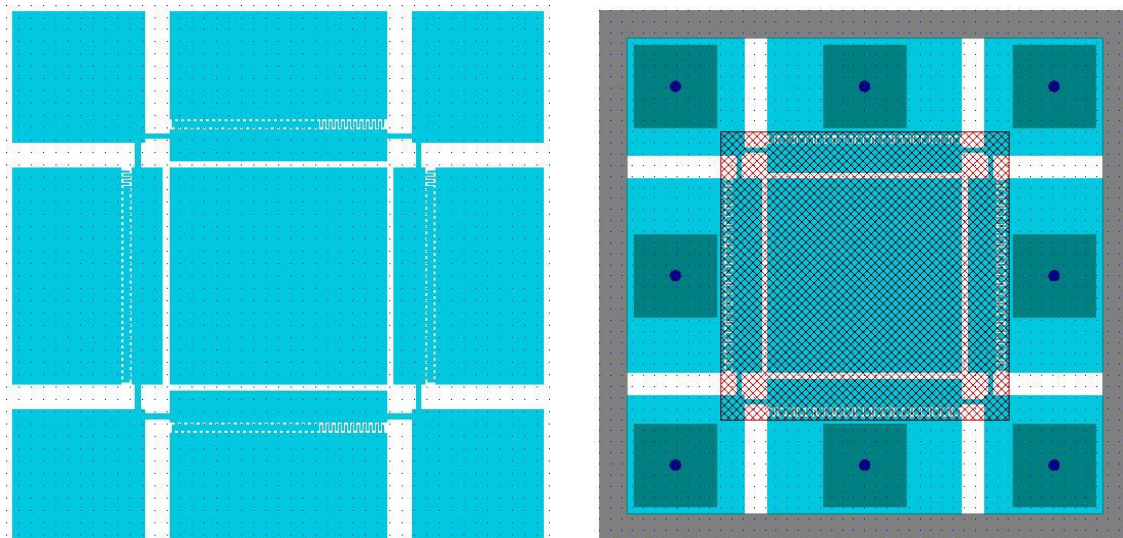
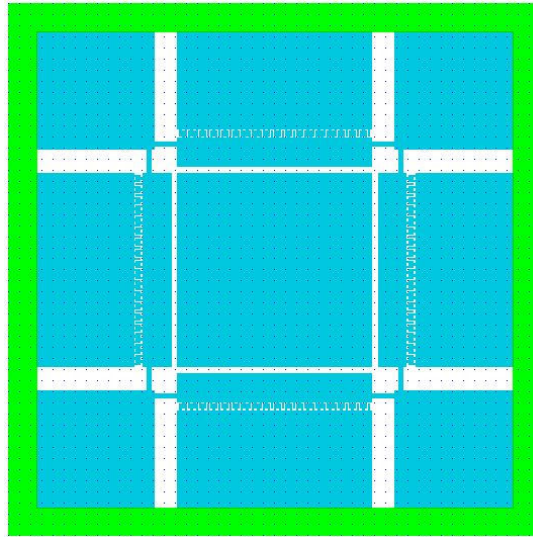


Figure 4-28: Fingers Mask (Blue); Frontside Paste (Grey); Frontside Cavity (Stripes); and TSV (Blue)

On the other hand, the lower cap wafer needs only one mask, shown in Fig. 4-29 called Backside Paste.





**Figure 4-29: Fingers Mask (Blue); Backside Paste (Green).**

In summary, for achieving wafer level packaging for our proposed devices, two main technologies need to be developed which are Through Silicon Via and wafer bonding. The former was successfully developed at the YJ-STRC labs, where  $40 \times 40 \mu\text{m}$  wide via etched through in high resistivity  $700 \mu\text{m}$  thick Si wafers. Then the Cu electroplating process was optimized to fill these pillars on a seed layer of Cu film deposited using e-beam evaporator on the other side of the cap wafer. This would result in selective Cu growth inside via only as shown previously. The wafer bonding technology still needs to be developed. Based on thorough studies, eutectic bonding was selected for bonding the cap wafers to the device wafer. Direct bonding was ousted from the selection because it requires high thermal budget process and not reliable in bonding processed wafers (with high surface roughness). Also, anodic bonding was not recommended because it needs special Pyrex wafers which are quite tricky for etching cavities and TSV through it. Glass Frit bonding was ousted also as it requires special facility for depositing the adhesive paste on the bonded surfaces which is not available in YJSTRC labs, AUC. The development of the eutectic wafer requires optimizing several factors such as the thickness of the gold bond ring, bonding temperature, pressure, and time.

## 5. Chapter V: Summary, Conclusion & Future Work

In this thesis, two novel architectures are proposed for the realization of MEMS gyroscopes. In these two designs, out-of-plane beams are used instead of in-plane beams for the realization of the suspension system. This allows presence of large proof-mass (1.6 mg) with long beams (400-500  $\mu\text{m}$ ). The idea of the utilization of vertical beams for building the suspension system instead of in-plane beams came after the thorough inspection of the various designs in literature. It has been found that most of the designs reported in literature are primarily based on having in-plane suspension or springs, which limit the area fill factor of the proof mass. This in turn reduces the proof mass and results in degraded noise floor or minimum detectable angular rate, output signal sensitivity to input angular rate and, accordingly, scale factor.

Based on the comparison with the best recently reported performance towards inertial grade operation, it is expected that the novel architecture further lowers the dominant Brownian (thermo-mechanical) noise level by more than an order of magnitude (down to  $0.08^\circ/\text{hr}$ ). Moreover, the gyroscope's figure of merit such as output sensitivity ( $150 \text{ mV}/^\circ/\text{s}$ ) is expected to be improved by more than two orders of magnitude. This necessarily results in a signal to noise ratio (SNR), which is up to three orders of magnitude higher (up to  $1,900 \text{ mV}/^\circ/\text{hr}$ ). Furthermore, the novel concept introduced in this work for building MEMS gyroscopes allows reducing the sense parasitic capacitance by an order of magnitude. This in turn reduces the drive mode coupling or quadrature errors in the sensor's output signal. The new approach employing Silicon-on-Insulator (SOI) substrates has very large mass ( $>1.6 \text{ mg}$ ), large sense capacitance ( $>2.2 \text{ pF}$ ), high quality factors ( $>21,000$ ), large drive amplitude ( $\sim 2\text{-}4 \mu\text{m}$ ) and low resonance frequency ( $\sim 3\text{-}4 \text{ KHz}$ ) as well as the consequently suppressed noise floor and reduced support losses for high-performance vacuum operation. The designs are proved to have mechanical decoupling less than 6%. Table 5-1 compares between the performance of the vertical, hybrid, and state of the art gyroscope designs.

**Table 5-1: Comparison between the vertical gyroscope, hybrid gyroscope, and state of the art**

| Performance Measure   | State of the art<br>Design [34]                | Vertical Design  | Hybrid Design  |
|---|--|--|--|
| Overall Gyroscope Area  | 2mm <sup>2</sup>                               | 2 mm <sup>2</sup>  | 2mm <sup>2</sup>   |
| Dimensions of the Proof<br>Mass and Proof Mass Area<br>Fill Factor ( <i>PMAFF</i> )                 | 570*570*40μm <sup>3</sup><br><i>PMAFF</i> ~17% | 1000*1000*700μm <sup>3</sup><br><i>PMAFF</i> ~80%<br>(The effective mass is around <b>53</b> times larger due to area<br>and thickness expansion inherent with the novel gyroscope<br>architecture)                      |  |
| Proof Mass ( <i>M<sub>e</sub></i> )   | 0.03mg   | 1.6mg (two orders of magnitude larger)   |  |
| Resonance Frequency ( <i>F<sub>r</sub></i> )<br>for the <b>SAME</b> Stiffness<br>and Support Losses | 17.4KHz  | 3.1 KHz  | 4.9 KHz  |
| Quality Factors for Drive<br>and Sense Modes ( <i>Q<sub>d</sub></i> and<br><i>Q<sub>s</sub></i> )   | 81,000 and 64,000                              | 21,000<br>The relative small aspect ratio of the vertical beams (4:1)<br>limited the quality factor due to the spring losses.<br>With advanced etching technology, this aspect ratio can<br>reach (1:10) and Q = 340,000 |  |
| Max drive Amplitude for<br>the <b>SAME</b> Voltage  | 3 μm   | 4 μm   | 0.6 μm   |
| Sense Amplitude   | 3 nm   | 150 nm   | 115 nm   |
| Mechanical Noise<br>Equivalent Angular Rate<br>(for the same displacement)                          | 0.3 °/hr                                       | 0.08 °/hr  |  |
| Drive and Sense<br>Capacitances ( <i>C<sub>d</sub></i> and <i>C<sub>s</sub></i> )                   | 0.16pF   | 2.2pF (The capacitance is increased only due to improving<br>the <i>PMAFF</i> , as the active (or electrical) thickness is the<br><b>SAME</b> and equals 40 μm   |  |
| Parasitic or Coupling<br>Sustaining Area for the<br><b>SAME</b> SOI oxide<br>thickness              | 100*570μm <sup>2</sup>                         | 100*100μm <sup>2</sup> (The parasitic<br>Capacitance is then reduced<br>by a factor of 5.7 as a result<br>of the suggested support for<br>the fixed combs)   | The handle wafer is<br>potential less, and<br>therefore, the parasitic<br>capacitance is nearly zero |
| Electrical Output<br>Sensitivity ( <i>S<sub>e</sub></i> )   | 1.25mV/°/s                                     | 150 mV/°/s   | 115 mV/°/s   |
| Signal to Noise Ratio<br>( <i>SNR</i> )   | 4.17mV/ °/hr                                   | 1,875mV/ °/hr (The SNR is<br>improved by <b>three orders</b><br><b>of magnitude</b> )  | 1,437mV/ °/hr (The SNR is<br>improved by <b>three orders</b><br><b>of magnitude</b> )                |

As it's shown in the previous table, the utilization of a full set of vertical beams in the vertical suspension architecture resulted in an increase of one order of magnitude in the drive/sense capacitances and area fill factor while the proof-mass increased with two orders of magnitude. The long, flexible, beams and large proof-mass contributed in the reduction of the

resonance frequency and, consequently, the mechanical theoretical noise by one order of magnitude. Moreover, the output sensitivity of the gyroscope was increased by two orders of magnitude. Total SNR is enhanced by three orders of magnitude.

On the other hand, the hybrid suspension gyroscope nearly eliminated the parasitic capacitances between the drive/sense and the proof-mass. This would contribute significantly to eliminating any existent mechanical coupling using the differential sensing scheme discussed in section 2.2.1. In addition, the fabrication process flow of this architecture is much easier and much cheaper (two masks instead of four in the vertical suspension gyroscope case). It's also worth mentioning that this architecture did not affect the proof-mass area fill factor, capacitance, or the quality factor (keeping the mechanical noise equivalent rotation the same as at the vertical suspension architecture. However, these advantages did not come priceless. The stiffer horizontal beams used caused an increase of the resonance frequency from 3.1 KHz to 4.9 KHz. Hence, slight decline in the output sensitivity and SNR. Nonetheless, the hybrid suspension architecture is considered to be fine trade-off between the fabrication simplicity (low cost) and the high performance (of the vertical suspension design).

The numerical analysis built on Matlab/Simulink platform model the nonlinear behavioral of the electrostatic driven Comb-Drive which is used in the drive and sense modes. This model allows us to expect the tuning capability of the gyroscopes to match the sense and drive modes resonance frequencies during measurement.

It can be concluded from the discussions presented, in chapter 3, and the illustration of the fabrication process for both architectures that the hybrid suspension design is much easier in fabrication, and consequently, cheaper. Fabrication challenges such as selection of the masking material, etching profile optimization, notching effect, and the maximum achievable etching depth are presented in detail. The optimization of these parameters resulted in achieving etching process that forms vertical beams with cross-sections  $50 \times 80 \mu\text{m}$  and lengths up to  $350 \mu\text{m}$  (cf. 5-1).

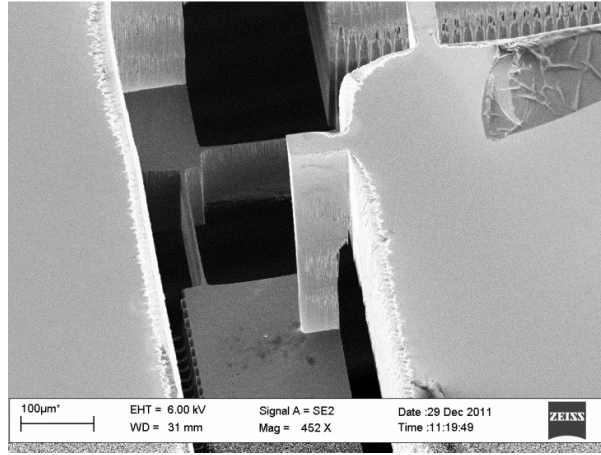


Figure 5-1: SEM of back-side of hybrid suspension gyroscope

By investigating the measured frequency response of the mass-spring-damping system of the gyroscope drive and sense modes, it is clear that all designed gyroscopes have the approximately matched resonance frequency. Second, the measured quality factors are very small,  $\sim 6$ , in all experiments since the characterization was performed under air pressure conditions. Also, the small length of the vertical beams ( $350 \mu\text{m}$  instead of  $400 \mu\text{m}$  in the simulated design) besides the thicker cross-section ( $50 \times 80 \mu\text{m}$  fabricated instead of  $10 \times 40 \mu\text{m}$  designed) clipped the quality factors due to the support and thermoelastic losses. As a result of the very small quality factors, the band width of all designed gyroscopes is very large which approaches a value of 4-6 KHz. The high resonance frequencies  $\sim 28 \text{ KHz}$  (instead of 4.9 KHz of the proposed design) for the drive and sense modes are expected due to the reduction of the vertical beam lengths resulting in stiffer beams (cf. Fig. 5-2).

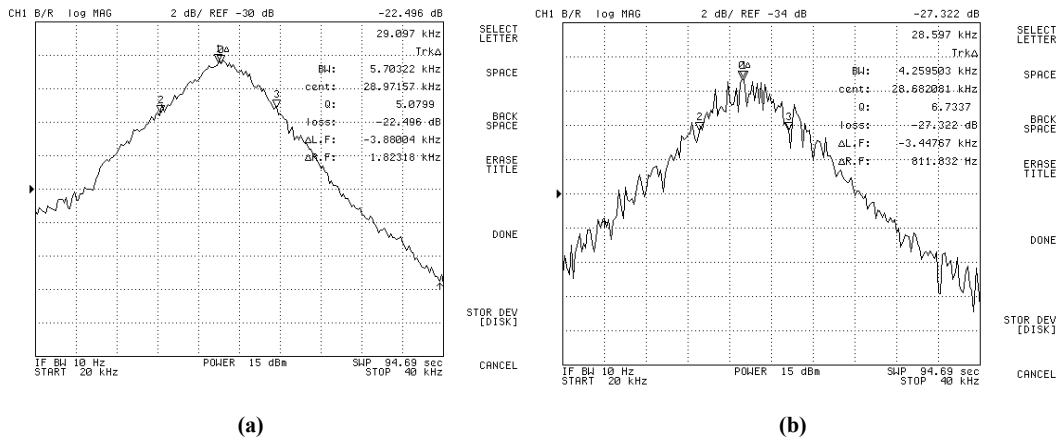
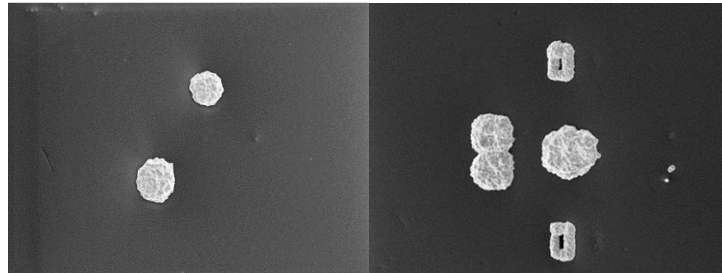


Figure 5-2: Measured frequency response: a) Sense mode. b) Drive mode

A proper design of the package (at which Wafer Level Packaging (WLP) mechanism is utilized) is illustrated with a detailed process flow. This design required developing two complementary technologies: Through Silicon Via (TSV) and Wafer Bonding. The TSV are pillars made of Cu used to transfer the electrical signal outside the cap wafer. An anisotropic etching process for around 700 $\mu\text{m}$  for via with cross-section of 40x40  $\mu\text{m}$  was developed using the Deep Reactive Ion Etching (DRIE). These TSVs were successfully filled by Copper through electroplating process (cf. Fig. 5-3).



**Figure 5-3: TSV after Cu filling by electroplating process**

Although, the wafer bonding process was not performed in the lab, the famous mechanisms reported in the literature (direct, anodic, glass frit, and anodic bonding) are studied with a focus on the pros and cons of each one of them (for our case study). Based on the latter, the optimum bonding technology for packaging the proposed gyroscope is selected. The four mentioned bonding technologies were selected for study because of their reliable capability, reported in the literature, on achieving hermetic sealing (air tight) which guarantees vacuum environment for the gyroscope for proper operation.

Based on this study, direct bonding was ousted from the selection because it requires high thermal budget process and not reliable in bonding to processed wafers (with high surface roughness). Also, anodic bonding was not selected because it requires especial pyrex wafers for bonding which is quite tricky for etching cavities and TSV through it. Glass frit boning is considered one of the best mechanisms for packaging MEMS devices under vacuum for its durability against rough and contaminated surfaces and its high reliability. That's why glass frit bonding is widely recommended for commercialized MEMS applications. However, it requires especially facility for depositing glass frit paste on the bonding surfaces which is not available in YJSTRC labs, AUC. Finally, it is concluded that eutectic bonding is the optimum technique. Several reasons (technically and logistically) were explained in chapter 4 for verifying the choice.

## 5.1. Conclusion

Novel architecture was presented for the realization of MEMS gyroscopes. This architecture causes an evolution in the MEMS industry as follows:

- Out-of-plane beams are used instead of in-plane beams for the realization of the suspension system
- Using the out-of-plane suspension system, large proof-mass (weights 1.6mg) can be realized with long beams (400-500  $\mu\text{m}$ ) in total area for the device of 2 mm<sup>2</sup>.
- The gyroscope's output sensitivity increased by two orders of magnitude (150 mV/ $^{\circ}$ /s)
- Thermo-mechanical noise of the device was reduced by one order of magnitude (down to 0.08 $^{\circ}$ /hr)
- Signal to Noise Ratio (SNR) is enhanced by three orders of magnitude (1,900mV/ $^{\circ}$ /hr).
- This novel architecture results in an evolution in the MEMS vibratory gyroscopes industry because it allows the fabrication of inertial grade gyroscope using standard micromachining facilities.
- MEMS gyroscopes can compete the Ring Laser Gyroscopes in aerospace applications.

Although, the proposed design can be fabricated using standard micromachining facilities, vertical suspension gyroscope fabrication process flow is relatively sophisticated. Therefore, hybrid suspension design was proposed to ease the fabrication process. The new design offered several advantages:

- The proof mass is directly conducted to anchors through in-plane beams.
- The need for Contact mask etching and SiGe deposition was overruled in this design.
- Hybrid suspension architecture needs only two masks for fabrication instead of four for the original architecture
- The new design reduces parasitic capacitance drastically as it removes the potential off the handle wafer.
- Performance was slightly degraded due to the use of stiffer in-plane beams while keeping PMAFF fixed. However, it still operates in the inertial grade class.

The hybrid suspension gyroscope was fabricated. The drive and sense modes resonance frequencies (of  $\sim 28$  KHz) were measured using probe station and network analyzer. This (for

the first time) proves the concept of realizing out-of-plane mass spring damping system using standard micromachining technology.

Spring softening and hardening phenomena are studied to model the comb-drive nonlinearity.

The latter study allows the prediction of the gyroscope frequency tuning capability.

Wafer level packaging (WLP) was selected for sealing proposed designs under vacuum for the following reasons:

- It is favored recently in industry and literature because it allows packaging all the devices on the wafer simultaneously before dicing.
- It increases the packaging density, hence, reduces device cost.

WLP requires the development two technologies: TSV and wafer bonding. TSV technology was developed for transferring electrical signals from device wafer to the drive/sense circuits through the cap wafer. Holes of 40x40  $\mu\text{m}$  were etched (using DRIE) through the wafer of 700  $\mu\text{m}$  thickness and filled with Cu by electroplating.



### 5.3. Future Work

Regarding the gyroscopes designs, several ideas are still open for investigation. For example, replacing the in-plane simple beams, in the hybrid suspension gyroscope, with folded ones and study its effect on the reducing the spring hardening. This would allow higher drive displacement and enhance the devices performance. Also, replacing the simple vertical beam with crab leg would help reaching the same result. However, the length of the bended part of the crab leg beam needs to be optimized to avoid any relapse in the coupling between the drive and sense modes.

Concerning the fabrication, the fabrication process at YJ-STRC needs to be more optimized so that the etching aspect ratio reaches the world standards for Bosch process (up to 1:50). This would allow the formation of smaller cross-section for the vertical beams that could reaches dimensions of  $10 \times 40 \mu\text{m}$ . Also, the max vertical etching depth needs to increased so vertical beams lengths reaches depths of  $400\text{-}500 \mu\text{m}$  instead of max limit less than  $350 \mu\text{m}$ . Moreover, the enhancement of the etching aspect ratio would reduce the gap between the comb-drive fingers from currently  $6 \mu\text{m}$  to  $2 \mu\text{m}$  as designed.

To the regard of the characterization setup, it needs to be built inside a vacuum chamber to reach the simulated quality factors. Also, a measurement platform that includes a rate table is necessary to verify not only the mechanical operation of the mass-spring-damping system of the drive/sense modes, but also, verify that the architecture operates as gyroscope with the simulated performance. Metallization pads are essential to be formed on the fabricated gyroscopes to be bonded through wires to the rate table electrical ports.

Finally, the wafer bonding technology needs to be developed. Based on thorough studies, eutectic bonding was selected for bonding the cap wafers to the device wafer. This requires optimizing several factors such as the thickness of the gold bond ring, bonding temperature, pressure, and time.

## References

- [1] C. Acar and A. M. Shkel. MEMS Vibratory Gyroscopes: Structural Approaches to Improve Robustness. 2<sup>nd</sup> edition, Springer 2009
- [2] N. Maluf and K. Williams. Introduction to Microelectromechanical Systems Engineering. 2<sup>nd</sup> edition, Artech House 2004
- [3] G.G. Coriolis. M'emoire sur les 'equations du mouvement relatif des syst'emes de corps. *Journal de l'ecole Polytechnique, Vol 15*, pp. 142-154. 1835
- [4] S. Beeby. MEMS Mechanical Sensors. 1<sup>st</sup> edition, Artech House 2004
- [5] W. Chow, J. Gea-Banacloche, L. Pedrotti, V. Sanders, W. Schleich and M. Scully. The ring laser gyro. *Reviews of Modern Physics 57(1)*, pp. 61. 1985
- [6] N. Yazdi, F. Ayazi and K. Najafi. Micromachined inertial sensors. *Proceedings of the IEEE 86(8)*, pp. 1640-1659. 1998
- [7] IEEE Std. 1431-2004. IEEE Standard Specification Format Guide and Test Procedure for Coriolis Vibratory Gyros.
- [8] IEEE Std. 528-2001. IEEE Standard for Inertial Sensor Terminology.
- [9] P. Greiff, B. Boxenhorn, T. King and L. Niles. Silicon monolithic micromechanical gyroscope. Presented at Solid-State Sensors and Actuators, 1991. Digest of Technical Papers, TRANSDUCERS'91, 1991 International Conference on, vol., no., pp.966-968, 24-27 Jun 1991
- [10] J. Bernstein, S. Cho, A. King, A. Kourepenis, P. Maciel and M. Weinberg. A micromachined comb-drive tuning fork rate gyroscope. Presented at Micro Electro Mechanical Systems, 1993, MEMS'93, Proceedings an Investigation of Micro Structures, Sensors, Actuators, Machines and Systems. IEEE, vol., no., pp.143-148, 7-10 Feb 1993
- [11] K. Tanaka, Y. Mochida, M. Sugimoto, K. Moriya, T. Hasegawa, K. Atsuchi and K. Ohwada. A micromachined vibrating gyroscope. *Sensors and Actuators A: Physical 50(1)*, pp. 111-115. 1995
- [12] W. A. Clark, R. T. Howe and R. Horowitz. Surface micromachined Z-axis vibratory rate gyroscope. Presented at Tech. Dig. Solid-State Sensor and Actuator Workshop. 1996
- [13] R. Voss, K. Bauer, W. Ficker, T. Gleissner, W. Kupke, M. Rose, S. Sassen, J. Schalk, H. Seidel and E. Stenzel. Silicon angular rate sensor for automotive applications with piezoelectric drive and piezoresistive read-out. Presented at Solid State Sensors and Actuators, 1997. TRANSDUCERS'97 Chicago, 1997 International Conference on , vol.2, no., pp.879-882 vol.2, 16-19 Jun 1997
- [14] M. Lutz, W. Golderer, J. Gerstenmeier, J. Marek, B. Maihofer, S. Mahler, H. Munzel and U. Bischof. A precision yaw rate sensor in silicon micromachining. Presented at Solid State Sensors and Actuators, 1997. TRANSDUCERS'97 Chicago, 1997 International Conference on, vol.2, no., pp.847-850 vol.2, 16-19 Jun 1997.
- [15] D. Sparks, S. Zarabadi, J. Johnson, Q. Jiang, M. Chia, O. Larsen, W. Higdon and P. Castillo-Borelley. A CMOS integrated surface micromachined angular rate sensor: Its automotive applications. Presented at Solid State Sensors and Actuators, 1997 TRANSDUCERS'97 Chicago, 1997 International Conference on , vol.2, no., pp.851-854 vol.2, 16-19 Jun 1997
- [16] F. Ayazi and K. Najafi. A HARPSS polysilicon vibrating ring gyroscope. *Microelectromechanical Systems, Journal of 10(2)*, pp. 169-179. 2001

- [17] G. He and K. Najafi. A single-crystal silicon vibrating ring gyroscope. Presented at Micro Electro Mechanical Systems, 2002. the Fifteenth IEEE International Conference on , vol., no., pp.718-721, 2002
- [18] T. K. Tang, R. C. Gutierrez, C. B. Stell, V. Vorperian, G. A. Arakaki, J. T. Rice, W. J. Li, I. Chakraborty, K. Shcheglov and J. Z. Wilcox. A packaged silicon MEMS vibratory gyroscope for microspacecraft. Presented at Micro Electro Mechanical Systems, 1997. MEMS'97, Proceedings, IEEE., Tenth Annual International Workshop on , vol., no., pp.500-505, 26-30 Jan 1997
- [19] T. Juneau, A. Pisano and J. H. Smith. Dual axis operation of a micromachined rate gyroscope. Presented at Solid State Sensors and Actuators, 1997. TRANSDUCERS'97 Chicago., 1997 International Conference on , vol.2, no., pp.883-886 vol.2, 16-19 Jun 1997
- [20] K. Y. Park, C. W. Lee, Y. S. Oh and Y. H. Cho. Laterally oscillated and force-balanced micro vibratory rate gyroscope supported by fish hook shape springs. Presented at Micro Electro Mechanical Systems, 1997. MEMS'97, Proceedings, IEEE., Tenth Annual International Workshop on , vol., no., pp.494-499, 26-30 Jan 1997
- [22] S. Lee, S. Park, J. Kim, S. Lee and D. I. Cho. Surface/bulk micromachined single-crystalline-silicon micro-gyroscope. *Microelectromechanical Systems, Journal of* 9(4), pp. 557-567. 2000.
- [23] H. Xie and G. K. Fedder. A CMOS-MEMS lateral-axis gyroscope. Presented at Micro Electro Mechanical Systems, 2001. MEMS 2001. the 14th IEEE International Conference on , vol., no., pp.162-165, 2001
- [24] H. Luo, X. Zhu, H. Lakdawala, L. R. Carley and G. K. Fedder. A copper CMOS-MEMS z-axis gyroscope. Presented at Micro Electro Mechanical Systems, 2002. the Fifteenth IEEE International Conference on , vol., no., pp.631-634, 2002
- [25] W. Geiger, W. Butt, A. Gaisser, J. Frech, M. Braxmaier, T. Link, A. Kohne, P. Nommensen, H. Sandmaier and W. Lang. Decoupled microgyros and the design principle DAVED. *Sensors and Actuators A: Physical* 95(2), pp. 239-249. 2002.
- [26] S. E. Alper, K. Azgin and T. Akin. A high-performance silicon-on-insulator MEMS gyroscope operating at atmospheric pressure. *Sensors and Actuators A: Physical* 135(1), pp. 34-42. 2007.
- [27] S. E. Alper and T. Akin. A single-crystal silicon symmetrical and decoupled MEMS gyroscope on an insulating substrate. *Microelectromechanical Systems, Journal of* 14(4), pp. 707-717. 2005.
- [28] S. E. Alper and T. Akin. Symmetrical and decoupled nickel microgyroscope on insulating substrate. *Sensors and Actuators A: Physical* 115(2), pp. 336-350. 2004.
- [29] C. Acar and A. M. Shkel. Inherently robust micromachined gyroscopes with 2-DOF sense-mode oscillator. *Microelectromechanical Systems, Journal of* 15(2), pp. 380-387. 2006.
- [30] S. E. Alper, Y. Temiz and T. Akin. A compact angular rate sensor system using a fully decoupled silicon-on-glass MEMS gyroscope. *Microelectromechanical Systems, Journal of* 17(6), pp. 1418-1429. 2008.
- [31] A. Sharma, F. M. Zaman, B. V. Amini and F. Ayazi. A high-Q in-plane SOI tuning fork gyroscope. Presented at Sensors, 2004. Proceedings of IEEE , vol., no., pp. 467-470 vol.1, 24-27 Oct. 2004
- [32] A. Sharma, M. F. Zaman and F. Ayazi. A sub-0.2°/hr bias drift micromechanical silicon gyroscope with automatic CMOS mode-matching. *Solid-State Circuits, IEEE Journal of* 44(5), pp. 1593-1608. 2009.

- [33] A. Sharma, M. Faisal Zaman and F. Ayazi. A 0.2 °/hr micro-gyroscope with automatic CMOS mode matching. Presented at Solid-State Circuits Conference, 2007. ISSCC 2007. Digest of Technical Papers. IEEE International , vol., no., pp.386-610, 11-15 Feb. 2007
- [34] M. Zaman, A. Sharma and F. Ayazi. High performance matched-mode tuning fork gyroscope. Presented at Micro Electro Mechanical Systems, 2006. MEMS 2006 Istanbul. 19th IEEE International Conference on , vol., no., pp.66-69, 2006
- [35] W. Sung, M. Dalal and F. Ayazi. A 3MHz spoke gyroscope with wide bandwidth and large dynamic range. Presented at Micro Electro Mechanical Systems (MEMS), 2010 IEEE 23rd International Conference on , vol., no., pp.104-107, 24-28 Jan. 2010
- [36] S. A. Zotov, A. A. Trusov and A. M. Shkel. High-range angular rate sensor based on mechanical frequency modulation. *Microelectromechanical Systems, Journal of* (99), pp. 1-8. 2012.
- [37] Y. Oh, B. Lee, S. Baek, H. Kim, J. Kim, S. Kang and C. Song. A surface-micromachined tunable vibratory gyroscope. Presented at Micro Electro Mechanical Systems, 1997. MEMS'97, Proceedings, IEEE., Tenth Annual International Workshop on , vol., no., pp.272-277, 26-30 Jan 1997
- [38] R. Hulsing. MEMS inertial rate and acceleration sensor. *Aerospace and Electronic Systems Magazine, IEEE* 13(11), pp. 17-23. 1998.
- [39] A. Kourepenis, J. Borenstein, J. Connelly, R. Elliott, P. Ward and M. Weinberg. Performance of MEMS inertial sensors. Presented at Position Location and Navigation Symposium, IEEE 1998 , vol., no., pp.1-8, 20-23 Apr 1998
- [40] Y. Mochida, M. Tamura and K. Ohwada. A micromachined vibrating rate gyroscope with independent beams for the drive and detection modes. Presented at Micro Electro Mechanical Systems, 1999. MEMS'99. Twelfth IEEE International Conference on , vol., no., pp.618-623, 17-21 Jan 1999
- [41] K. Funk, H. Emmerich, A. Schilp, M. Offenberg, R. Neul and F. Larmer. A surface micromachined silicon gyroscope using a thick polysilicon layer. Presented at Micro Electro Mechanical Systems, 1999. MEMS'99. Twelfth IEEE International Conference on , vol., no., pp.57-60, 17-21 Jan 1999
- [42] X. Jiang, J. I. Seeger, M. Kraft and B. E. Boser. A monolithic surface micromachined Z-axis gyroscope with digital output. Presented at VLSI Circuits, 2000. Digest of Technical Papers. 2000 Symposium on , vol., no., pp.16-19, 2000
- [43] A. K. S. A. Aziz, A. H. Sharaf, M. Y. Serry and S. S. Sedky. *MEMS mass-spring-damper systems using an out-of-plane suspension scheme, US patent application publication 2011/0030472A1 February 10, 2011* 2010.
- [44] C. T. C. Nguyen and R. T. Howe. An integrated CMOS micromechanical resonator high-Q oscillator. *Solid-State Circuits, IEEE Journal of* 34(4), pp. 440-455. 1999.
- [45] Z. Hao, A. Erbil and F. Ayazi. An analytical model for support loss in micromachined beam resonators with in-plane flexural vibrations. *Sensors and Actuators A: Physical* 109(1), pp. 156-164. 2003.
- [46] A. H. Nayfeh and D. T. Mook. *Nonlinear Oscillations*, 2<sup>nd</sup> edition, Wiley-VCH 2008.
- [47] B. J. Gallacher, J. Hedley, J. S. Burdess, A. J. Harris, A. Rickard and D. O. King. Electrostatic correction of structural imperfections present in a microring gyroscope. *Microelectromechanical Systems, Journal of* 14(2), pp. 221-234. 2005.
- [48] Z. Xiao, W. Peng, R. Wolffenbuttel and K. Farmer. Micromachined variable capacitors with wide tuning range. *Sensors and Actuators A: Physical* 104(3), pp. 299-305. 2003.
- [49] A. M. Elshurafa and E. I. El-Masry. Finite-element modeling of low-stress suspension structures and applications in RF MEMS parallel-plate variable

- capacitors. *Microwave Theory and Techniques, IEEE Transactions on* 54(5), pp. 2211-2219. 2006.
- [50] A. Elshurafa and E. El-Masry. The effects of non-uniform nanoscale deflections on capacitance in RF MEMS parallel-plate variable capacitors. *J Micromech Microengineering* 18, pp. 045012. 2008.
  - [51] A. M. Elshurafa, K. Khirallah, H. H. Tawfik, A. Emira, A. K. S. Abdel Aziz and S. M. Sedky. Nonlinear dynamics of spring softening and hardening in folded-MEMS comb drive resonators. *Microelectromechanical Systems, Journal of* (99), pp. 1-16. 2011.
  - [52] W. C. Tang, M. G. Lim and R. T. Howe. Electrostatic comb drive levitation and control method. *Microelectromechanical Systems, Journal of* 1(4), pp. 170-178. 1992.
  - [53] Y. J. Su, C. F. Qian, M. H. Zhao and T. Y. Zhang. Microbridge testing of silicon oxide/silicon nitride bilayer films deposited on silicon wafers. *Acta Materialia* 48(20), pp. 4901-4915. 2000.
  - [54] G. S. Hwang and K. P. Giapis. On the origin of the notching effect during etching in uniform high density plasmas. *Journal of Vacuum Science & Technology B: Microelectronics and Nanometer Structures* 15(1), pp. 70-87. 1997.
  - [55] P. K. Montgomery, R. D. Peters, C. Garza, T. Breeden, M. Azrak, J. Jiang and K. Kim. Improved ion implantation masking through photoresist fluorination. Presented at Proceedings of SPIE. 2006.
  - [56] H. Jansen, H. Gardeniers, M. Boer, M. Elwenspoek and J. Fluitman. A survey on the reactive ion etching of silicon in microtechnology. *J Micromech Microengineering* 6, pp. 14. 1996.
  - [57] J. Bhardwaj, H. Ashraf and A. McQuarrie. Dry silicon etching for MEMS. Presented at Proc. Symp. Microstructures and Microfabricated Systems, ECS. 1997.
  - [58] N. P. Pham, J. N. Burghartz and P. M. Sarro. Spray coating of photoresist for pattern transfer on high topography surfaces. *J Micromech Microengineering* 15, pp. 691. 2005.
  - [59] A. Rockett. *The Materials Science of Semiconductors*, 1<sup>st</sup> edition, Springer 2007.
  - [60] J. H. Lau, C. K. Lee, C. S. Premachandran and Y. Aibin, *Advanced MEMS Packaging*. McGraw-Hill 2010.
  - [61] P. Monajemi, F. Ayazi, P. Joseph and P. Kohl. A low cost wafer-level MEMS packaging technology. Presented at Micro Electro Mechanical Systems, 2005. MEMS 2005. 18th IEEE International Conference on , vol., no., pp. 634- 637, 30 Jan.-3 Feb. 2005
  - [62] K. Najafi. Micropackaging technologies for integrated microsystems: Applications to MEMS and MOEMS. Presented at Proc. SPIE, Vol. 4979, pp. 1-19, Jan 15, 2003.
  - [63] M. Esashi. Wafer level packaging of MEMS. *J Micromech Microengineering* 18, Article Number 073001. 2008.
  - [64] L. Lin, R. T. Howe and A. P. Pisano. Microelectromechanical filters for signal processing. *Microelectromechanical Systems, Journal of* 7(3), pp. 286-294. 1998.
  - [65] R. Kant, N. Ferralis, J. Provine, R. Maboudian and R. T. Howe. Experimental investigation of silicon surface migration in low pressure nonreducing gas environments. *Electrochemical and Solid-State Letters* 12, pp. H437. 2009.
  - [66] S. Sedky, H. Tawfik, A. Abdel Aziz, S. El Saegh, A. Graham, J. Provine and R. Howe. Low thermal-budget silicon sealed-cavity microencapsulation process. Presented at Micro Electro Mechanical Systems (MEMS), 2011 IEEE 24<sup>th</sup> International Conference on , vol., no., pp. 276-279, 23-27 Jan. 2011
  - [67] B. Lee, S. Seok and K. Chun. A study on wafer level vacuum packaging for MEMS devices. *J Micromech Microengineering* 13, pp. 663. 2003.

- [68] P. J. Joseph, P. Monajemi, F. Ayazi and P. A. Kohl. Wafer-level packaging of micromechanical resonators. *Advanced Packaging, IEEE Transactions on* 30(1), pp. 19-26. 2007.
- [69] K. H. Lu, X. Zhang, S. K. Ryu, J. Im, R. Huang and P. S. Ho. Thermo-mechanical reliability of 3-D ICs containing through silicon vias. Presented at Electronic Components and Technology Conference, 2009. ECTC 2009. 59<sup>th</sup>, 2009. ECTC 2009. 59<sup>th</sup>, vol., no., pp.630-634, 26-29 May 2009
- [70] D. S. Tezcan, F. Duval, H. Philipsen, O. Luhn, P. Soussan and B. Swinnen. Scalable through silicon via with polymer deep trench isolation for 3D wafer level packaging. Presented at Electronic Components and Technology Conference, 2009. ECTC 2009. 59<sup>th</sup>, vol., no., pp.1159-1164, 26-29 May 2009
- [71] A. Fischer, N. Roxhed, T. Haraldsson, N. Heinig, G. Stemme and F. Niklaus. Fabrication of high aspect ratio through silicon vias (TSVs) by magnetic assembly of nickel wires. Presented at Micro Electro Mechanical Systems (MEMS), 2011 IEEE 24<sup>th</sup> International Conference on , vol., no., pp.37-40, 23-27 Jan. 2011
- [72] P. Nilsson, A. Ljunggren, R. Thorslund, M. Hagstrom and V. Lindskog. Novel through-silicon via technique for 2d/3d SiP and interposer in low-resistance applications. Presented at Electronic Components and Technology Conference, 2009. ECTC 2009. 59<sup>th</sup>, vol., no., pp.1796-1801, 26-29 May 2009
- [73] M. J. Wolf, T. Dretschkow, B. Wunderle, N. Jurgensen, G. Engelmann, O. Ehrmann, A. Uhlig, B. Michel and H. Reichl. High aspect ratio TSV copper filling with different seed layers. Presented at Electronic Components and Technology Conference, 2008. ECTC 2008. 58<sup>th</sup>, vol., no., pp.563-570, 27-30 May 2008.
- [74] S. D. Senturia. *Microsystem Design* 2001.
- [75] M. J. Madou. *Fundamentals of Microfabrication: The Science of Miniaturization*. 2<sup>nd</sup> edition, CRC Press 2002.
- [76] M. Lefebvre, G. Allardyce, M. Seita, H. Tsuchida, M. Kusaka and S. Hayashi. Copper electroplating technology for microvia filling. *Circuit World* 29(2), pp. 9-14. 2003.
- [77] F. Niklaus, P. Enoksson, E. Kälvesten and G. Stemme. Low-temperature full wafer adhesive bonding. *J Micromech Microengineering* 11, pp. 100. 2001.
- [78] M. Shimbo, K. Furukawa, K. Fukuda and K. Tanzawa. Silicon-to-silicon direct bonding method. *J. Appl. Phys.* 60(8), pp. 2987-2989. 1986.
- [79] Y. Kanda, K. Matsuda, C. Murayama and J. Sugaya. The mechanism of field-assisted silicon-glass bonding. *Sensors and Actuators A: Physical* 23(1), pp. 939-943. 1990.
- [80] A. Berthold, L. Nicola, P. Sarro and M. Vellekoop. Glass-to-glass anodic bonding with standard IC technology thin films as intermediate layers. *Sensors and Actuators A: Physical* 82(1-3), pp. 224-228. 2000.
- [81] Corning Pyrex 7740 wafers, data sheet.
- [82] C. Iliescu, B. Chen and J. Miao. On the wet etching of pyrex glass. *Sensors and Actuators A: Physical* 143(1), pp. 154-161. 2008.
- [83] X. Li, T. Abe and M. Esashi. Deep reactive ion etching of pyrex glass using SF<sub>6</sub> plasma. *Sensors and Actuators A: Physical* 87(3), pp. 139-145. 2001.
- [84] E. Belloy, S. Thurre, E. Walekiers, A. Sayah and M. Gijs. The introduction of powder blasting for sensor and microsystem applications. *Sensors and Actuators A: Physical* 84(3), pp. 330-337. 2000.
- [85] R. Knechtel. Glass frit bonding: An universal technology for wafer level encapsulation and packaging. *Microsystem Technologies* 12(1), pp. 63-68. 2005.
- [86] FX-11-036 by Ferro Datasheet.

- [87] R. Knechtel, M. Wiemer and J. Frömel. Wafer level encapsulation of microsystems using glass frit bonding. *Microsystem Technologies* 12(5), pp. 468-472. 2006.
- [88] R. Wolffenbuttel. Low-temperature intermediate au-si wafer bonding; eutectic or silicide bond. *Sensors and Actuators A: Physical* 62(1-3), pp. 680-686. 1997.
- [89] F. Niklaus, G. Stemme, J. Q. Lu and R. Gutmann. Adhesive wafer bonding. *J. Appl. Phys.* 99, Article Number 031101. 2006.